UNIVERSITÀ POLITECNICA DELLE MARCHE

FACOLTÀ DI INGEGNERIA

Dipartimento di Ingegneria dell'Informazione

Master's degree in BIOMEDICAL ENGINEERING

Quantifying SAR Induced by Smartphone Operation on Biological Models: A Comparison Between Two Simulation Programs.

Supervisor:

Prof. Franco Moglie

Author:

Caterina Antonacci

Co-supervisor:

Prof. Valter Mariani Primiani

Academic year: 2022-2023

To my Father and Mother,
the ones who have been my saviors.

Abstract

The constant and enormous growth in the use of smartphones in wireless communication has exacerbated and generated understandable concern for human health and related health risks. The main parameter capable of defining the quantity of energy emitted by the source, and how much of it affects people, is the specific absorption rate. It is also useful for evaluating aspects relating to the safety of the devices themselves. In this context, two numerical methods, namely finite-difference time-domain using the *C* language, and the second, identified as a finite integration technique method through CST Studio Suite are used to compute the specific absorption rate. Both methods proposed follow a similar procedure, the initial step involves the development of a planar inverted-F antenna, the choice falls on a 1.8 GHz. Subsequently, consists in testing, trough simulations aimed to test the antenna's performance on different human body models woman and child. For both models, three body parts have been chosen to interact with the antenna: ear, mouth and chest, and at three distances: 1 mm, 16 mm, 50 mm. The goal is to evaluate the energy absorbed by the human body. Furthermore, the study analyzes the Specific absorption rate averaged at 1 g and 10 g which allowed us to evaluate the absorption rate that goes from the most superficial to the deepest layers of the human body, in order to obtain a more complete overview of exposure to the electromagnetic waves. For both methods, the result, demonstrates precision, accuracy, and similarity, reinforcing the reliability of the finding.

INDEX:

1. Introduction

During the past years, there has been an exponential growth in the usage of wireless devices, starting from smartphones, earbuds, to wearable devices. As for smartphones, they have become an integral part of our lives, serving purposes from personal to professional. However, due to the increased utilization of these wireless devices, there has been a consequent inquiry into the potential effects these devices might have on the human body. This has prompted scientific research to delve deeper into the effects of human exposure to electromagnetic fields generated by such devices.

An essential parameter that measures the absorption of electromagnetic energy by biological tissues is the specific absorption rate (SAR), and this parameter can be obtained through various methods. In the specific context of this thesis, we will examine the finite difference time domain (FDTD) and finite integration technique (FIT) methods.

These two techniques have been developed over the past decades and have immediately proven to be effective and powerful methods for evaluating the interaction between human biological models and electromagnetic fields in various exposure scenarios. We have analyzed key situations in which smartphones are used, such as during a call (thus involving interaction between the smartphone and the human ear), when sending a voice message or call using the speakerphone (involving interaction between smartphone and mouth), and at last, when the smartphone is placed in a jacket pocket (resulting in chest exposure).

Before delving into these scenarios, the study has highlighted the main electromagnetic characteristics of a source like an antenna (in our case, a planar inverted-F antenna or PIFA characterized by an L-shaped structure), the fundamentals of the employed methods (FDTD, FIT), the essence of the parameter of our interest (SAR) and the regulations set forth by entities like FCC (Federal Communications Commission) and ICNIRP (International Commission on Non-Ionizing Radiation Protection). These organizations established exposure limits for electromagnetic fields to the population (both workers and non-workers)

in the late 1990s, considering exposure duration and operational frequency of the source in question.

However, it is crucial to emphasize that despite the increased scientific studies on SAR and its potential adverse effects on human bodies in recent years, which have undoubtedly contributed to understanding mechanisms of this nature, the analysis of SAR and its effects remains highly variable and constantly evolving.

1.1. Antenna's Features

Since the 1980s, when antennas in use worldwide were relatively few, antenna implementations have increased significantly. Today, thanks to smartphones and wireless communications, antennas play an essential role in everyday life.

The definition of an antenna in the context of communications is "a part of an electric device designed to receive or radiate electromagnetic waves"; in other words, an antenna is a component of a device that allows electrical energy to be generated, travel through air or space, and then arrive at a receiver with an associated magnetic field.

The frequency can be thought of as the number of times that an electromagnetic wave occurs. Since electromagnetic (EM) waves have a periodic shape with a period (T) and wavelength (λ); they change in space and time like a sinusoidal wave. (1)

Therefore, the frequency is the number of full cycles that occur in a second. (2) Mathematically:

$$f = \frac{1}{T}$$

Equation 1

Because wavelength and frequency are inversely related (faster frequency, shorter wavelength), the velocity of waves depends on frequency of occurrence. So:

$$c = f\lambda$$

Equation 2

Also important is the degree of directivity measured by "antenna gain" which also defines the efficiency of the antenna.

These are the main factors we take into account, however it's also important to consider additional ones, such as:

- "Far-field pattern" (radiation pattern) is the spatial EM distribution that depends on the angular directions of the strength of waves from the antenna. The antenna gait is the ratio of the intensity (in a given direction) to the radiation intensity that results from isotropically radiating the power that the antenna accepts. (1) (3)
- "Antenna impedance" refers to the system's terminal point as measured by the voltage ratio across a point. (1) (3)
- The term "bandwidth" refers to the frequency range where the antenna is capable of operating. (1) (3)

The term "radiation efficiency" refers to the ratio between the power transmitted across all directions and the power received by the antenna receiver. Radiation efficiency has a range between 0 and 1, and the higher the value, the better the antennas are at radiating the majority of the absorbed power. (4) However, some of the power available by the terminal is not received due to the antennas' limited conductivity.

The term "polarisation" refers to the plane orientation in which an electric field travels; as a result, in the context of an antenna, it depends on the polarisation of transmitted waves. In its most basic form, polarisation is a linear phenomenon that can be either vertical or horizontal.

The final metric, "return loss" (RL), measures the difference between incident and reflected power in decibels (dB) between the antenna attached to the line and the impedance of the line itself.

$$RL(dB) = 10\ log_{10} \frac{P_i}{P_r}$$

Equation 3

This match is good if the RL (dB) is high, but the return loss is related to the ratio between amplitude of reflected voltage wave (V_0^-) and incident voltage wave (V_0^+), also called "reflection coefficient" (Γ). Hence:

$$\Gamma = \frac{V^-}{V^+} = \frac{Z_A - Z_0}{Z_A + Z_0}$$

Equation 4

The perfect match occurs at: $Z_A = Z_0$, means Γ is null; but is necessary to consider the Voltage Standing Wave Ratio (VSWR), represents the power reflected from the antenna, and is in function of Γ; so:

$$VSWR = \frac{|V^+| + |V^-|}{|V^+| - |V^-|} = \frac{1 + |\Gamma|}{1 - |\Gamma|}$$

Equation 5

This means that in case of perfect matching is VSWR = 1. An acceptable matching occurs when the power loss is lower than 10%, means that:

$$\begin{cases} \text{RL} < -10\ \text{dB} \\ |\Gamma| < 1/3 \\ 1 \leq \text{VSWR} < 2 \end{cases}$$

Equation 6

By considering that:

$$RL = |S_{11}|_{dB} = 10log_{10}|\Gamma|^2$$

Equation 7

In this context, this parameter allows measuring the reflection of an antenna that produces an electromagnetic wave incident on other electronic systems or objects. It is used to evaluate the efficiency, impedance, and other characteristics of the antenna. (5)

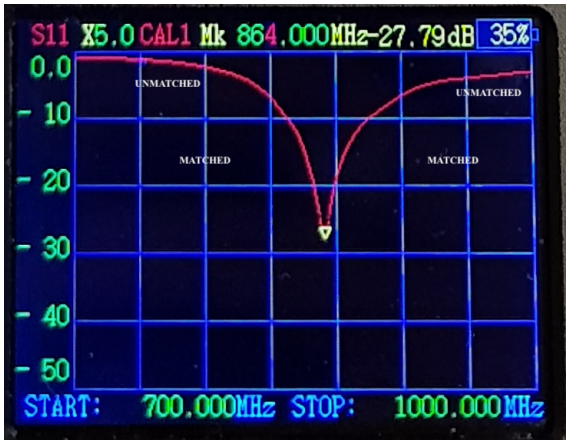

Figure 1: Example of measured Return Loss.

1.1.2. Field Regions

The space around the antenna is divided into three regions:

1. “Reactive near-field-region”, the area nearest the antenna where the electrical and magnetic fields are displayed 90 degrees from each other.

2. “Radiating near-field region” in which electric and magnetic fields are perpendicular to each other with no displacement, is the middle between the two regions. It is the field the EM field can be transformed from reactive to radiative one.

3. “Far-field region” that is the area far from the antenna characterized by radiated EM fields, and follow the equations, considering that “D” is the largest dimensions of antenna:

$$Far\_field > \frac{2D^2}{\lambda}$$

Equation 8

The “far-field region” is commonly taken to exist at a distance that is higher than Equation 8 but can occurs that same antennas (specially multibeam reflector antennas) are sensible to the variation of phase, and this may be inadequate.

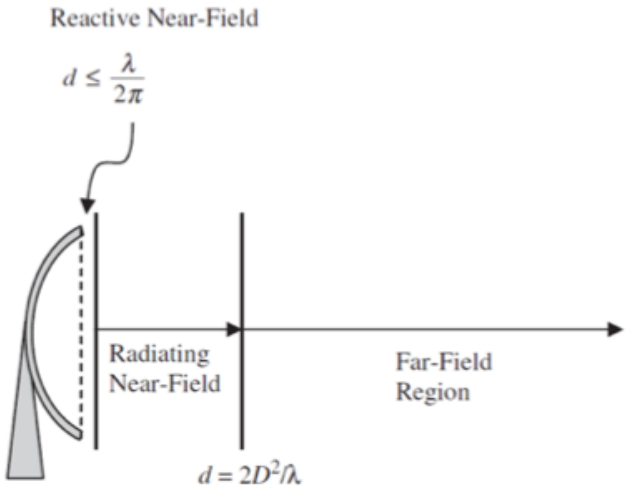

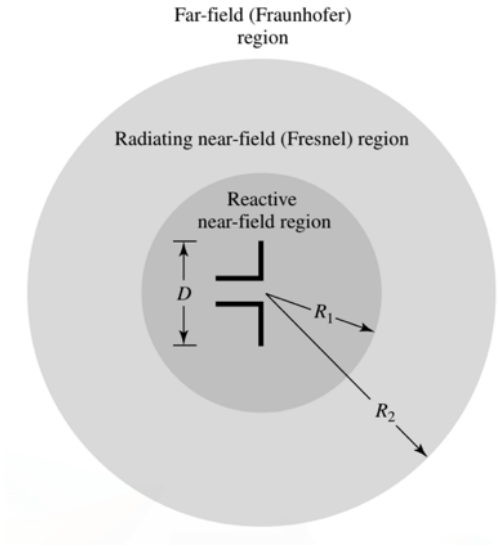

Figure 2: Representative images of the antenna's field region.

As the figure displayed there is "R_1" and "R_2" that represents the inner and outer boundary respectively, that are equal to:

$$R_1 = 0.62\frac{\sqrt{D}^3}{\lambda}$$

Equation 9

$$R_2 = \frac{2D^2}{\lambda}$$

Equation 10

The shape of an antenna's amplitude pattern is also dependent on variations in the field's phase and magnitude. For example, in the reactive near-field region, the pattern is more uniform and dispersed; as the wave advances to the next region the Fresnel region (Radiating near-field region), the pattern becomes smoother and produces lobes; and in the final region, the Fraunhofer region (far-field region), the pattern is well-formed and produces one or more major lobes and a few minor ones.

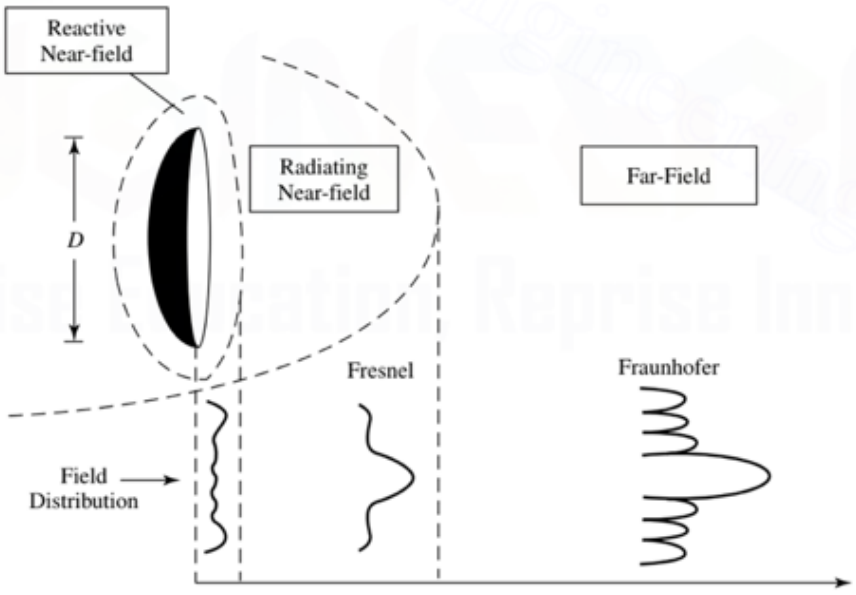

Figure 3: image about change of antenna amplitude pattern shape.

1.1.3. Microstrip Antennas

In the 1970s, Microstrip antennas gained enormous popularity, particularly in government and commercial uses for wireless and mobile radio communication, such as on the surfaces of high-performance aircraft, satellites, vehicles, and handheld mobile phones (1) (6) (7) (8) They consist of a metallic patch on a substrate of the ground. These antennas can be set up in a variety of ways:

a) Square
b) Rectangular
c) Dipole
d) Circular
e) Elliptical
f) Triangular
g) Disc sector
h) Circular ring
i) Ring sector

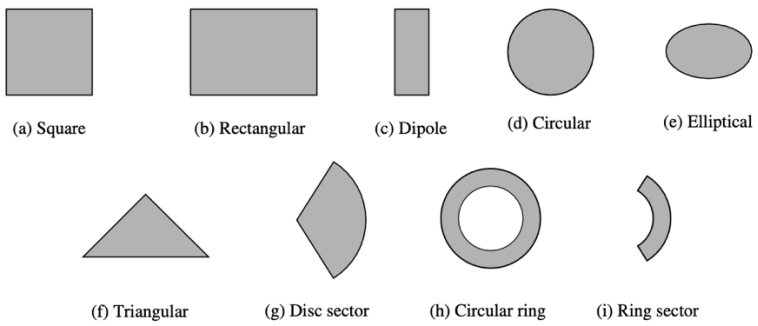

Figure 4: Different microstrip patch shape.

Due to their simplicity in analysis and fabrication, circular (d) and rectangular (b) patch antennas are the most popular, and their main advantage is their decreased radiation at cross-polarizations. They are very adaptable, particularly because of resonant frequency resonance, polarisation, pattern, and impedance, but their main drawbacks are low efficiency and power, poor polarisation purity and performance (if the wave's surface is excluded), and a limited bandwidth (around 35%). It is possible to increase efficiency and bandwidth by increasing the height of the substrate, though this has its drawbacks as well. (6)

The thin metallic strip (like a patch) above the ground plane is one of the fundamental features of microstrip antennas. They are created in such a way that the maximal pattern achieved by selecting the proper excitation mode over the patch is normal to the patch.

Think about rectangular patch or microstrip antennas that are supplied by a transmission line.

The patch is on a substrate with related heights "H" and permittivity "ε_r" and has dimensions of length "L" and width "W" (which regulate the input impedance). The thickness is typically "h" smaller than wavelength ($\approx \frac{1}{40}\lambda$). (9)

The operation frequency is defined as:

$$f_c \approx \frac{c}{2L\sqrt{\varepsilon_r}} = \frac{1}{2L\sqrt{\varepsilon_0 \varepsilon_r \mu_0}}$$

Equation 11

This means that the path's length should be one half of wavelength within the substrate medium.

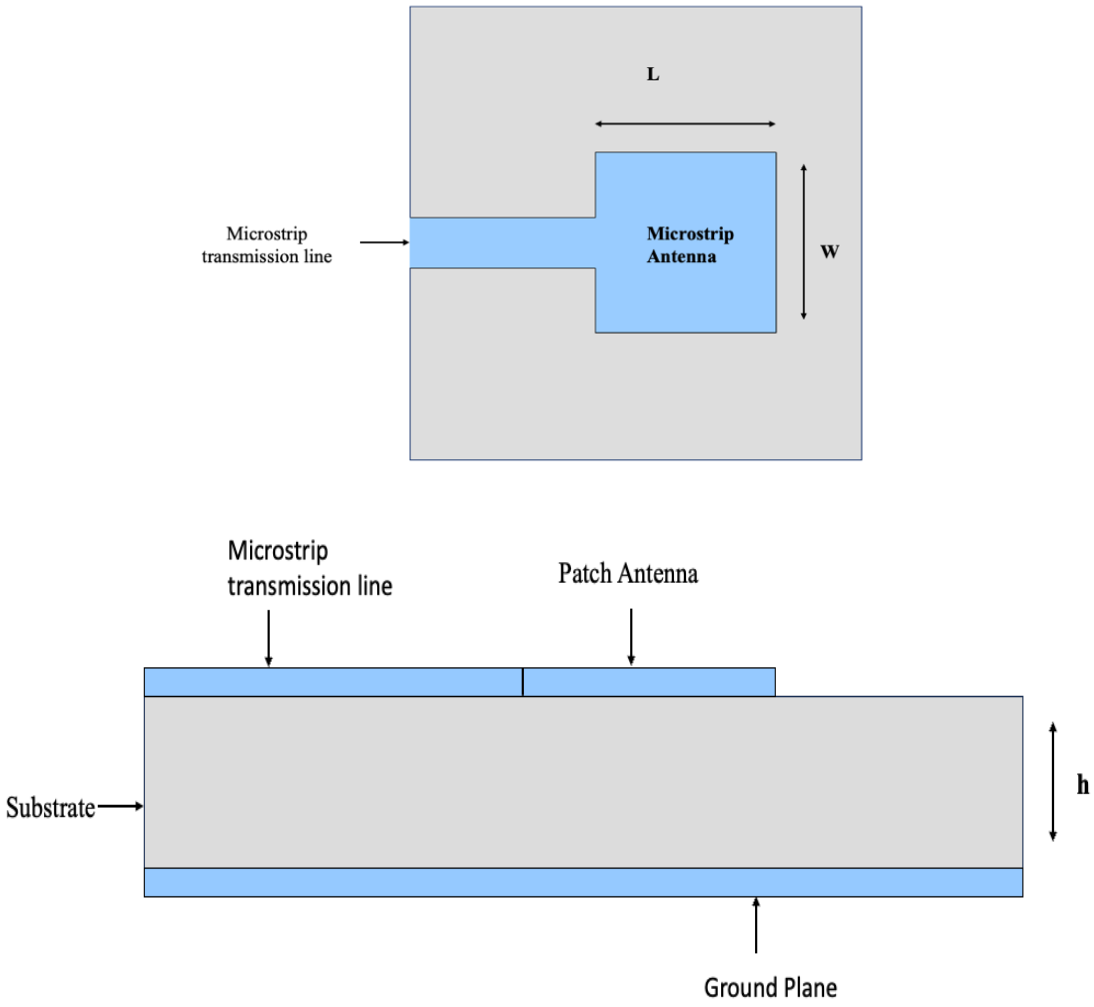

Figure 5: Graphics representation of main characteristics of antenna.

1.1.3.1 Inverted-F Antennas

An inverted-F antenna (IFA) is normally made up of a ground plane, or short-circuiting plate, that is positioned below a rectangular planar element and is connected to a planar element feeding mechanism. IFA is a specific type of antenna that reduces height while preserving resonant length by having the upper section parallel to the ground plane. This new layout causes capacitance to become the antenna's impedance, and the rising capacitance is balanced by a short circuit known as a stub, whose end is connected to the antenna's ground plane.

When an antenna's one dimension is restricted, IFA is advised, especially for heart rate monitors.

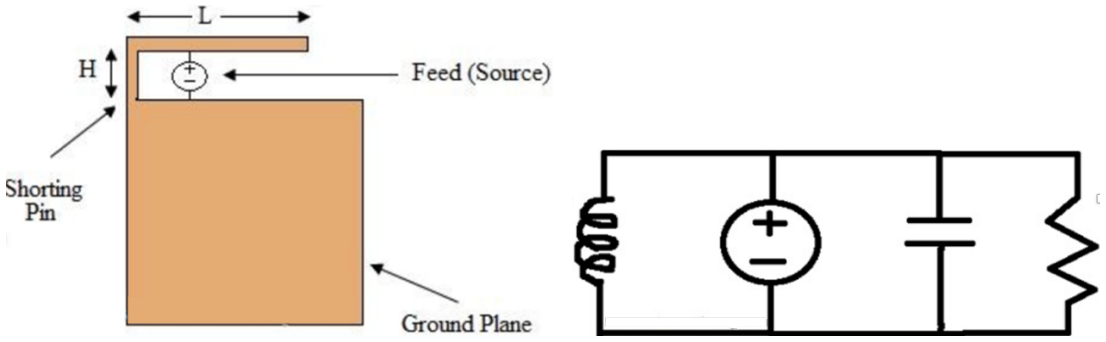

Figure 6: Typical geometry of IFA and associated equivalent circuit model.

1.1.3.2. Planar Inverted-F Antenna (PIFA)

The Planar Inverted-F antenna (PIFA), utilized in wireless mobile communications systems, is a unique variety of microstrip antenna (10) (11). In this instance, the electrical length, which is associated with the operation frequency, affects the radiation efficiency and gain characteristics; also, the monopole position influences the pattern, but the least one is not too many which affect the input impedance and the resonant frequency.

In this case is introduced, between the patch and ground plane, a short pin and it is used "Quarter-Wavelength Patch", due to shorted length the current of antenna patch in not forced to be null, also the antenna gain is reduced due to the presence of fringing field, responsible for the radiation, in specific positions is irradiated only the field near to the transmission line. Practically the PIFA is resonant on quarter- wavelength, due to the shorter pin at the end, in a way to reduce the dimensions of the antenna itself; this antenna is characterized to an omnidirectional pattern. PIFA have a feed point between the open and shorted end in a way to control the input impedance.

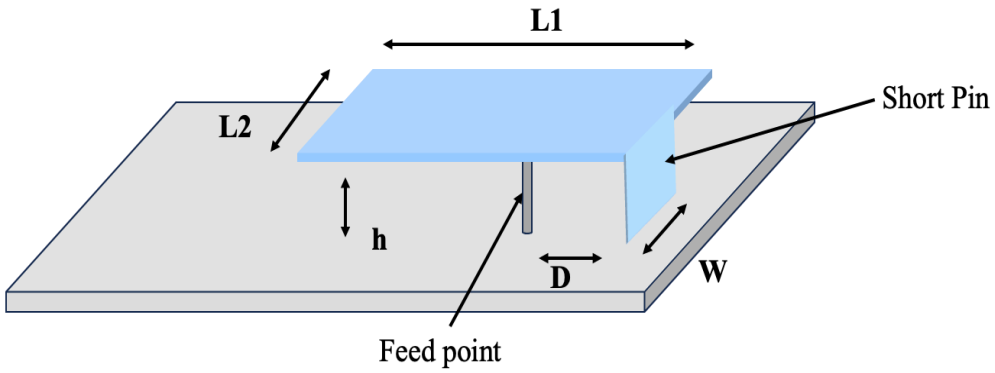

Figure 7: Representation of general PIFA antenna.

In which “L1” defines the length of PIFA, “L2“ its width; “W“ stays for the width of short Pin, “D“ defines the distance between feed point and shorting pin, at the end “h“ defines the height of PIFA from the ground plane.

The distance is one of the main parameters, because through it is possible to control the impedance of the antenna, due to the inversely proportionality between them, practically if we move closer the feed and the shorting pin the impedance will decrease.

Instead, the resonant frequency depend on W because of:

$$if\ W = L2 \rightarrow L1 = \frac{\lambda}{4}$$

Equation 12

This mean that if the shorting pin width is equal to antenna width our PIFA has maximum radiation efficiency at quarter-wavelength; instead, if we consider that the shorting pin width is equal to zero, or at least lower than “L2“, the antenna is resonant at:

$$If\ W = 0 \rightarrow L1 + L2 = \frac{\lambda}{4}$$

Equation 13

Generalizing the problem, it’s possible to define that the resonant length is in function of “L1“(antenna’s length), “L2“(antenna’s width), “W “(short pin width).

$$L1 + L2 + W = \frac{\lambda}{4}$$

Equation 14

Also, it is necessary to consider the substrate dielectric constant (ε_r) between patch and ground plane by calculating the square root of “ε_r“. The previous equation become:

$$(L1 + L2 + W)\sqrt{\varepsilon_r} \approx \frac{\lambda}{4}$$

Equation 15

The least equation represents resonances’ conditions considering the dielectric constant substrate, i.e., FR-4. This FR-4 is a particular matter defined as “ composite material

composed of woven fiberglass cloth with an epoxy resin binder that is flame resistant (self-extinguishing).” (12) The main characteristics are related to the variation of conductivity in function of frequency; also have a dielectric loss, or loss tangent (defined as the ratio between conductivity and frequency) very high; this means that we have a very high attenuation of signal at high frequencies. (13)

Another important parameters are the height and the dimensions of patch (biggest is the patch lower is the frequency) because from this it is possible to define the bandwidth of resonant frequencies.

$$f_{lower}(GHz) \approx \frac{c}{4\big(L(mm) + W(mm) + h(mm)\big)\sqrt{\varepsilon_{eff}}}$$

$$f_{upper}(GHz) \approx \frac{c}{4\big(L_2(mm) + L_3(mm)\big)\sqrt{\varepsilon_{eff}}}$$

Equation 16

In which “ε_{eff}“ is representant as:

$$\varepsilon_{eff} = \frac{\varepsilon_r\ \varepsilon_{air}(h_s + h_{air})}{\varepsilon_r\ h_{air} + \ \varepsilon_{air}\ h_s}$$

Equation 17

Where, “ε_r“ represents the dielectric constant of FR-4 substrate; “ h_s“is the associated height of separation of FR-4 substrate; “ε_{air}“ is the dielectric constant of air, “h_{air}“, at the end, is the height of the separation of air. (14)

1.2. Finite Integration Technique

Finite Integration Technique is one of the two most used numerical method to solve Maxwell's equation.

It calculates the field step by step considering time, if the integrations width of the step doesn't overcome the limit the method remains stable, also, this value is related to the discretization of the structure because denser is the grid, smaller is the usable time step width and so, this can determine the global timestep and the total simulation time. (15)

To obtain robust performance, same software (like CST studio) combines the use of FIT with Perfect Boundary Approximations (PBA) and Thin Sheet Technique (TST)

The first one is used for spatial discretization obtaining a good approximation of curved surface within a cubic mash cell in a way to map the EM field and structure in a hexahedral mesh.

FIT's aim is to provide a universal spatial discretization applicable for most EM problem fields, from the static to high frequency application either in time or frequency domain.

It starts from the integral form Maxwell's equation, but to solve the equation it is necessary to define a finite domain included into the considered applications. The spatial discretization is performed by splitting the starting structure in many cells generating the grid, in which the primary grid has an electric grid voltage "e" and magnetic fluxes "b", and the dual grid has a dielectric fluxes "d" and magnetic grid voltage "h".

$$\oint_{\delta A} \vec{E}\ d\vec{s} = -\int_{A} \frac{\delta \vec{B}}{\delta t} \delta \vec{A}$$

$$\oint_{\delta V} \vec{D}\ d\vec{A} = \int_{V} \rho dV$$

$$\oint_{\delta A} \vec{H}\ d\vec{s} = \int_{A} \left(\frac{\delta \vec{D}}{\delta t} + \vec{J}\right) \delta \vec{A}$$

$$\oint_{\delta V} \vec{B}\ d\vec{A} = 0$$

Equation 18

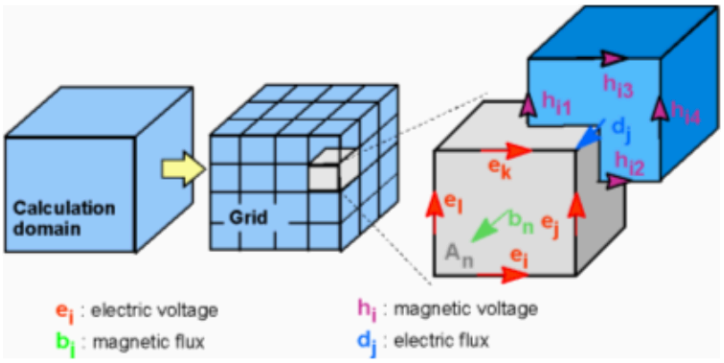

Figure 8: Graphic representation of first part of FIT procedure.

Now, Maxwell's equations are made for each cell separately, but considering Faraday's equations (left side of image) can be re-written as the sum of four grid's voltage and, repeating this procedure many times, obtain the topological matrix C.

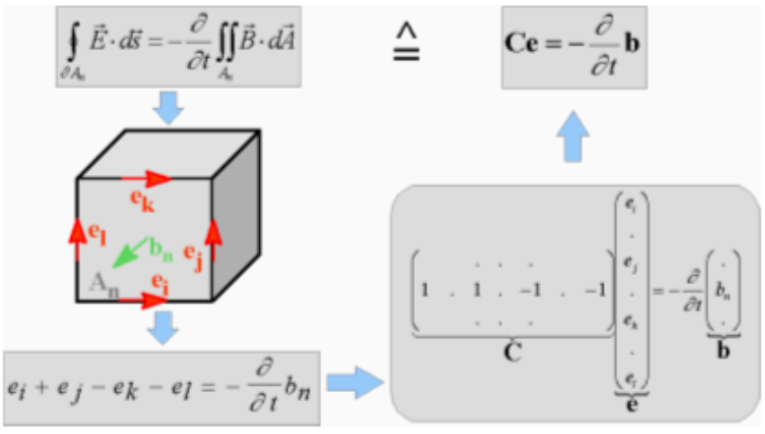

Figure 9: Graphic representation of second part of FIT procedure.

If it is applied the same scheme for the Ampere law, will have the definition of the correspondent dual discrete curl operator "$\widetilde{C}$"; in the case of divergence equations lead to two discrete operators, “S” and “$\tilde{S}$” belongs to the first grid and the second grid. At the end it is obtained the complete set of Maxwell’s Grid equations (MGEs) without considering the discretization error, but are maintained in grid space the continuous gradient, curl and divergence properties.

$$Ce = -\frac{d}{dt}b \qquad \tilde{C}h = \frac{d}{dt}d + j$$

$$\tilde{S}d = q \qquad Sb = 0$$

$$SC = \tilde{S}\tilde{C} = 0 \quad \Leftrightarrow \quad div\, rot \equiv 0$$

$$C\tilde{S}^T = \widetilde{C}\, S^T = 0 \quad \Leftrightarrow \quad rot\, grad \equiv 0$$

Equation 19

The formulation of FIT is not influenced by problems related to instability for a long time because the CGEs equation are able to maintain the energy and charge conservation.
When is defining the relation between fluxes and voltage, their integral form must be approximate considering boundary of cell and areas of cell, this led to a numeric imprecision; so, the resultant coefficient depends on the averaged parameters of the material and also from the spatial resolution of grid.
At the end, it’s possible to define that FIT method with the application of the same techniques can maintain all the advantages of a artesian grid also for curve structure; and can improve a better modeling of electric conducting sheets.

To summarize the FIT method, it's possible apply this kind of technique from continuous current to high frequency, and it can be rewritten in case of cartesian grid and time domain in a way to obtain one of the standard methods in Finite Difference Time Domain (FDTD). The main technique to solve FIT method is the transient solver, in which the last one is based on discretization of Maxwell's Grid Equations substituting the time derivative by considering the central difference, in case of loss-free case, it's possible obtain:

$$e^{n+1} = e^{n-\frac{1}{2}} + \Delta t M_{\tilde{Z}}^{-1}\left[\tilde{C} M_{\mu}^{-1} b^{n} + j_{S}^{n}\right]$$

$$b^{n+1} = b^{n} - \Delta t C e^{n+\frac{1}{2}}$$

Equation 20

Considering the electric voltage and magnetic fluxes it's possible calculates the variable above, the unknown parameters instead are in time in a "leap-frog scheme":

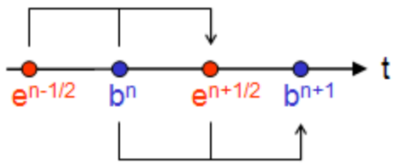

Figure 10: Graphic representation of "leap-frog scheme".

The stability is defined considering Courant-Friedrichs-Levy (CFL) criterion, requiring that the propagation in one time step should not exceed the grid cell sizes. Practically:

$$\Delta t \leq \frac{\sqrt{\varepsilon\mu}}{\sqrt{\left(\frac{1}{\Delta x}\right)^{2} + \left(\frac{1}{\Delta y}\right)^{2} + \left(\frac{1}{\Delta z}\right)^{2}}}$$

Equation 21

1.3. Finite-Difference Time Domain Method

In 1966 Yee introduced Finite-Difference Time Domain (FDTD) technique while the name and acronym “FDTD” was coined by Allen Taflove in 1980 (16) (17)

The principal features of this method are related to the non-uses of linear algebra, in order to avoid limitation in term of size of frequency domain integral equations and finite element in electromagnetic models; additionally, treats non-linear behavior and impulsive one in a natural way, in case of impulsive response because of it calculates in direct way the impulse response of EM system, in fact FDTD simulation can provide ultrawideband temporal waveform or sinusoidal response in steady-state conduction at any frequency.

FDTD method is a systematic approach because when is defined a new structure the problem is reduced only in mesh generation; the source of error of this metho is comprehended, means that can be bounded to allow the simulations of accurate model for large variety of EM interaction problems. The main problem related to this method are the requirement of large access memory in computer visualization field, but both the problem can be solved through the rapidly increasing memory of computers and the increasing of computer visualizations.
FDTD technique allow direct solution of Maxwell’s curl equations, the basic principle is the volumetric samples of unknown electric vector “E” and associated magnetic vector “H” within and on the boundary structure of interest for a certain time, the volumetric sampling is at sub-wavelength resolution, typically 10-20 samples per λ_0 sampling, in time is used to ensure numerical stability to the algorithm.
In general, this kind of algorithm simulates continuous electromagnetic waves in a finite space through sampled numerical data that propagates in a computer space.

Practically, this algorithm is an explicit solver that uses parallel and highly vectorizable schemes in order to advance in time the filed the six components of “E” and “H” in each spatial cell. The methods can be divide considering the degree of structure or the regularity in the mash cells:

a) Almost completely structured; in which the unit cell is congruent where possible. Also, it is possible to modify the size and shape of adjacent cells to structural features to fit completely its surface (18) (19). In this case, from the computational point of view, the modified cells are proportional to the surface area of structure, then the number of cells modified decreases progressively than the regular cells fitted volume of structure as the size increases.

b) Surface-fitted; in this case the space grid is completely distorted in a way to fit the shape of structure, but the grid can be divided in many zones to include different surface features (20) The main problems related to this are the memory allocations for the position of each cell and the extra operation to complete the Maxwell’s equations at each cell and to guarantee a continuity field at interfaces of two adjacent cells.

c) Completely unstructured; the space is fully filled by cells with different shapes and sizes (21), in fact the main problem is related to the numerical accuracy and instability because the generation of random cells introduces high distortion.

1.3.1 Yee Algorithm

The article "Numerical solution of initial boundary value problems involving Maxwell's equations in isotropic media" proposed by Kane Yee (16), describes mathematical methods to solve initial and boundary problems with Maxwell's equations.
The time-dependent equation in differential and integral form are:

a) Faraday's Law:

$$\frac{\partial B}{\partial t} = -\nabla \times E - M$$

$$\frac{\partial}{\partial t}\iint_A B\, dA = -\oint_L E\, dL - \iint_A M\, dA$$

Equation 22

In which "E" is the electric field (Volt/m) considering dL that is the differential length vector that characterize contour "L" (m^2) , "M" represent the equivalent magnetic current density (Volt/m) considering dA that is differential normal vector that characterize the surface "A" ; at the end "B" is the magnetic flux density (Wb/m^2), where "Wb" represent the unit of magnetic flux associated to one circuit that can produce 1 Volt of electromotive force if it is reduced to zero a uniform rate in 1 second (22) but also is the total magnetic flux across the surface of 1 m^2 perpendicular to magnetic flux density of 1 Tesla (T), additionally can be expressed in function to Henry (H) unit of measure of electrical inductance and ampere, or in function of Ohm (Ω) and Coulomb (C). Practically:

$$Wb = V\, s = \frac{Kg\, m^2}{s^2\, A} = T\, m^2 = A\, H = \Omega C$$

Equation 23

b) Ampere's law

$$\frac{\partial D}{\partial t} = \nabla \times H - J$$

$$\frac{\partial}{\partial t}\iint_A D\, dA = \oint_L H\, dL - \iint_A J\, dA$$

Equation 24

Where "D" is the electric flux density (C/ m^2), "H" is the magnetic field (A/m) and "J" electrical current density.

c) Gauss' law for electric field

$$\nabla D = 0$$

$$\oiint_A D\, dA = 0$$

Equation 25

d) Gauss' law for magnetic field

$$\nabla B = 0$$

$$\oiint_A B\, dA = 0$$

Equation 26

In case of linear, isotropic and no dispersive materials it is possible linked "D" to "E" and "B" to "H" using:

$$D = \varepsilon E = \varepsilon_r \varepsilon_0 E$$

Equation 27

In which "ε" rapresent the electrical permittivity (Farads/m), "ε_r" the relative permittivity and "ε_0" is the free space permittivity that is $8.85 \cdot 10^{-12}$ (F/m)

$$B = \mu H = \mu_r \mu_0 H$$

Equation 28

And "μ" is the magnetic permittivity (H/m), "μ_r" relative permittivity and "μ_0" is the free-space magnetic permittivity at $4\pi \cdot 10^{-7}$(H/m).

These equations are crucial to describe the EMs behaviors in terms of electric and magnetic field.

Additionally, it is possible do the transition from Maxwell's equation into a set of finite difference equations. Re-writing the previous equations we can obtain:

$$\begin{cases} \nabla \times \vec{E} = -\dfrac{\partial \vec{B}}{\partial t} \\ \nabla \times \vec{H} = \sigma \vec{E} - \dfrac{\partial \vec{D}}{\partial t} \end{cases}$$

Equation 29

$$\begin{cases} \vec{B} = \mu \vec{H} \\ \vec{D} = \varepsilon \vec{E} \end{cases}$$

Equation 30

In which "$\sigma \vec{E}$" take into account the electric loss mechanism that one material can dissipate where "σ" is the electric conductivity (Siemens/m) (23)

It's possible decompose the previous equations into three-dimensional rectangular coordinate system (x, y, z) assuming that σ, μ, ε are parameters time-independent. In this way is possible obtain the basis for the FDTD finding the following six finite difference equations:

$$\begin{cases} \dfrac{\partial E_y}{\partial z} - \dfrac{\partial E_z}{\partial y} = \dfrac{\partial B_x}{\partial t} \\ \dfrac{\partial E_z}{\partial x} - \dfrac{\partial E_x}{\partial z} = \dfrac{\partial B_y}{\partial t} \\ \dfrac{\partial E_x}{\partial y} - \dfrac{\partial E_y}{\partial x} = \dfrac{\partial B_z}{\partial t} \end{cases}$$

Equation 31

$$\begin{cases} \dfrac{\partial H_y}{\partial z} - \dfrac{\partial H_z}{\partial y} = \sigma E_x + \dfrac{\partial D_x}{\partial t} \\ \dfrac{\partial H_z}{\partial x} - \dfrac{\partial H_x}{\partial z} = \sigma E_y + \dfrac{\partial D_y}{\partial t} \\ \dfrac{\partial H_x}{\partial y} - \dfrac{\partial H_y}{\partial x} = \sigma E_z + \dfrac{\partial D_z}{\partial t} \end{cases}$$

Equation 32

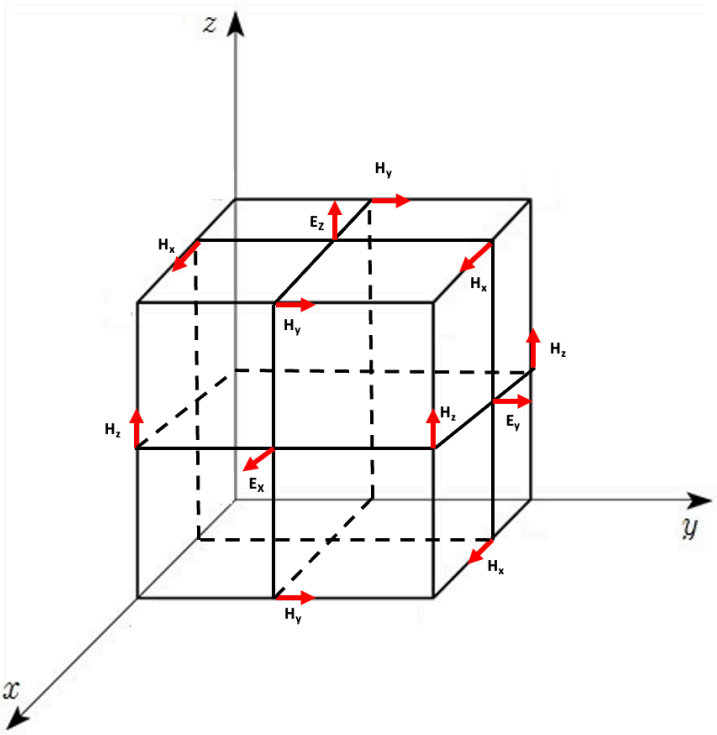

Figure 11: Position of the electric and magnetic field vector components about a cubic unit cell of the Vee space lattice.

As it's possible to see in the previous figure, the region is divided into many smaller regions called cells, in a way that each "E" component is enclosed by four components of "H"; this led to identify the "E" component associated with displacement flux linking "H" loops and, so, to identify the "H" component associated with displacement flux linking "E" loops.
In Yee algorithm aim its "H" and "E" component in time, in a so-called "leapfrog" organization, all computation of "E" in this space are stored for a particular time using the previous "H" output data; and so, all the "H" computation is space are completed and stored using the previous "E" data. The end point is the "time-stepping" that is explicit. (24).
It's possible design the procedure explained for one-dimension wave propagations as follow:

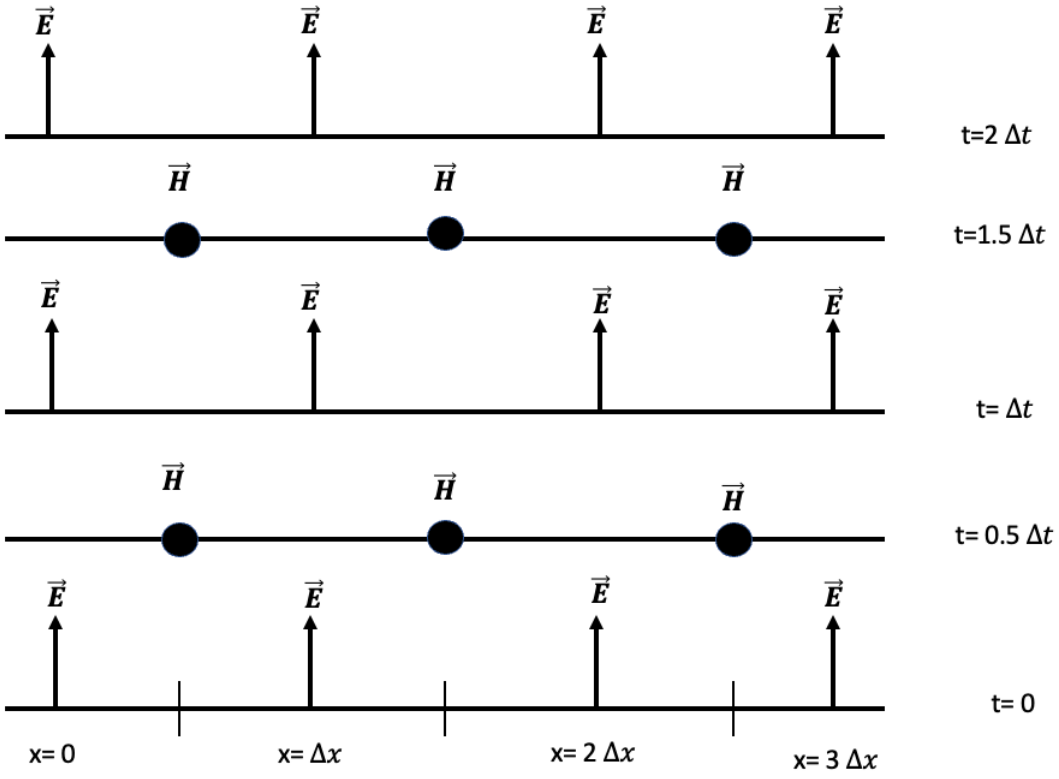

Figure 12: Space-time chart of the Yee algorithm for a one-dimensional wave propagation example showing the use of central differences for the space derivatives and leapfrog for the time derivatives. Initial conditions for both electric and magnetic fields are zero everywhere in the grid.

Here, "Δx", "Δy", "Δz" represents the incrementation in x, y, z direction, and, considering i, j, k as integer, we can obtain the discrete point and the discrete function as:

$$(i\Delta x, j\Delta y, k\Delta z)$$

Equation 33

For discrete-time function, instead, it's evaluated at discrete point inside the gris and considering a discrete point:

$$F|_{i,j,k}^{n} = F(i\Delta x, j\Delta y, k\Delta z, n\Delta t)$$

Equation 34

Yee algorithm uses a central difference equation for both time and space derivation in a way to obtain:

$$\begin{cases} \dfrac{dF}{dx}(i\Delta x, j\Delta y, k\Delta z, n\Delta t) = \dfrac{F|_{i+\frac{1}{2},j,k}^{n} - F|_{i-\frac{1}{2},j,k}^{n}}{\Delta x} + 0((\Delta x)^2) \\ \dfrac{dF}{dy}(i\Delta x, j\Delta y, k\Delta z, n\Delta t) = \dfrac{F|_{i,j+\frac{1}{2},k}^{n} - F|_{i,j-\frac{1}{2},k}^{n}}{\Delta y} + 0((\Delta y)^2) \\ \dfrac{dF}{dz}(i\Delta x, j\Delta y, k\Delta z, n\Delta t) = \dfrac{F|_{i,j,\square\square+\frac{1}{2}}^{n} - F|_{i,j,k-\frac{1}{2}}^{n}}{\Delta z} + 0((\Delta z)^2) \\ \dfrac{dF}{dt}(i\Delta x, j\Delta y, k\Delta z, n\Delta t) = \dfrac{F|_{i,j,k}^{n+\frac{1}{2}} - F|_{i,j,k}^{n-\frac{1}{2}}}{\Delta t} + 0((\Delta t)^2 \end{cases}$$

Equation 35

As we can see it's represented the increment $\pm\frac{1}{2}$ denoting the finite difference over $\Delta x, \Delta, y, \Delta z, \Delta n$ in a way to obtain a central difference taking in consideration the central difference to respectively right and left position respect the point of observations. The goal is obtaining the alternations between E and H's components inside the spatial grid, to be more specific he obtained the difference of two component of E separated by "Δx", " Δy", " Δz" respectively for $\pm\frac{1}{2}\Delta x$, $\pm\frac{1}{2}\Delta, y$, $\pm\frac{1}{2}\Delta z$ and the same for H's components. In case of time, Yee wants to intersperse E and H components in an interval of $\pm\frac{1}{2}\Delta t$ to implement the "leapfrog" algorithm. The aim of this kind of procedure is to obtain the easiest formula for numeric approximation of partial derivatives that load a correct evolution of H and E in time field.

The discretization of H component and E component are respectively:

$$\begin{cases} H_x|_{i,j,k}^{n+\frac{1}{2}} = H_x|_{i,j,k}^{n-\frac{1}{2}} + \dfrac{\Delta t}{\mu_{i,j,k}}\left(\dfrac{E_y|_{i,j,k+\frac{1}{2}}^{n} - E_y|_{i,j,k-\frac{1}{2}}^{n}}{\Delta z} - \dfrac{E_z|_{i,j+\frac{1}{2},k}^{n} - E_z|_{i,j-\frac{1}{2},k}^{n}}{\Delta y}\right) \\ H_y|_{i,j,k}^{n+\frac{1}{2}} = H_y|_{i,j,k}^{n-\frac{1}{2}} + \dfrac{\Delta t}{\mu_{i,j,k}}\left(\dfrac{E_z|_{i+\frac{1}{2},j,k}^{n} - E_z|_{i-\frac{1}{2},j,k}^{n}}{\Delta x} - \dfrac{E_x|_{i,j,k+\frac{1}{2}}^{n} - E_x|_{i,j,k-\frac{1}{2}}^{n}}{\Delta z}\right) \\ H_z|_{i,j,k}^{n+\frac{1}{2}} = H_z|_{i,j,k}^{n-\frac{1}{2}} + \dfrac{\Delta t}{\mu_{i,j,k}}\left(\dfrac{E_x|_{i,j+\frac{1}{2},k}^{n} - E_x|_{i,j-\frac{1}{2},k}^{n}}{\Delta y} - \dfrac{E_y|_{i+\frac{1}{2},j,k}^{n} - E_y|_{i-\frac{1}{2},j,k}^{n}}{\Delta x}\right) \end{cases}$$

Equation 36

And, finally, for E component:

$$\begin{cases} E_x|_{i,j,k}^{n+\frac{1}{2}} = E_x|_{i,j,k}^{n-\frac{1}{2}} + \dfrac{\Delta t}{\mu_{i,j,k}}\left(\dfrac{H_y|_{i,j,k+\frac{1}{2}}^{n} - H_y|_{i,j,k-\frac{1}{2},}^{n}}{\Delta z} - \dfrac{H_z|_{i,j+\frac{1}{2},k}^{n} - H_z|_{i,j-\frac{1}{2},k}^{n}}{\Delta y}\right) \\ E_y|_{i,j,k}^{n+\frac{1}{2}} = E_y|_{i,j,k}^{n-\frac{1}{2}} + \dfrac{\Delta t}{\mu_{i,j,k}}\left(\dfrac{H_z|_{i+\frac{1}{2},j,k}^{n} - H_z|_{i-\frac{1}{2},j\ k}^{n}}{\Delta x} - \dfrac{H_x|_{i,j,k+\frac{1}{2}}^{n} - H_x|_{i,j,k-\frac{1}{2}}^{n}}{\Delta z}\right) \\ E_z|_{i,j,k}^{n+\frac{1}{2}} = E_z|_{i,j,k}^{n-\frac{1}{2}} + \dfrac{\Delta t}{\mu_{i,j,k}}\left(\dfrac{H_x|_{i,j+\frac{1}{2},k}^{n} - H_x|_{i,j-\frac{1}{2},k}^{n}}{\Delta y} - \dfrac{H_y|_{i+\frac{1}{2},j,k}^{n} - H_y|_{i-\frac{1}{2},j,k}^{n}}{\Delta x}\right) \end{cases}$$

Equation 37

With these two systems of equations it is possible to obtain and define, in any point of space grid, the component of H and E, and it's possible to define the evolution of the EM field at each point and for each sampling time.

1.3.2 Numerical Stability and Boundary Conditions

The choice of increments in terms of both space and time ($\Delta x, \Delta y, \Delta z, \Delta t$) can affect the velocity propagation of waves.
Considering one dimension wave propagation:

$$\frac{d^2u}{d^2t} = c^2 \frac{d^2u}{d^2x}$$

Equation 38

Where "u" is in function of space and time, so:

$$u = u\,(x, t)$$

Equation 39

The basic idea is that "the wave propagation solution is stable if it produces a bounded result given a bounded input; the solution is unstable if it produces an unbounded result given a bounded input." (25)
Numeric instability is an unwanted result due to an increasing result defined without any limit during the time under considerations. Meaning that if we assume that each term is limited, each resultant term will be limited for each sample of time; considering the linear system, this means that the total error, represented by the sum of all the error terms, will be always limited.
Specifically, the one-dimension wave propagation equation, in a uniform grid, is exact, instead, considering two-dimensions and three-dimension the wave propagations affect the numerical dispersion in term of wavelength, direction of wave in the grid and grid discretization. (26)

The numeric error dispersion is in function of:

1. Physical phase Velocity error: it refers to the difference between numerical velocity defined using finite-difference algorithm and the real velocity in a continuous domain. The phase velocity refers to the velocity in which the wave, with a proper frequency, propagates in space; the associated error refers when the two velocities (numeric and real) are different, that can be due to an unappropriated discretization of grid and same approximation during the execution of algorithm. This kind of error can affect the precision and accuracy of numeric simulations, in the worst case this leads to a distortion of wave shape. To mitigate the error, it's necessary to use appropriate discretization and use an accurate algorithm to model the wave shape. (15) (27) (28)

2. Velocity-anisotropy error: it refers to discrepancies between propagation velocity defined by the FDTD and the real one but taking the anisotropy features of a medium propagator. In our context the term "anisotropy" refers to the dependency between velocity propagation wave and space directions; in this kind of medium the velocity of wave propagation can change considering the specific orientation of the medium. This error can lead to distortions in the shape of wave and deviations respect the auspicated one. To mitigate the velocity-anisotropy error it's important to consider the characteristics of the medium and adjust the algorithm in function of its. (27) (15) (28)

At the end, the discretization of the grid must guarantee computational stability and accuracy.

If we consider the situation in which $\Delta x = \Delta y = \Delta z$, considering the system linear we obtain the accuracy increase under the consideration that:

$$\Delta x = \frac{\lambda_{min}}{10}$$

Equation 40

And the stability is defined considering Courant-Friedrichs-Levy (CFL)-criterion, Practically, we obtain the following equation under the same consideration: (29)

$$\Delta t \leq \frac{1}{c_0\sqrt{\left(\frac{1}{\Delta x}\right)^2+\left(\frac{1}{\Delta y}\right)^2+\left(\frac{1}{\Delta z}\right)^2}} = \frac{1}{c_0\frac{\sqrt{3}}{(\Delta x)}} = \frac{\Delta x}{c_0\sqrt{3}}$$

Equation 41

And considering the so-called stability factor (S):

$$S = \frac{c_0\Delta t}{\Delta x} = \frac{1}{\sqrt{3}}$$

Equation 42

All this means that if we have a higher value of "S" we will have low iterations and divergent results, also means that the algorithm must have more velocity than the velocity propagation of wavelength. The main problem is related to the generalization due to iteration between the Yee algorithm and the adjustment to have the best model for boundary conditions. (30)
It is important to consider spatial dimensions due to the higher influence in terms of elaboration time and quality. The aim is to minimize undesirables reflections of EM waves that can affect simulation results. The main method used is Absorbing Boundary Conditions (ABC) and it is used to simulate waves that continually propagate in computational fields. (31) traditionally ABC used in FDTD simulation consider Liao boundary conditions (32); practically this technique computes electric component in boundary space interpolating the extrapolation time components and previous spatial component, increasing the order of boundary condition will consider more component of electromagnetic field. (33)
Good choice is to truncate spatial outer during the simulations through a medium absorbent material. (34) Ideally this kind of medium has thickness about only few lattice cells without reflection improving waves for all their frequency spectrum; during the first attempt a medium with dispersion and lossy negligibility was used. The main problem is related to the use of an absorbing layer matched to incident plane waves; this means that it has imitated application in EM. Since 1994 the PML was extended in a way that incident waves considering polarizations and frequency was matched with boundary, this means that PLM

can be used as an absorbing boundary to terminate domain in inhomogeneous, dispersive, nonlinear, and anisotropic medium.
ABC combinations with PML give efficient and robust results but, considering continuous space and the discrete grid FDTD, the electromagnetics parameters are spatially staggered and these lead to error in results and can degrade the behavior of PML.

1.3.3 Advantages and Disadvantages FIT and FDTD methods.

To summarize the two methods under consideration it's possible to analyze advantages and disadvantages for FIT and FDTD.
Referring to the FIT method, it is a method able to transform the integral form of Maxwell's equations to a linear system of equations, it is very similar to FDTD method especially for homogeneous media. FIT method is very accurate and flexible with complex geometrical shape and curve boundaries like FDTD have a simple implementation and parallel architecture. By using the discretization of Maxwell's equation it is able to satisfy the main properties in all the domain fields in inhomogeneous medium (35) but the main problems, like FDTD, are the dependency from time and the using of Yee's algorithm because of, in the first case, the application of time step on grid based on Courante-Friedrich-Levy (CFL) condition, especially for lithography application simulation it is required a small size of grid and so, the time step become significant small and, it means an increasing of computational time. The lithography simulations are essential to optimize and predict the same parameters

as radiation's wavelength, angle of incidence, and the properties of the material affect the definition and accuracy of the structures.

The Yee's algorithm can be considered as a problem because, when we have to do with cartesian mash it is inflexible when the discretization is applied to complex and nonorthogonal structure. (36) To overcome this problem an review extends this method to a variety of applications in electromagnetic field, knowing that the main problem refers to the scattering problem (37) (38) and considering electromagnetic field in the human body. (39)

1.4 Overview of Cole-Cole Equation

When there is an interaction between a magnetic field and the human body, it's crucial to take into account the dielectric properties, as they determine effects arising from the interaction between the two. The main effect is polarization, where, for each moment in time, it is defined as the vector sum of all contributions.

$$P = \sum_{i}^{n} P_i$$

Equation 43

But when there is polarization, there will be a dielectric displacement "D," thus considering the internal electric resistance "E" and the dielectric properties of the material (ε_0):

$$D = \varepsilon_0 \, \mathrm{E} + \mathrm{P}$$

Equation 44

Furthermore, we can state that there is a dependence between polarization and internal electric resistance through "ε_0" and the material's permittivity "ε":

$$P = \varepsilon_0(\varepsilon - 1)E$$

Equation 45

But when it comes to biological tissues, it's necessary to consider the permittivity as a complex parameter "ε*", taking into account both the imaginary part (jε"), represented by power loss, and the real part (ε'), represented by the displacement component. Therefore:

$$\varepsilon^* = \varepsilon' - j\varepsilon''$$

Equation 46

So:

$$\varepsilon'' = \frac{\sigma}{\omega\varepsilon_0}$$

Equation 47

And consequently, it's possible to define the complex dielectric permittivity as the effective complex relative dielectric permittivity:

$$\varepsilon^*_{r\,eff}(\omega) = \varepsilon'_r(\omega) - j\left(\varepsilon''_r(\omega) + \frac{\sigma_{dc}}{\omega\varepsilon_0}\right) = \varepsilon'_r(\omega) - j\left(\frac{\sigma_{dc}(\omega) + \sigma_{dc}}{\omega\varepsilon_0}\right)$$

Equation 48

And thus, the electrical conductivity as:

$$\sigma(\omega) = \sigma_{ac}(\omega) + \sigma_{dc} = \omega\varepsilon_0\,\varepsilon''_r(\omega) + \sigma_{dc}$$

Equation 49

where σ_{dc}(continue) represents the ohmic conductivity arising from the mobility within a specific tissue and σ_{ac} (alternating) represents the losses.

One of the main characteristics of the dielectric spectrum of a biological tissue is its reduction at high frequencies, known as dispersion (α, β, and γ):

- "α" (< 10 kHz) represents low-frequency dispersion, associated with ionic diffusion phenomena present on the cell membrane.
- "β" (> 20 kHz, < 300 GHz) is due to polarization occurring at the cellular level between intracellular and extracellular bodies; other contributions come from protein and macromolecule polarization.
- "γ" (> 1 GHz) occurs when there is polarization due to the presence of water molecules with randomly oriented dipoles in the absence of an external field.

However, each dispersion is characterized by its own time constant called dielectric relaxation time (τ), which is related to frequency as follows:

$$\varepsilon_r^* = \varepsilon_\infty + \frac{\varepsilon_s - \varepsilon_\infty}{1 + j\omega\tau}$$

Equation 50

This is also known as the Debye equation, of which:

$$\varepsilon = \begin{cases} \varepsilon_\infty & \omega\tau \gg 1 \\ \varepsilon_s & \omega\tau \ll 1 \end{cases}$$

Equation 51

However, considering that human models and actual human beings consist of various tissue types, this implies that they will have different dielectric relaxation time constants. Therefore, it's possible to express the previous equation in terms of deviation from Debye behavior, which is also known as the semi-empirical Cole-Cole equation:

$$\varepsilon_r^* = \varepsilon_\infty + \frac{\Delta\varepsilon}{1 + (j\omega\tau)^{1-\alpha}}$$

Equation 52

where the parameter α describes the increase in dispersion.

Mathematically, it's possible to describe the spectrum of a tissue in terms of multiple Cole-Cole dispersions, which is very useful because with a precise choice of parameters associated

with the tissues, it's possible to express the dielectric behavior as a function of the frequency band.

$$\varepsilon_r^* = \varepsilon_\infty + \sum_n \frac{\Delta\varepsilon_n}{1 + (j\omega\tau_n)^{1-\alpha_n}} + \frac{\sigma_{dc}}{j\omega\varepsilon_0}$$

Equation 53

1.5 Specific Absorption Rate

"Specific Absorption Rate" (SAR) is defined as a useful physical quantity to quantifythe amount of energy absorbed by biological tissues as a result of exposure to electromagnetic fields. It relates the absorbed energy to the quantity of tissue and is expressed in W/kg or, less commonly, in mW/g. The fundamental equation that demonstrates this is:

$$SAR = \frac{\Delta P}{\Delta m}$$

Equation 54

Where ΔP represents the absorbed power for a certain volume of tissue (W) and Δm the mass of tissue (kg).

Starting from the previous equation, SAR can be defined as the temporal derivative of the incremental energy absorbed or dissipated by a volume unit characterized by an incremental mass associated with a specific density. (40)

$$SAR = \frac{d}{dt}\left(\frac{dW}{dm}\right) = \frac{d}{dt}\left(\frac{dW}{\rho\, dV}\right)$$

Equation 55

Furthermore, this parameter is dependent on the electric field applied at a point as specified in the following equation:

$$SAR = \frac{\sigma |E|^2}{2\rho}$$

Equation 56

This demonstrates that the specific absorption rate is directly proportional to the square of the effective value of the electric field intensity ($|E|^2$) and the electrical conductivity of the material under consideration (σ), and inversely proportional to the density of the irradiated material. All of this highlights that SAR inherently depends on the geometric characteristics of the space traversed by electromagnetic waves and the position of the body relative to the source (41) but also, on the geometry of the device used as the emitting source. (42) (43)This implies that we won't have a uniform calculation since biological tissues, as in our case, are neither uniform in terms of geometric characteristics nor in terms of electrical conductivity. It suggests that SAR calculation is highly sensitive to the tissue characteristics that compose the analyzed biological area.

Additionally, the calculation of SAR is used to determine the exposure levels of the biological tissues under consideration, thus, evaluating the potential heating of tissues caused by a radiofrequency source. When tissue is exposed to such frequencies, it undergoes heating, resulting in an increase in temperature and heat associated with the tissue. This heating is always dependent on the exposure time, as explained by the following equation:

$$SAR = \frac{c\,\Delta T}{\Delta t}\Big|_{t=0}$$

Equation 57

Where ΔT represents the temperature change (°C), Δt is the exposure duration (s), and c is the specific heat capacity (J/kg °C). However, this assumes that measurements are in ideal conditions, meaning without heat loss due to thermal effects, radiation, or thermoregulation caused by blood flow or sweating. (44)

These considerations are relevant when examining wireless devices or smartphones emitting radiofrequency fields.

It's important to consider "dosimetry" when discussing SAR, which is the analysis of the "dose" of power absorbed by the tissues under consideration. It represents an indirect analysis of the thermal power absorbed by the body or specific body sections, thanks to the intrinsic relationship between SAR and temperature increase. This measurement forms the basis for determining potential undesired effects due to exposure to electromagnetic fields. In general, there are two approaches for calculating SAR:

- Using a numerical method, such as FDTD and FIT, to analyze absorbed power from theory point of view, considering models of electromagnetic field sources and biological bodies.
- Directly measuring the induced field inside the body or body parts under examination, this time starting from real sources.

The calculation of SAR is not unique, and there are three main methods:

1) "Whole-body average," which analyzes SAR considering the entire biological model and considering far-field exposure.
2) "Organ-average" or "body-part" approach, considering the electromagnetic field source close to or at an intermediate position, resulting in partial body exposure. In this case, SAR is analyzed for specific anatomical parts.
3) "Local-average" SAR, considering a specific body part (such as just the head or back) exposed to an extremely nearby field source.

Regarding "local-average" SAR, it can be:

- Calculated for each Yee's algorithm cell within the considered computational space.
- SAR averaged over a certain range of Yee's cells to encompass 1g or 10g of tissue. In practice, SAR is averaged over a small mass sample, as if it were a point, for every 1g or 10g of contiguous tissue or over the entire considered body. (45) (46) (47)

  The calculation of SAR in this case is integrated and averaged over the volume necessary to reach the required amount of tissue. It is represented as follows:

$$SAR = \frac{1}{V}\int_{sample} \frac{\sigma(r)|\vec{E}(\vec{r})|^2}{\rho(r)}\, dr$$

Equation 58

- Calculating the peak averaged SAR, which involves considering only the maximum SAR value within various spatial positions of the body.

Currently, it is possible to assess SAR by using anthropomorphic phantoms made of low-permittivity fiberglass shells filled with an equivalent liquid to replicate the behavior and layering of biological tissues. Typically, an attempt is made to represent "average" tissues to achieve conservative SAR results, meaning slightly overestimated compared to anatomical models. (48)

1.6 Regulations

There are institutions that have established Specific Absorption Rate limits to ensure the safety of individuals from radiofrequency sources, wireless devices, and phones. Unfortunately, universal limits do not exist, but they vary across different parts of the world. For instance, the *Comité Européen de Normalisation Électrotechnique* (CENELEC) represents the European Committee for Electrotechnical Standardization and sets standards in various sectors, including electronic and electrical devices. Specifically, they have established SAR limits for RF exposure in accordance with European directives. CENELEC 1995 and the Telecommunications Technology Council No. 89 defined a SAR limit averaged over 10g of tissue, corresponding to 2 W/kg, based on a maximum exposure of 6 minutes.

It is important to consider the *Federal Communications Commission* (FCC), a US government agency responsible for safeguarding human health that in the late 1990s established SAR exposure limits to protect both workers and non-workers. These limits are based on experiments conducted on 8 rats and 5 monkeys exposed to radiation for 40-60 minutes, resulting in SAR limits of 4 W/kg.

Lastly, we have the *International Commission on Non-Ionizing Radiation Protection* (ICNIRP), which defines exposure limits for non-ionizing radiation, including radiofrequency radiation, for the public and workers. They have specified limits of 0.8 W/kg for 30 minutes of exposure over the whole-body average; 2 W/kg for a 6-minutes exposure in 10 grams of tissue, referencing the head and torso; and 4 W/kg for a 6-minutes exposure, considering 10 grams of tissue, but referencing limbs.

In a more specific context, the ICNIRP standard EN 50361 defines a maximum SAR of 2 W/kg for 10 grams of tissue mass, and the maximum SAR for 1 gram of tissue mass should not exceed 1.6 W/kg, in accordance with the FCC standard C95.3-1999. (49) (22) (50)

The SAR limits provided by these regulatory agencies and organizations can ensure the safety of individuals from exposures to magnetic and RF fields. They are based on assessments of potential health effects while taking into account factors such as exposure duration, frequency, and power. It is also acknowledged that values exceeding these thresholds may have adverse effects. (51).

However, as highlighted by James C. Lin, these limits are often defined in a way that primarily aims to minimize tissue heating. This implies that they might not be applicable to short-duration and low-intensity exposures. Furthermore, these provided limits are based on outdated parameters, thereby limiting their effectiveness in safeguarding children, workers, and non-workers. (48)

2. Materials and Methods

During this study, various interactions between human models and a specifically chosen antenna were analyzed. Concerning the antenna, a typical smartphone antenna operating at 1.8 GHz was selected. Specifically, a PIFA (Planar Inverted-F Antenna) with L-shape was chosen, having identical characteristics for both working environments (FDTD with C language and FIT using CST Studio). Regarding the biological models, representations in the childhood growth phase and an adult woman were selected.

In particular, the interactions between the antenna and human models were examined in two different environments using two distinct methods. The first case utilized the FDTD (Finite-Difference Time-Domain) method programmed in the C language, while the second environment employed CST Studio, which uses the FIT (Finite Integration Technique) method. In this manner, shared features and disparities between the two approaches were also analyzed through a comparison of the computed SAR results.

In both working environments, the same antenna was defined with identical geometric characteristics. However, in the FDTD case, dimension parameterization was required. Subsequently, the geometry and corresponding coordinates of the antenna in three dimensions (x, y, z) were defined to achieve antenna modeling. In the case of CST Studio, on the other hand, antenna parameterization was unnecessary as the software provided a graphical interface. Therefore, only the antenna dimensions (which were the same as in the FDTD case) needed to be defined.

Regarding the Biologic Models that simulate human characteristics, there were different situations. In CST Studio, human models were already implemented in the software. Segmentation of the models was applied to reduce computational complexity. Full body analysis was not performed; only the head-to-midsection of the body was considered. In the FDTD case, the workspace had to be imported. These models were subsequently segmented to obtain dimensions similar to those in the CST Studio case and were visualized using ParaView through specially created .vtk files.

Once the biological models and the antenna for both FIT and FDTD were selected, two types of simulations were performed for each method. A 'test' simulation was conducted, where the field generated by the isolated antenna was simulated. Subsequently, a 'final test' simulation was carried out, considering the biological model to study their interaction.
Subsequently, positions and distances for simulations were defined in both working environments. Specifically, three different interaction positions between the antenna and human models were defined:

1) Interaction between the antenna positioned near the left ear of the biological models.
2) Interaction between the antenna positioned near the mouth of the biological models.
3) Interaction between the antenna positioned near the chest of the biological models.

These three positions were chosen as they are the most common positions while using a smartphone. For each of these positions, three different distances were analyzed: 1mm (short distance), 16mm (medium distance), and 50 mm (long distance).
Subsequently, the average SAR was computed at 1g and 10g for each position and at each distance, and the results were compared.
Following is the block diagram representing the entire procedure conducted during the course of this study.

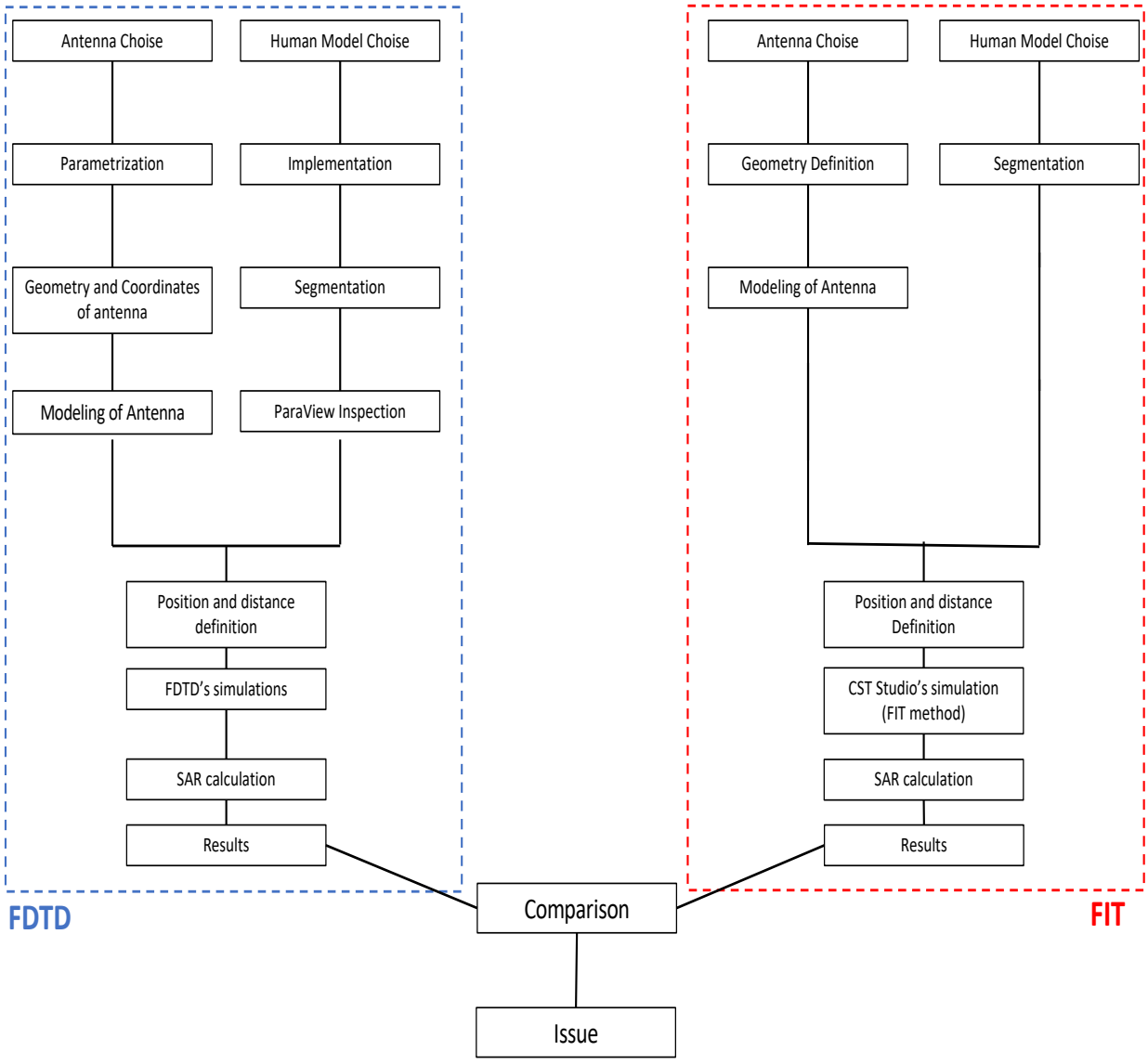

Figure 13: Block diagram of procedure used.

2.1 Antenna Choice

Regarding the antenna selection, as defined in the previous chapter, an L-shaped PIFA antenna was chosen.

For both working environments, the same type of antenna was selected L-shaped PIFA antenna aiming to match the characteristics of our Gold Standard antenna used in Domingo et al. (52).

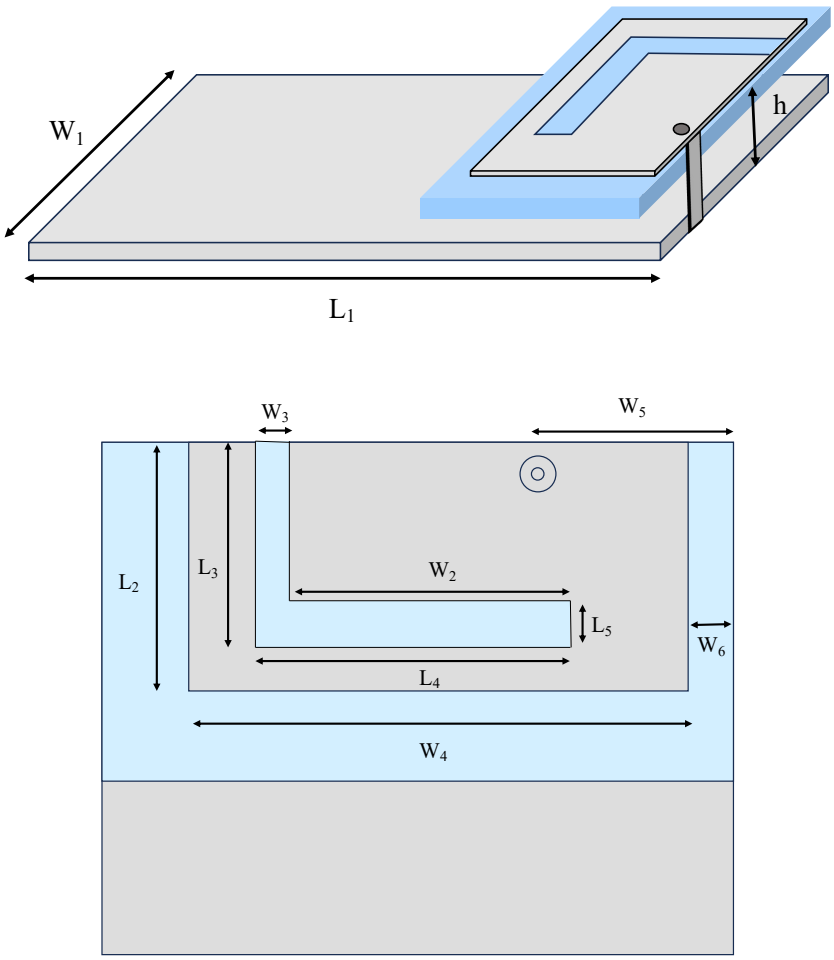

Figure 14: Schematic representation of used antenna (L-shape PIFA).

Dimensions [mm]			*Dimensions [mm]*
L_1 (Ground length)	100	**W_1 (Ground width)**	50
L_3 (Cutout parameter)	16	**W_2 (Cutout parameter width)**	21
L_5 (Vertical cutout width of grosorv)	2.7	**W_3 (Horizontal cutout width of grosorv)**	5
L_2 (Radiation area lenght)	23	**W_4 (Radiation area width)**	40
L_4	39	**W_5**	17
h	8.135	**W_6**	4
h_g (Ground height)	0.6	**h_p (Radiation area height)**	0.035
h_a (Air gap)	5.92	**h_s (Substrate height)**	1.58
h_{ss} (Shorting wall height)	7.5	**W_s (Substrate width)**	50
W_{ss} (Shorting wall width)	1	**L_s (Substate lenght)**	30
L_{ss} (Shorting wall lenght)	0.6		

Table 1: Physical features of used antenna.

Where "L_1" and "W_1" represent the length and width of the patch, respectively, and "h" denotes the height of the antenna. Essentially, this antenna is designed to consist of a ground plate, a dielectric substrate, a patch, a shorting wall, and a feeding point. The feeding point is located at a distance of 17mm (W_5). Additionally, the patch is made of copper and is positioned above the ground plate on a thin dielectric substrate. The chosen dielectric material is an FR-4 substrate, characterized by a dielectric constant (ε_r) of 4.3 and a loss tangent (δ) of 0.025. The main difference between the FDTD and CST Studio simulation lies

in the thickness of the FR-4 substrate. In the FDTD case, the thickness is 2 mm, while in the CST Studio case, it is 1.58 mm.

Regarding the patch material, as mentioned earlier, it is composed of copper with a conductivity of 5.8 × 107 S/m. Similarly, there is a difference in the thickness of the copper material considered in CST and FDTD simulations. Specifically, in the FDTD simulation, the copper thickness is 1 mm, while in the CST simulation, it is 0.035 mm.

Material	*Thickness [mm]*	
	FDTD	***CST***
FR-4	1.58	2
Copper	1	0.035

Table 2: Thickness of material used.

The following figure shows the PIFA antenna with L-shape displayed by CST studio.

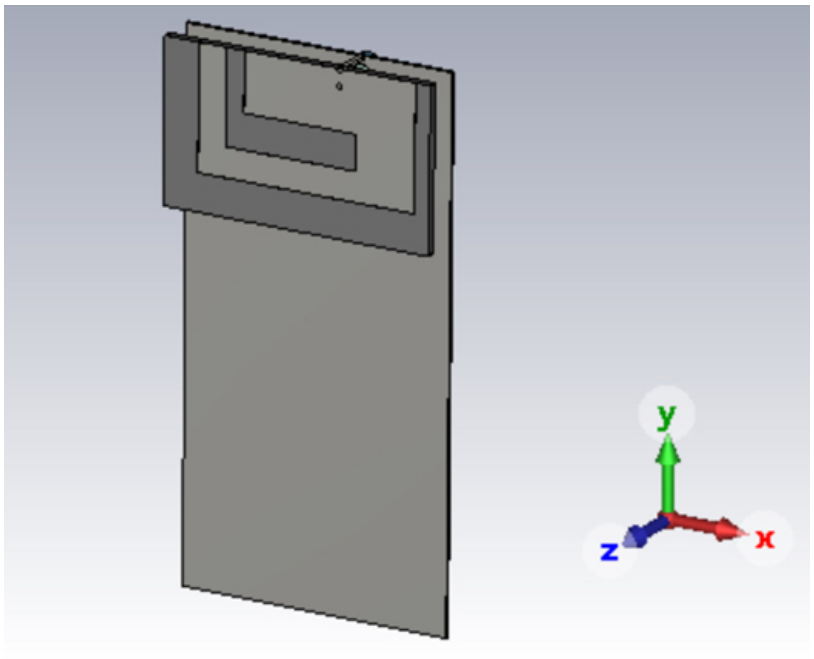

Figure 15: L-shape PIFA antenna on CST Studio Suite.

As mentioned earlier, the assessment of the S_{11} parameter is extremely important, especially during the isolated antenna testing phase. It's important to recall that this parameter is defined as the ratio of the reflected power from the source (P_{ref}) to the incident power on the antenna (P_{in}). Additionally, it's noteworthy that the S_{11} parameter also defines the bandwidth limit. (53). Both working environments emphasize that the antenna's operational frequency is at 1.8 GHz, also displaying a reflection coefficient of -10 dB, a commonly accepted value for effective antenna operation. Below are the S_{11} parameter values for both CST Studio and FDTD code.

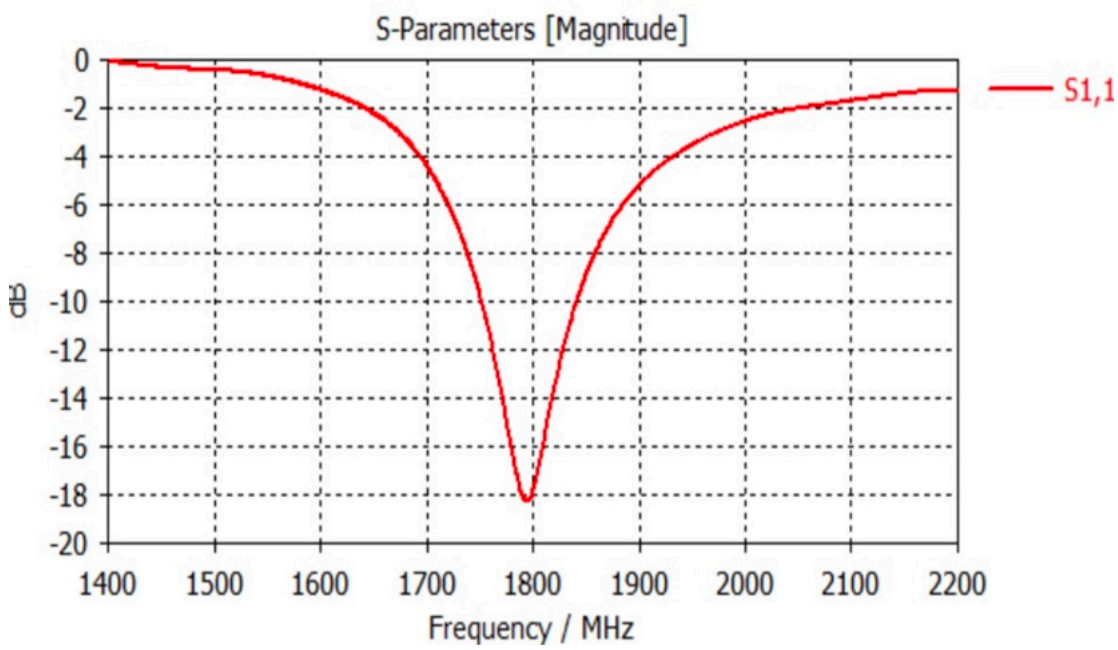

Figure 16: S_{11} parameter of PIFA from the CST Studio Suite software.

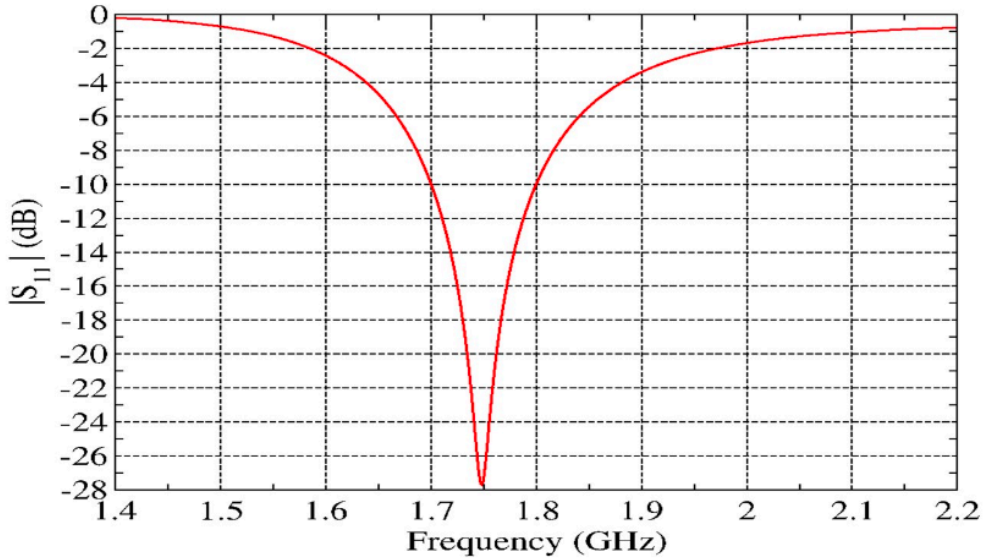

Figure 17: S11 parameter of PIFA from the FDTD code

The difference observed between the two obtained parameters in the two working environments is since in the FDTD code, the size of the elemental cell is 1mm. As a result, we will have different values in the dimensions of the PIFA.

2.2 Biological Models

For our work, computational models of human anatomy were employed, consisting of a numerical representation of the human body also considering the boundaries of internal organs and tissues (54). The initial representations, based on simpler geometric shapes (around the 1960s to 1980s), encompassed features such as the head, neck, arms, legs, and

torso, the latter of which also contained internal organs represented through basic geometric shapes. (55) (56)

Thanks to the invention of machines for Computer Tomography (CT) and Magnetic Resonance Imaging (MRI), it became possible to obtain cross-sectional images of the human body, allowing for high-resolution and accurate visuals of the human body, including internal organs and tissues. These images, after undergoing a segmentation procedure preceded by pre-processing (to eliminate artifacts), form the basis of the databases used for scientific research.

Ultimately, two classes of computational models were developed, one based on surfaces and the other based on voxels, which are composed of pixels from the acquired images. (57) (58) (59)

In reference to the models used in the simulations it was chosen two different human bodies, a 26-year-old woman and a 6-year-old child in case of FDTD; in the second work environments are chosen two different human model trying to be more similar as possible to the first case, in particular, 7-year-old girl, and “Laura’’ model which has a 46-year-old female.

These models were obtained from two different databases.

2.2.1 FDTD’s Biological Models

In the first working environment, which is the case where we used a C programming code to implement FDTD, the biological models used are surface based, implying the use of specific triangular meshes to represent human body tissues. It's crucial to note that these biological models provide an extremely detailed approximation of external tissues and organs.

Two human models were chosen, a 26-year-old woman named "Ella" and a 6-year-old boy named "Thelonious"; these human models were selected from *The Foundation for Research on Information Technologies in Society* (IT'IS), specifically, is an independent organization and non-profit research foundation aimed to improve people's life-quality by improving safety and electromagnetics technology.

These two biological models belong to the Virtual Population (ViP 3.0).

The IT'IS research foundation utilizes various virtual populations, for instance:

- First-generation models (V1) characterized by high precision and a spatial resolution of 1.0x1.0x1.0 mm^3.
- Second-generation models (V2), represent a simplified version compared to the first-generation ones in terms of tissue characterization, as more than 300 tissues are grouped into 22 groups containing the same tissues across all maps (except for the reproductive system).
- For the third-generation maps, each map includes more than 300 anatomical features with a higher spatial resolution of 0.5 × 0.5 × 0.5 mm^3. Improved maps are included, but these models are static, meaning their posture cannot be changed.
- V4 models are based on the third-generation models but include more than 1000 anatomical features and an increased spatial resolution of 0.1 x 0.1 x 0.2 mm^3, implying greater precision even in smaller anatomical parts.

The IT'IS biological models are based on Computed Tomography (CT) and Magnetic Resonance Imaging (MRI) scans that allow two different resolutions of images.

The procedure includes 7 different steps:

1. The volunteer's entire body underwent scanning using MRI technology.
2. The acquired MRI data underwent pre-processing to prepare it for further analysis.
3. The pre-processed MRI images were then subjected to segmentation, a process that involved labeling different regions within the images. This step aimed to distinguish various tissues and structures within the body.
4. Any artifacts present in the images were removed to ensure data quality and integrity.
5. Extracting the surface of the tissues from the processed images, including additional processing steps to refine the surface representation.

6. Rigorous quality control measures were implemented to verify the accuracy and reliability of the generated model which include use of guidelines including same important structures and tissue, also checked by two or more-member teams during the segmentation step and improvements based on feedback members.

By following these steps, the IT'IS foundation successfully generated the human model that was utilized in the FDTD simulation. (59)

Very important to note is that, to visualize our three-dimensional maps, ParaView software was utilized.

It is an open-source software released in 2002 by Kitware; ParaView is employed for scientific analyses characterized by interactive visualization. The files accepted by the software are in ".vtk" format; hence, it was necessary to convert the files in order to have the desired format. Through this process, it becomes possible to obtain a 3D visualization of the desired maps. (60) (61)

Below the ParaView's initial interface.

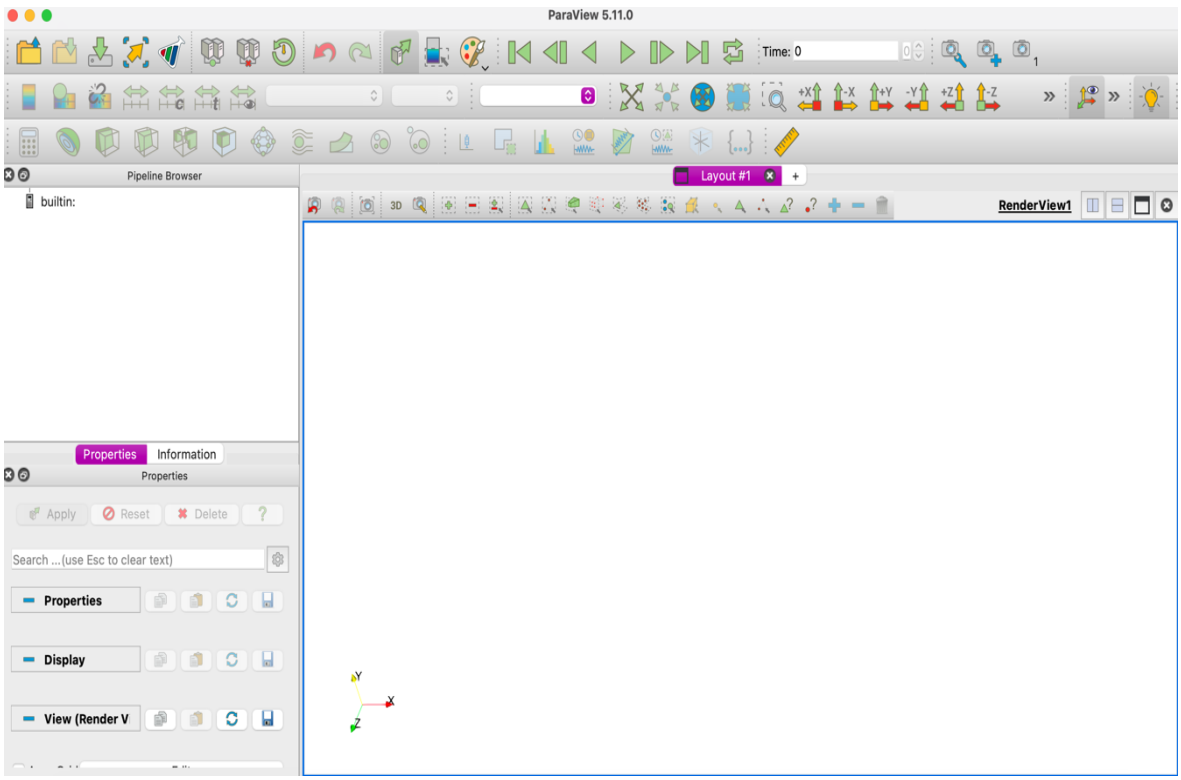

Figure 18: ParaView's initial user interface.

Below are representative images of the biological models used in the FDTD case by using ParaView software.

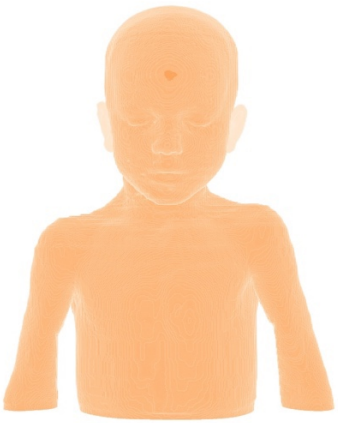

Figure 19: Selected part of Thelonious 'body model used in the simulations.

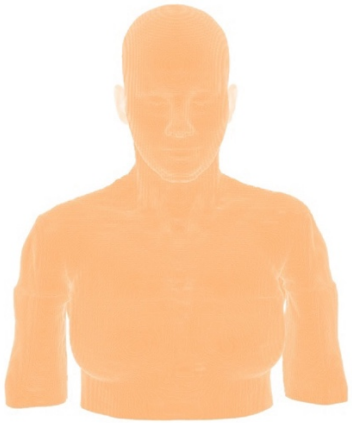

Figure 20: Selected part of Ella 'body model used in the simulations.

The following table represents the main characteristics of the human using FDTD method and includes information such as name, sex, height, weight, Body Mass Index (BMI) and resolutions of models used for the first work environment.

Name	Sex	Age (year)	Height (m)	Weight (Kg)	BMI (Kg/m^2)	Resolution (mm^3)
Thelonious	Male	6	1.16	18.6	13.8	Head: 0.5 x 0.5 x 1.00 Torso: 0.9 x 0.9 x 2.00 Limbs: 0.5 x 0.5 x 0.5
Ella	Female	26	1.63	57.3	21.6	Head: 0.5 x 0.5 x 1.00 Torso: 0.9 x 0.9 x 2.00 Limbs: 0.5 x 0.5 x 0.5

Table 3: Features of used biological model in FDTD case.

In addition, from the Cole-Cole equation it was possible to calculate two of the principal dielectric properties of the tissues (dielectric constant ε, electric conductivity σ) used for both the THELONOUS and ELLA biological models; also, tissue "Occurrences" representing the number of tissue cells considered for the human model studied were reported. But since the exact number of cells is large, this is a qualitative estimation.

Tissues (name)	*ε*	*σ [S/m]*	*Occurrences*
Adrenal Gland	581.423	150.098	2825
Air	1	0	48272
Blood	59.372	204.355	39762
Blood Vessel Wall	433.433	106.578	6844
Bone Marrow (Red)	10.677	0.349118	53603
Brain (Grey Matter)	500.792	13.913	696143
Brain (White Matter)	370.109	0.914958	367761
Bronchi	405.122	111.439	881
Bronchi lumen	1	0	735
Cartilage	402.148	128.693	42741
Cerebellum	461.138	170.894	151785

Cerebrospinal Fluid	672.005	292.359	196914
Commissura Anterior	370.109	0.914958	40
Commissura Posterior	370.109	0.914958	6
Connective Tissue	442.507	120.081	162532
Diaphragm	535.493	134.098	110796
Epididymis	586.054	169.155	0
Esophagus	632.269	169.803	6819
Esophagus Lumen	1	0	3612
Eye (Cornea)	527.678	185.827	295
Eye (Lens)	346.497	0.787477	292
Eye (Sclera)	53.568	160.186	3905
Eye (Vitrous Humor)	685.734	203.248	9222
Fat	110.215	0.190084	436720
Gallbladder	582.136	16.421	6456
Heart Lumen	59.372	204.355	7562
Heart Muscle	563.226	177.123	234581
Hippocampus	500.792	13.913	1982
Hypophysis	581.423	150.098	279
Hypothalamus	581.423	150.098	643
Intervertebral Disc	402.148	128.693	31528
Kidney (Cortex)	544.256	194.958	53993
Kidney (Medulla)	544.256	194.958	33691
Large Intestine	551.483	157.628	29213
Large Intestine Lumen	535.493	134.098	12685
Liver	442.109	128.914	535623
Lung	209.459	0.637143	907738
Mandible	117.805	0.275221	16645
Medulla Oblangata	461.138	170.894	5272
Meniscus	402.148	128.693	0
Midbrain	461.138	170.894	7577
Muscle	535.493	134.098	2173191
Nerve	308.672	0.842923	24099
Pancreas	581.423	150.098	10540
Patella	117.805	0.275221	0
Penis	433.433	106.578	0
Pharynx	1	0	1433
Pineal Body	581.423	150.098	276
Pons	461.138	170.894	12257
Prostate	586.054	169.155	0
SAT (Subcutaneous Fat)	110.215	0.190084	625084

Skin	388.718	118.474	469332
Skull	117.805	0.275221	262595
Small Intestine	559.035	269.598	53152
Small Intestine Lumen	535.493	134.098	20763
Spinal Cord	308.672	0.842923	25855
Spleen	538.476	177.996	121978
Stomach	632.269	169.803	135338
Stomach Lumen	535.493	134.098	130674
Tendon\Ligament	442.507	120.081	33289
Testis	586.054	169.155	0
Thalamus	500.792	13.913	18809
Thymus	581.423	150.098	28931
Tongue	53.568	137.134	37535
Tooth	117.805	0.275221	5687
Trachea	405.122	111.439	4054
Trachea Lumen	1	0	6095
Ureter\Urethra	433.433	106.578	78
Urinary Bladder	183.412	0.535168	0
Vertebrae	117.805	0.275221	126029

Table 4: Dielectric constant and electric conductivity of Thelonious 'tissues.

Tissues (name)	***ε***	***σ [S/m]***	***Occorenze***
Adrenal Gland	581.423	150.098	12796
Air	1	0	69328
Blood	59.372	204.355	146291
Blood Vessel Wall	59.372	204.355	88493
Bone	117.805	0.275221	383823
Bone Marrow (Red)	10.677	0.349118	34195
Brain (Grey Matter)	500.792	13.913	674911
Brain (White Matter)	370.109	0.914958	415609
Breast Fat	526.923	0.0935875	628617
Bronchi	405.122	111.439	7675
Bronchi lumen	1	0	666
Cartilage	402.148	128.693	66357
Cerebellum	461.138	170.894	140852
Cerebrospinal Fluid	672.005	292.359	318332
Commissura Anterior	370.109	0.914958	58
Commissura Posterior	370.109	0.914958	30
Connective Tissue	442.507	120.081	912568
Diaphragm	535.493	134.098	246771
Esophagus	632.269	169.803	26365

Esophagus Lumen	1	0	1903
Eye (Cornea)	527.678	185.827	316
Eye (Lens)	346.497	0.787477	305
Eye (Sclera)	53.568	160.186	4010
Eye (Vitrous Humor)	685.734	203.248	12132
Fat	110.215	0.190084	1170153
Gallbladder	582.136	16.421	13727
Heart Lumen	59.372	204.355	286119
Heart Muscle	563.226	177.123	279109
Hippocampus	500.792	13.913	730
Hypophysis	581.423	150.098	728
Hypothalamus	581.423	150.098	745
Intervertebral Disc	402.148	128.693	108013
Kidney (Cortex)	544.256	194.958	41406
Kidney (Medulla)	544.256	194.958	41320
Large Intestine	551.483	157.628	0
Large Intestine Lumen	535.493	134.098	0
Larynx	402.148	128.693	2533
Liver	442.109	128.914	745106
Lung	209.459	0.637143	2616473
Mandible	117.805	0.275221	35331
Medulla Oblangata	461.138	170.894	7115
Meniscus	402.148	128.693	0
Midbrain	461.138	170.894	7683
Mucous Membrane	438.505	123.206	16087
Muscle	535.493	134.098	6176761
Nerve	308.672	0.842923	1487
Ovary	463.964	181.783	0
Pancreas	581.423	150.098	0
Patella	117.805	0.275221	0
Pharynx	1	0	6054
Pineal Body	581.423	150.098	161
Pons	461.138	170.894	11636
SAT (Subcutaneous Fat)	110.215	0.190084	2468301
Skin	388.718	118.474	12237
Skull	117.805	0.275221	521820
Small Intestine	559.035	269.598	0
Small Intestine Lumen	535.493	134.098	0
Spinal Cord	308.672	0.842923	19576
Spleen	538.476	177.996	163225
Stomach	632.269	169.803	270948
Stomach Lumen	535.493	134.098	163029
Tendon\Ligament	442.507	120.081	11291

Thalamus	500.792	13.913	13208
Thymus	581.423	150.098	19366
Thyroid Gland	581.423	150.098	12427
Tongue	53.568	137.134	60186
Tooth	110.215	0.190084	2468301
Trachea	405.122	111.439	14000
Trachea Lumen	1	0	3816
Ureter\Urethra	433.433	106.578	0
Urinary Bladder	183.412	0.535168	0
Uterus	589.366	176.418	0
Vagina	551.483	157.628	0
Vertebrae	117.805	0.275221	323271

Table 5: Dielectric constant and electric conductivity of Ella's tissues.

As previously mentioned, once the biological models were selected and their characteristics were analyzed, simulations were carried out.

Regarding the FDTD simulations, they concern the interactions between the PIFA antenna (described in the previous chapter) and the biological maps of "Thelonious" and "Ella". Three interaction modes were decided upon, each at three different distances:

1) Left ear at distances of 1 mm, 16 mm, 50 mm
2) Mouth at distances of 1 mm, 16 mm, 50 mm
3) Chest at distances of 1 mm, 16 mm, 50 mm

Each of these different cases involves different positions, and therefore the use of coordinates in three dimensions (x, y, z), represented in the following tables, where each table corresponds to the distance between the antenna and the biological model for the ear, mouth, and chest interactions.

Distance between antenna and Thelonious human model	Coordinates (x, y, z)
1 mm	(307, 122, 105)
16 mm	(323, 122, 105)
50 mm	(357, 122, 105)

Table 6: Coordinates of Thelonious case ear.

Distance between antenna and Thelonious human model	Coordinates (x, y, z)
1 mm	(212, 291, 182)
16 mm	(228, 291, 182)
50 mm	(262, 291, 182)

Table 7: Coordinates of Thelonious case mouth.

Distance between antenna and Thelonious human model	Coordinates (x, y, z)
1 mm	(266, 186, 263)
16 mm	(282, 186, 263)
50 mm	(316, 186, 263)

Table 8: Coordinates of Thelonious case chest.

Distance between antenna and Ella human model	Coordinates (x, y, z)
1 mm	(249, 123, 140)
16 mm	(265, 123, 140)
50 mm	(299, 123, 140)

Table 9: Coordinates of Ella case ear.

Distance between antenna and Ella human model	Coordinates (x, y, z)
1 mm	(257, 314, 219)
16 mm	(273, 314, 219)
50 mm	(307, 314, 219)

Table 10: Coordinates of Ella case mouth.

Distance between antenna and Ella human model	Coordinates (x, y, z)
1 mm	(351, 215, 383)
16 mm	(367, 215, 383)
50 mm	(401, 215, 383)

Table 11: Coordinates of Ella case chest.

2.2.2 CST's Biological Models

The second working environment for our simulations is CST Studio Suite.

The latter is a software used for designing, optimizing, and analyzing 3D electromagnetic systems and their components. Common subjects of analysis and design include antennas, electromagnetic compatibility, including potential interference, and, as in our case, human body exposure to electromagnetic fields.

CST is employed by many engineering companies around the world as it allows for the facilitation and reduction of the product development cycle, optimizing parameters, and addressing potential issues identified during the design phase.

This software can perform simulation starting from Time Domain (TD) to two high frequency time domain solvers. TD measures the development of field trough time at discrete location and at discrete time by considering the energy transmitted between different port or excitation sources either in open space or in closed one; so, TD solution is considered as a robust method for frequency application able to obtain entire frequency behavior of device under consideration.

The two frequencies time domain solver are the Finite Integration Technique (FIT) or Transient solver, the second one is based on Transmission Line Method (TLM) or TLM solver that allows the analysis in time domain based on hexahedral mash.

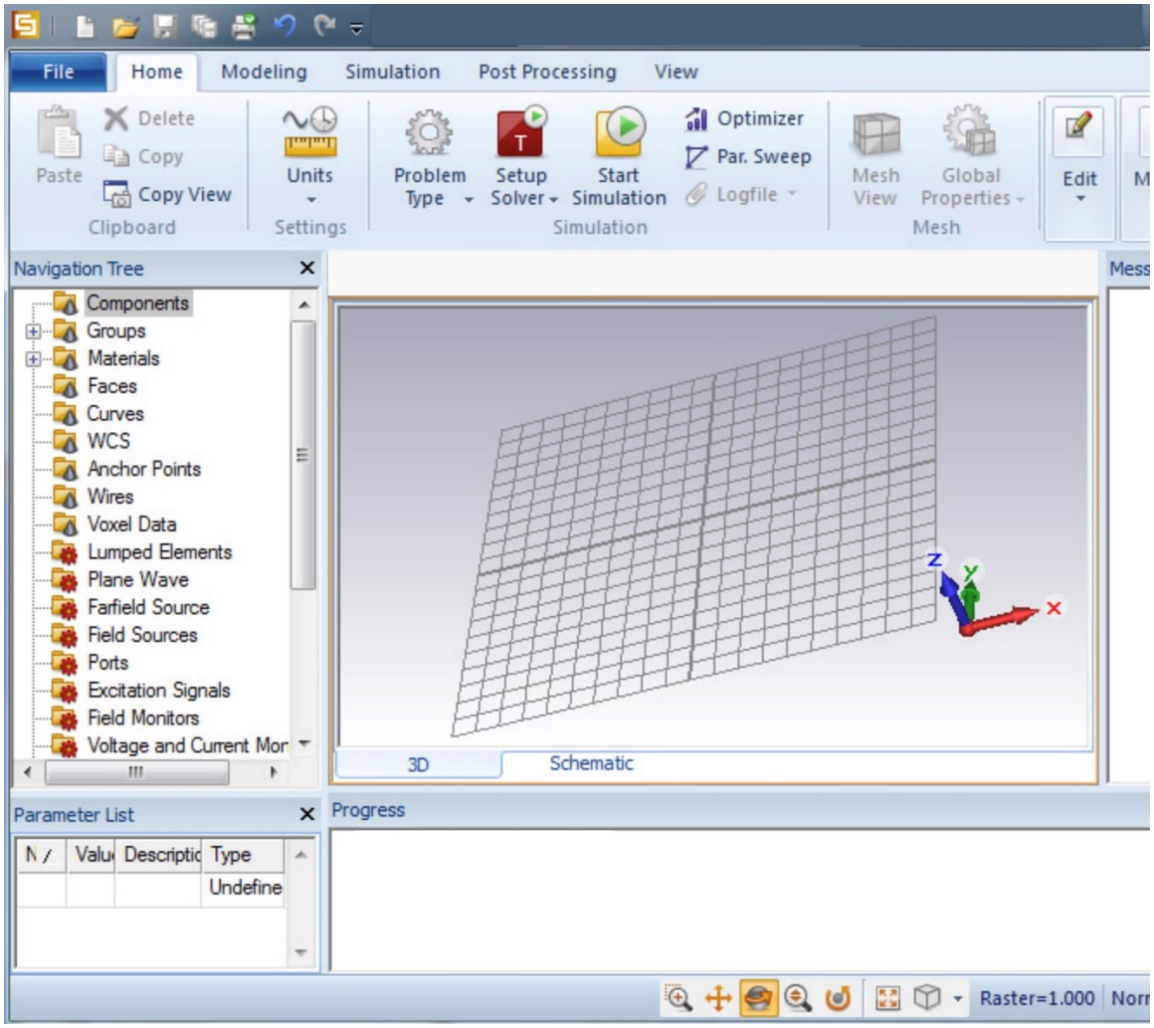

Figure 21: Typical initial interface of CST Studio Suite

The human models used in this case belong to the "CST Voxel Family," which is a group of eight distinct maps simulating eight different human models in terms of height, age, and gender. In this case, the biological models are already included within the software, so there was no need to implement the maps as in the previous case.

These models are voxel-based biological models, which means they are created from pixel data within two-dimensional medical images (obtained through CT or MR scans) and transformed into three-dimensional volumetric elements. Each voxel is filled with a unique substance associated with an identifying number that represents a specific tissue or organ. Furthermore, these biological models encompass up to 135 elements, including organs and

tissues, spread across 2-5 million voxels. They have a wide range of uses, including simulations of radiation therapies and exposures to ionizing radiation. (55) (62)

For our work, two models were selected:

1. 'Child', a 7-year-old girl
2. 'Laura', a 46-year-old woman

Below are the images of the girl and woman used in the CST simulations, along with a table featuring the main characteristics of the models (name, height, weight, body mass index, and resolution).

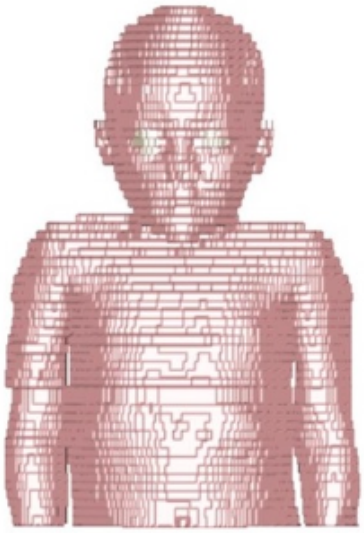

Figure 22: Selected part of Child 's body model used in the simulations.

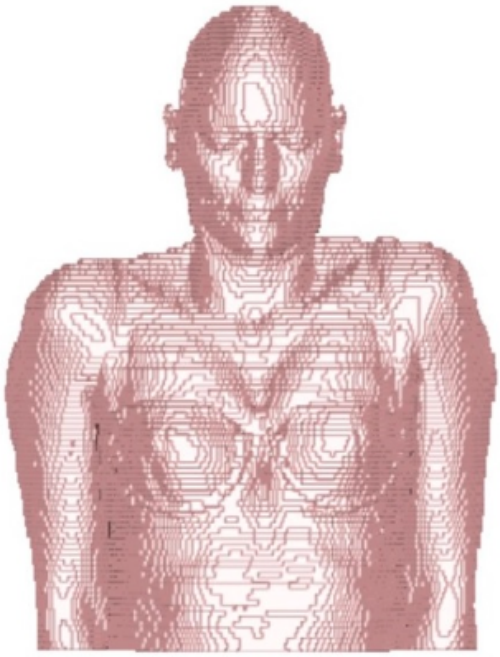

Figure 23: Selected part of Laura's body model used in the simulations.

Name	Sex	Age (year)	Height (m)	Weight (Kg)	BMI (Kg/m^2)	Resolution/mm
Child	Female	7	1.15	21.7	16,41	1.54 × 1.54 × 8.0
Laura	Female	43	1.63	51	19.2	1.875 × 1.875 × 5.0

Figure 24: Features of used biological model in FDTD case.

In this case as well, once the biological models were set, it was necessary to place them relative to the PIFA antenna. To position the biological models, a combination of translation and rotation relative to the PIFA was selected, each characterized by three-dimensional coordinates. The following tables represent the coordinates used at each distance (1 mm, 16 mm, 50 mm) for rotation and translation relative to the antenna in ear, mouth and chest cases.

Distance between antenna and Child human model	Coordinates (x, y, z)
1 mm	*TRASLATION*: (-80, -95, -428)
	ROTATION: (0,90,1020)
16 mm	*TRASLATION*: (-80, -95, -444)
	ROTATION: (0,90,1020)
50 mm	*TRASLATION*: (-80, -95, -478)
	ROTATION: (0,90,1020)

Table 12: Coordinates of Child case ear.

Distance between antenna and Child human model	Coordinates (x, y, z)
1 mm	*TRASLATION*: (0, -170, -393)
	ROTATION: (0,90,180)
16 mm	*TRASLATION*: (0, -186, -393)
	ROTATION: (0,90,180)
50 mm	*TRASLATION*: (0, -220, -393)
	ROTATION: (0,90,180)

Table 13: Coordinates of Child case mouth.

Distance between antenna and Child human model	Coordinates (x, y, z)
1 mm	*TRASLATION*: (-30, 15, -395)
	ROTATION: (0,0,0)
16 mm	*TRASLATION*: (-30, 15, -409)
	ROTATION: (0,0,0)
50 mm	*TRASLATION*: (-30, 15, -445)
	ROTATION: (0,0,0)

Table 14: Coordinates of Child case chest.

Distance between antenna and Laura human model	Coordinates (x, y, z)
1 mm	*TRASLATION*: (-135, -135, -635)
	ROTATION: (0,90,1020)
16 mm	*TRASLATION*: (-135, -135, -651)
	ROTATION: (0,90,1020)
50 mm	*TRASLATION*: (-135, -135, -685)
	ROTATION: (0,90,1020)

Table 15: Coordinates of Laura case ear.

Distance between antenna and Laura human model	Coordinates (x, y, z)
1 mm	*TRASLATION*: (40, -205, -707)
	ROTATION: (0,90,180)
16 mm	*TRASLATION*: (40, -221, -707)
	ROTATION: (0,90,180)
50 mm	*TRASLATION*: (40, -255, -707)
	ROTATION: (0,90,180)

Table 16: Coordinates of Laura case mouth.

Distance between antenna and Laura human model	Coordinates (x, y, z)
1 mm	*TRASLATION*: (-45, 0, -627)
	ROTATION: (10,0,0)
16 mm	*TRASLATION*: (-45, 0, -643)
	ROTATION: (10,0,0)
50 mm	*TRASLATION*: (-45, 0, -677)
	ROTATION: (10,0,0)

Table 17: Coordinates of Laura case chest.

3. Results

In this section, all the results obtained from the conducted simulations will be presented, including images and tables of the outcomes achieved in the interaction between the antenna and the biological models, both in the FDTD and CST (using the FIT method) cases.
The purpose of this study is to calculate Specific Absorption Rate (SAR) values (averaged over 1g and 10g tissue masses) using the FDTD and FIT methods, simulating various positions at different distances.

Specifically, in this section, we will compare the results obtained between FDTD and CST Studio Suite, first for the case of the child biological model (using "Thelonious" and "Child"), and subsequently for the case of the female biological model ("Ella" and "Laura"). We will analyze the SAR averaged over 1g and 10g for interactions near the left ear (at 1mm, 16mm, and 50mm distances), followed by interactions near the mouth of the biological models (at 1mm, 16mm, and 50mm), and finally interactions near the chest area (at 1mm, 16mm, and 50mm distances).
Subsequently, tables will be presented with the obtained values for all the analyzed cases.
After that, we will be analyzing the absorbed power by tissues only considering the FDTD case.

3.1 Babies' Cases

In this section, the case of child human models ("Thelonious" in the FDTD case and "child" in the CST Studio case) is analyzed by calculating their SAR averaged over both 1g and 10 of tissue. This is done for scenarios in which the antenna is positioned near the left ear, mouth, and chest, respectively.

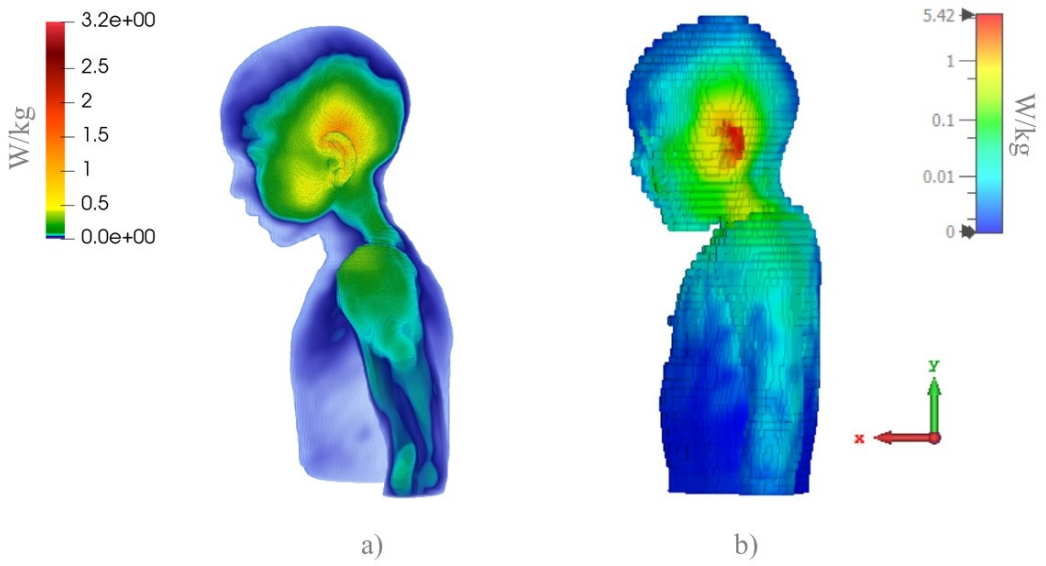

Figure 25: Comparison of 1 g SAR simulation results for antenna position (1 mm) by child ear in: a) FDTD code, b) CST Studio Suite.

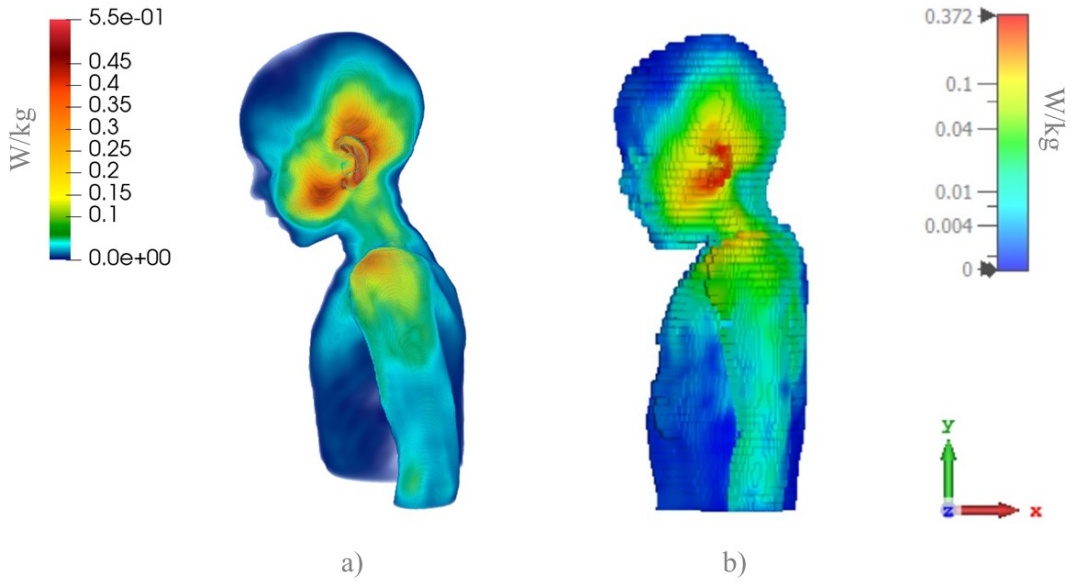

Figure 26: Comparison of 1 g SAR simulation results for antenna position (16 mm) by child ear in: a) FDTD code, b) CST Studio Suite.

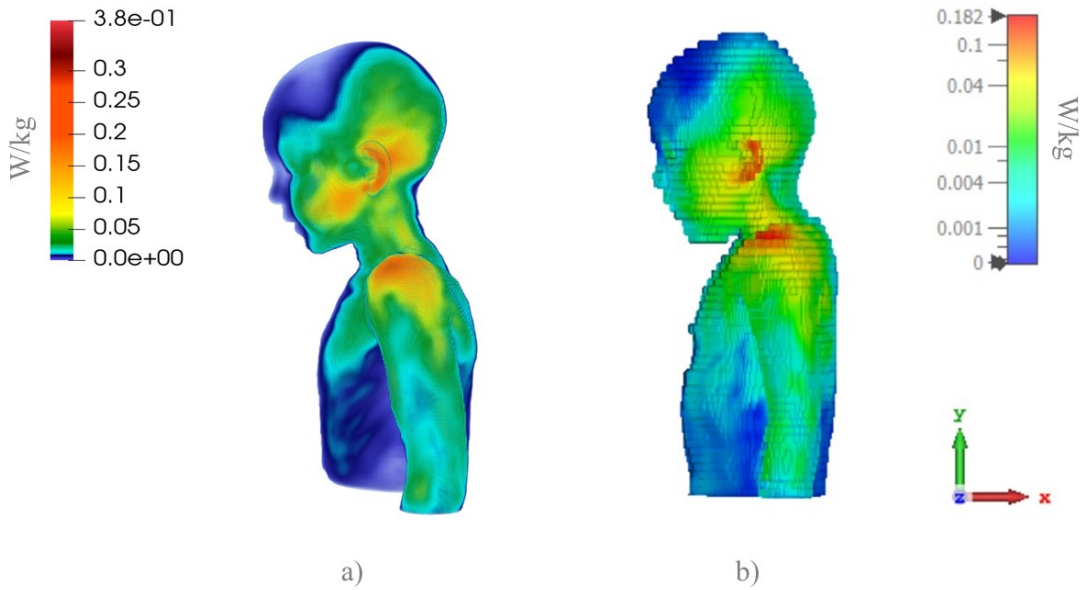

Figure 27: Comparison of 1 g SAR simulation results for antenna position (50 mm) by child ear in: a) FDTD code, b) CST Studio Suite.

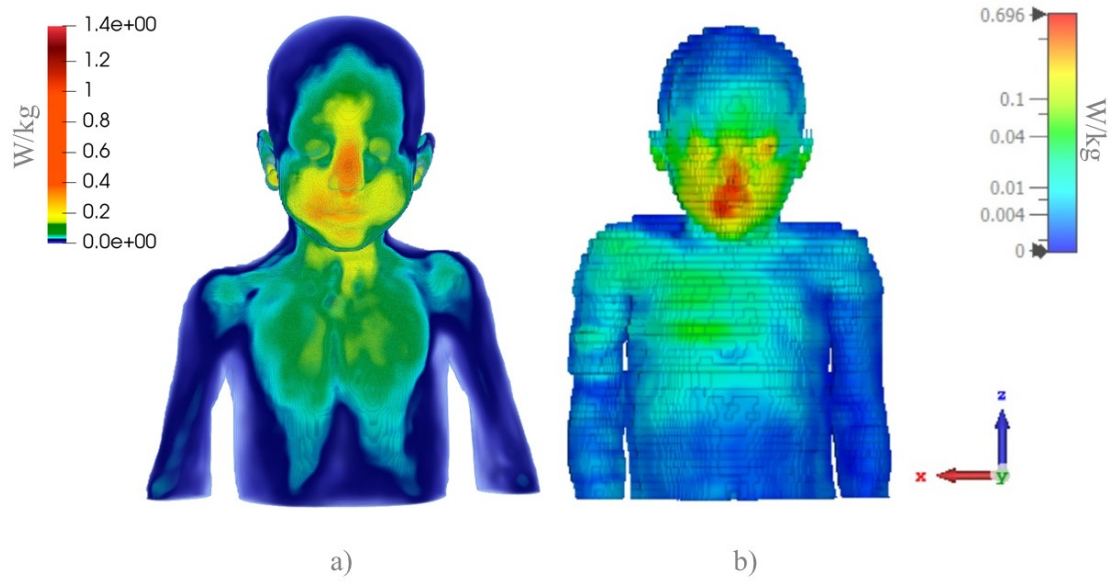

Figure 28: Comparison of 1 g SAR simulation results for antenna position (1 mm) by child mouth in: a) FDTD code, b) CST Studio Suite.

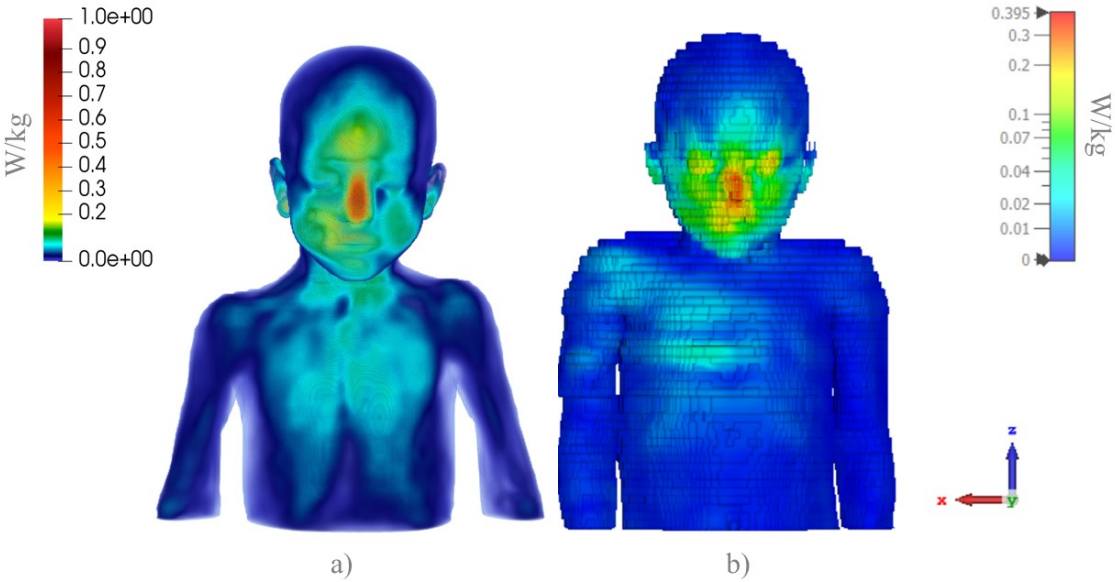

Figure 29: Comparison of 1 g SAR simulation results for antenna position (16 mm) by child mouth in: a) FDTD code, b) CST Studio Suite.

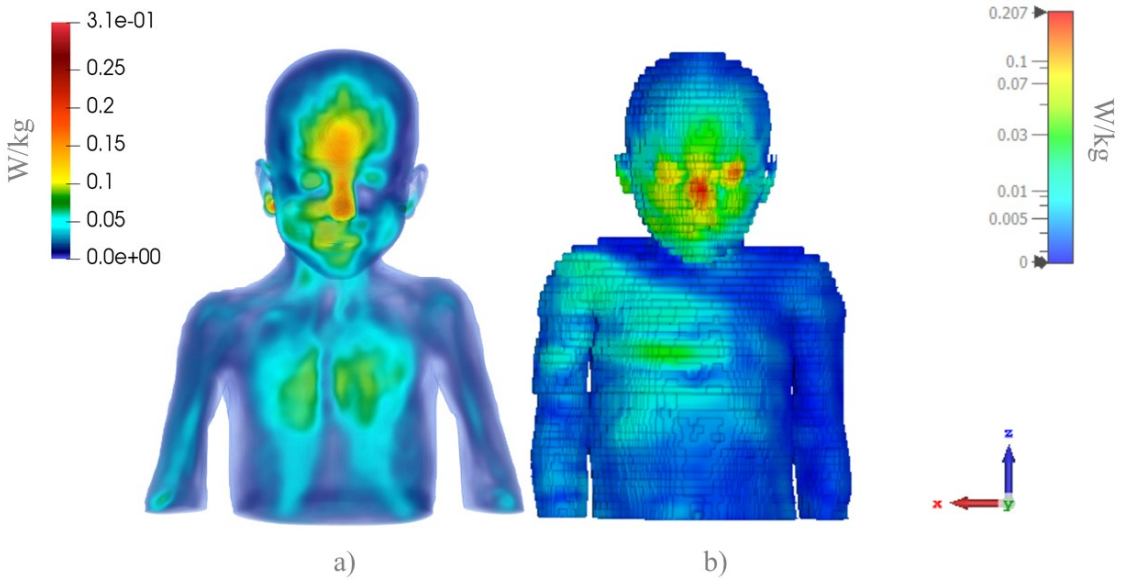

Figure 30: Comparison of 1 g SAR simulation results for antenna position (50 mm) by child mouth in: a) FDTD code, b) CST Studio Suite.

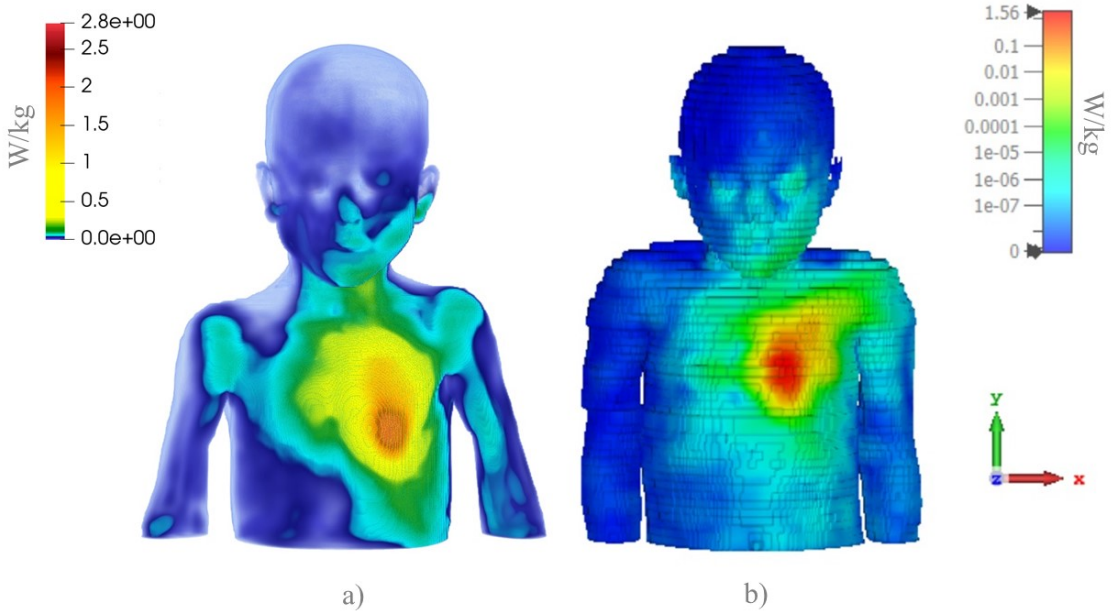

Figure 31: Comparison of 1 g SAR simulation results for antenna position (1 mm) by child chest in: a) FDTD code, b) CST Studio Suite.

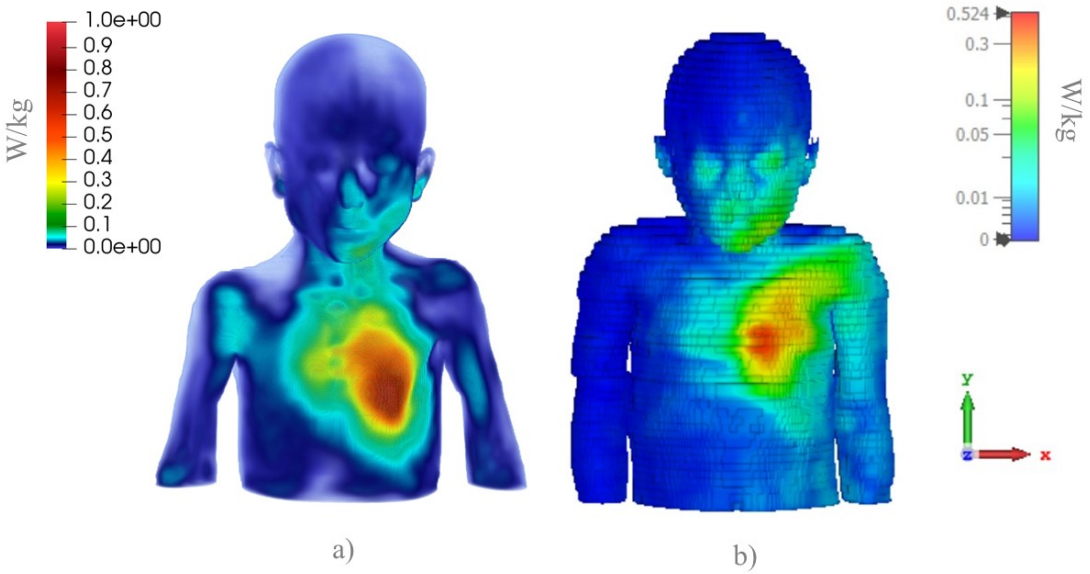

Figure 32: Comparison of 1 g SAR simulation results for antenna position (16 mm) by child chest in: a) FDTD code, b) CST Studio Suite.

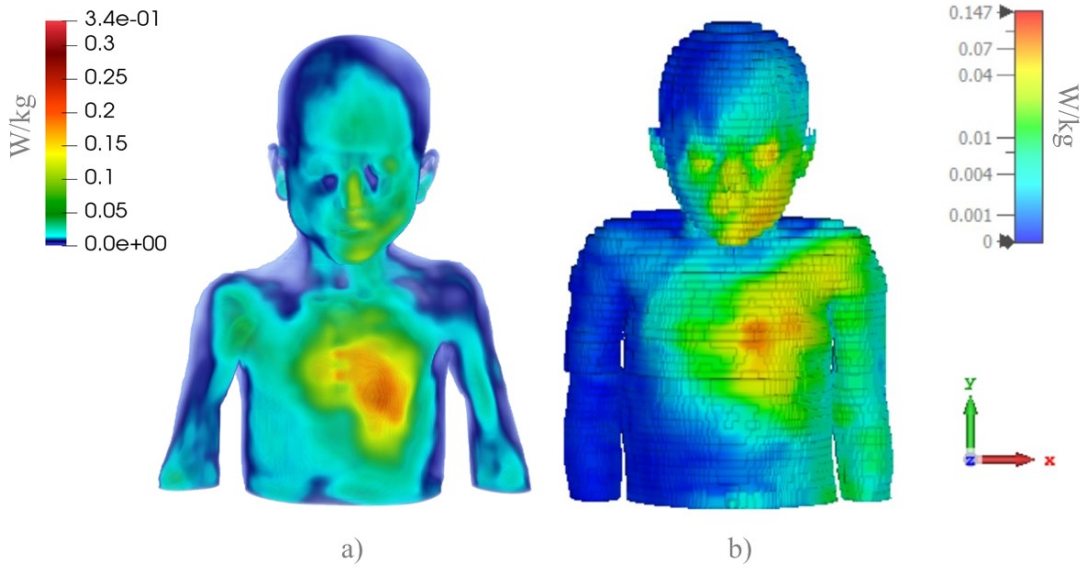

Figure 33: Comparison of 1 g SAR simulation results for antenna position (50 mm) by child chest in: a) FDTD code, b) CST Studio Suite.

Subsequently, a table and a histogram were presented depicting the maximum SAR (1g) values for both the FDTD and CST cases across all the positions and distances considered.

Location of PIFA	*SAR [W\kg]*					
	1 mm		*16 mm*		*50 mm*	
	FDTD	**CST**	**FDTD**	**CST**	**FDTD**	**CST**
Ear	3.180	5.51	1.042	1.321	0.378	0.452
Mouth	1.431	0.698	1.025	0.553	0.312	0.301
Chest	2.836	1.557	1.013	0.534	0.339	0.149

Table 18: Comparison of the results for child body model in case of SAR 1 g.

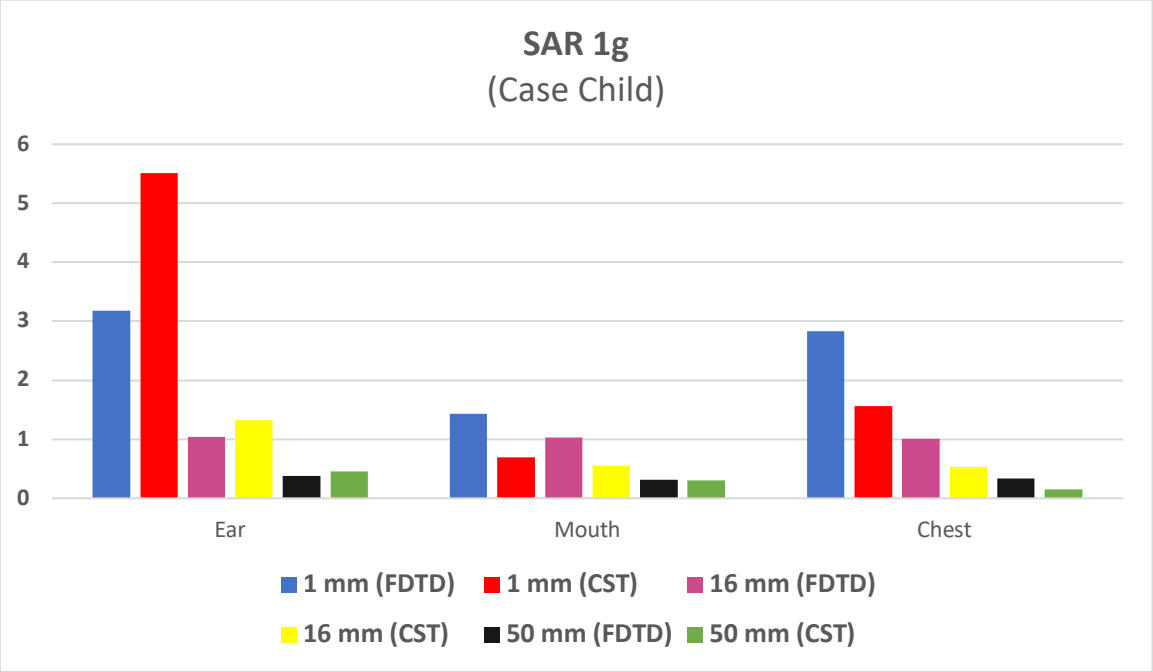

Figure 34: Histogram about comparison of the results for the child body model in case of SAR 1 g.

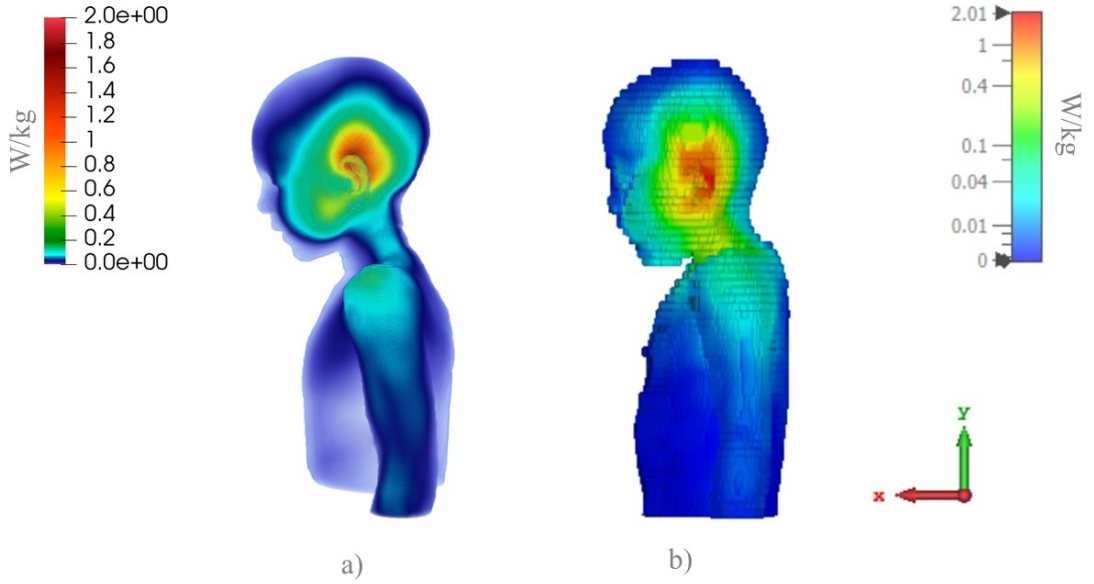

Figure 35: Comparison of 10g SAR simulation results for antenna position (1 mm) by child ear in: a) FDTD code, b) CST Studio Suite.

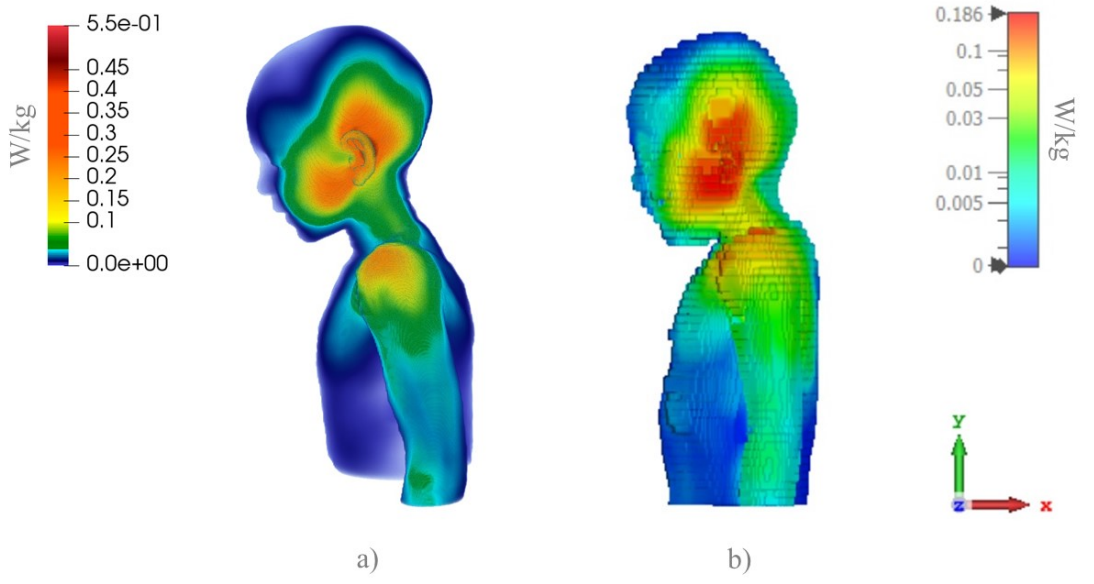

Figure 36: Comparison of 10g SAR simulation results for antenna position (16 mm) by child ear in: a) FDTD code, b) CST Studio Suite.

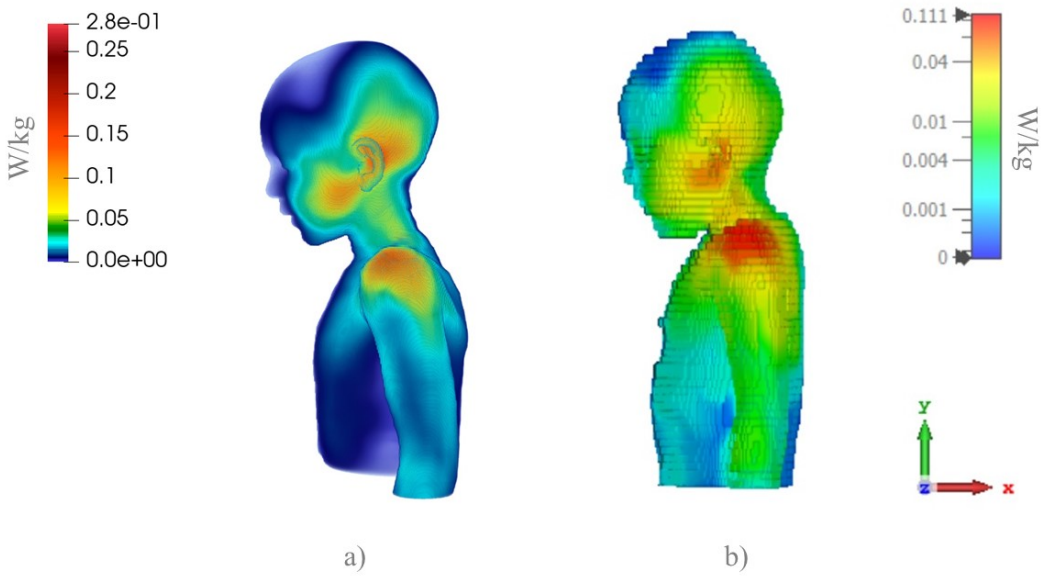

Figure 37: Comparison of 10g SAR simulation results for antenna position (50 mm) by child ear in: a) FDTD code, b) CST Studio Suite.

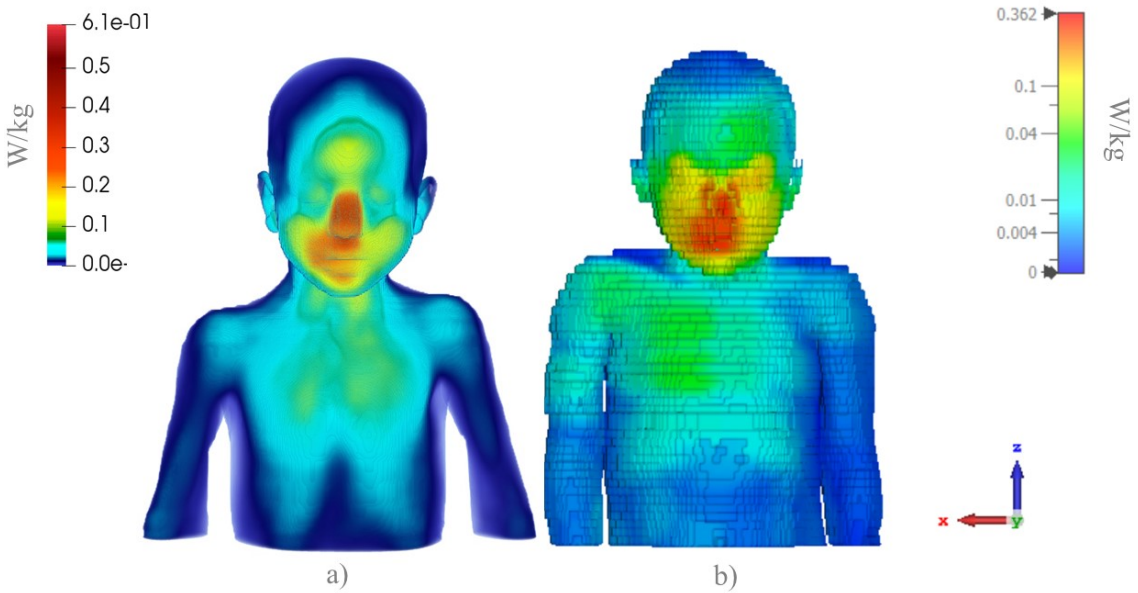

Figure 38: Comparison of 10g SAR simulation results for antenna position (1 mm) by child mouth in: a) FDTD code, b) CST Studio Suite.

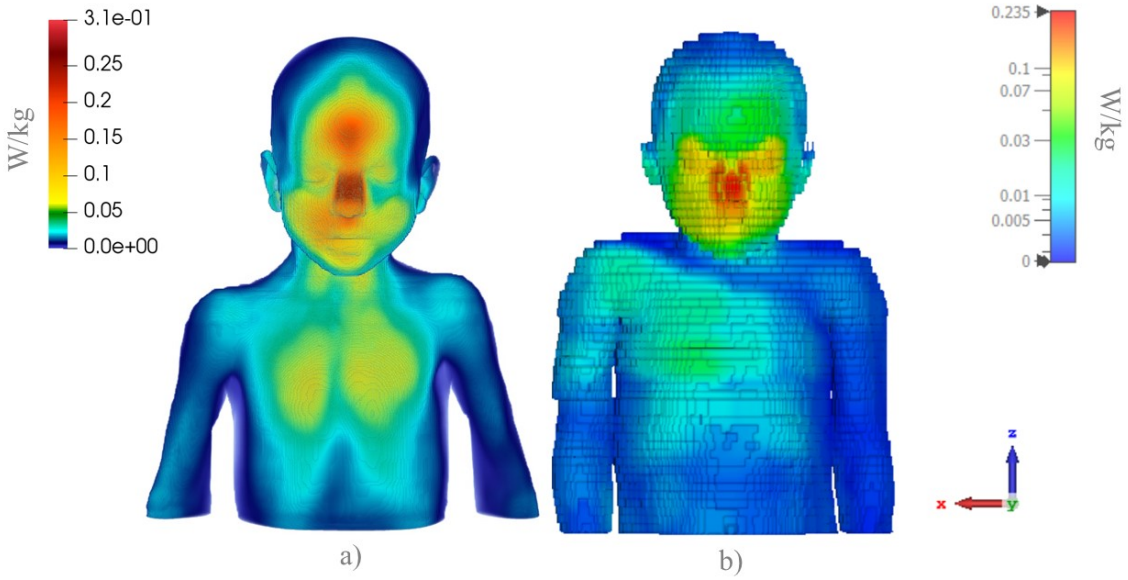

Figure 39: Comparison of 10g SAR simulation results for antenna position (16 mm) by child mouth in: a) FDTD code, b) CST Studio Suite.

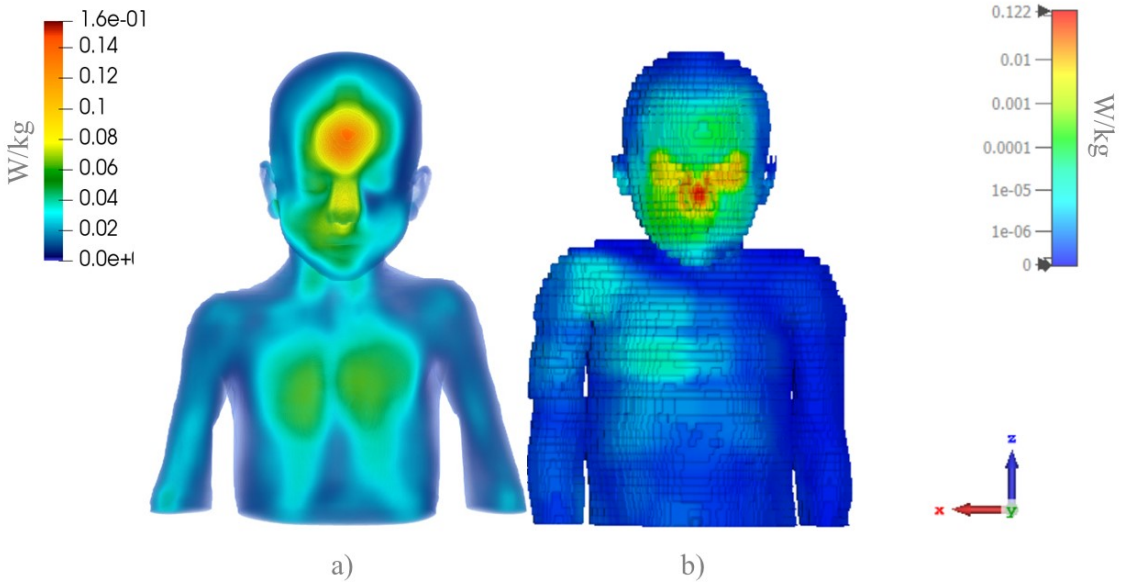

Figure 40: Comparison of 10g SAR simulation results for antenna position (50 mm) by child mouth in: a) FDTD code, b) CST Studio Suite.

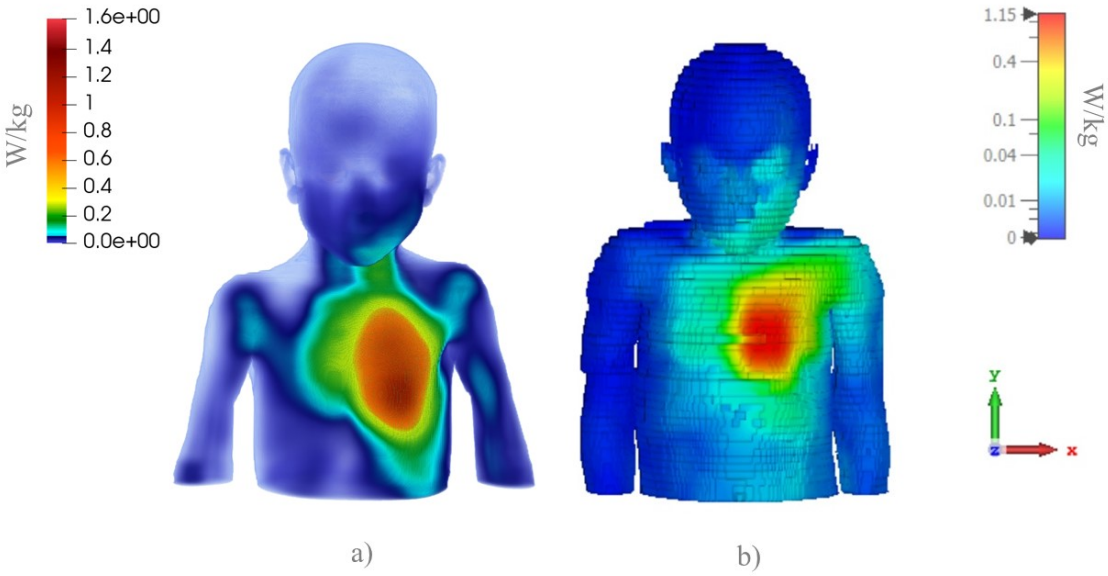

Figure 41: Comparison of 10g SAR simulation results for antenna position (1 mm) by child chest in: a) FDTD code, b) CST Studio Suite.

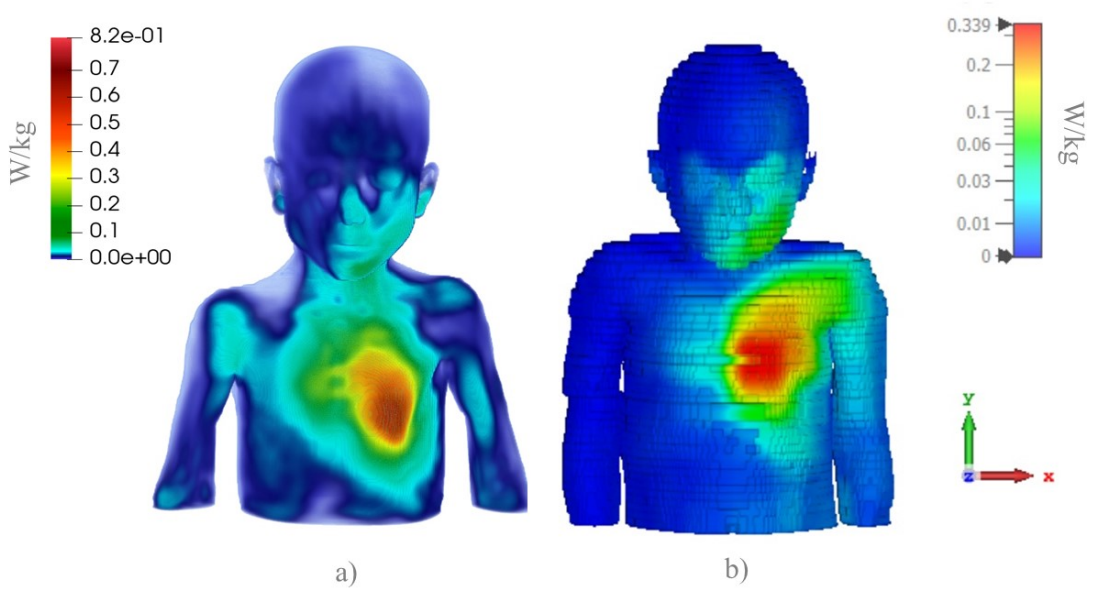

Figure 42: Comparison of 10g SAR simulation results for antenna position (16 mm) by child chest in: a) FDTD code, b) CST Studio Suite.

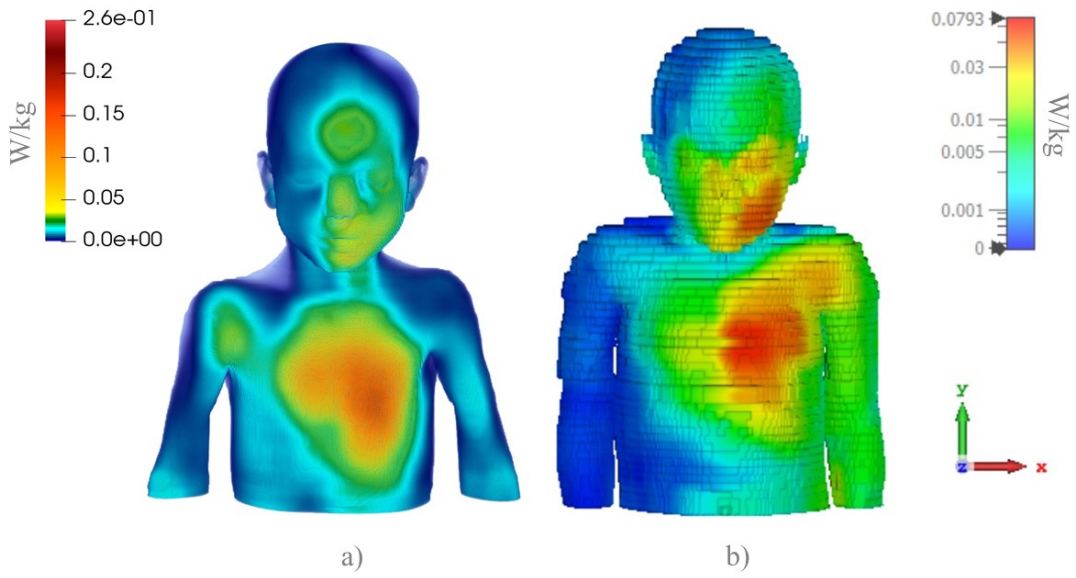

Figure 43: Comparison of 10g SAR simulation results for antenna position (50 mm) by child chest in: a) FDTD code, b) CST Studio Suite.

Below a table and a histogram was presented depicting the maximum SAR (10g) values for both the FDTD and CST cases across all the positions and distances considered.

Location of PIFA	***SAR [W\kg]***					
	1 mm		*16 mm*		*50 mm*	
	FDTD	**CST**	**FDTD**	**CST**	**FDTD**	**CST**
Ear	2.006	1.900	0.549	0.473	0.282	0.173
Mouth	0.609	0.433	0.443	0.326	0.157	0.155
Chest	2.097	1.150	0.819	0.339	0.263	0.080

Table 19: Comparison of the results for child body model in case of SAR 10 g.

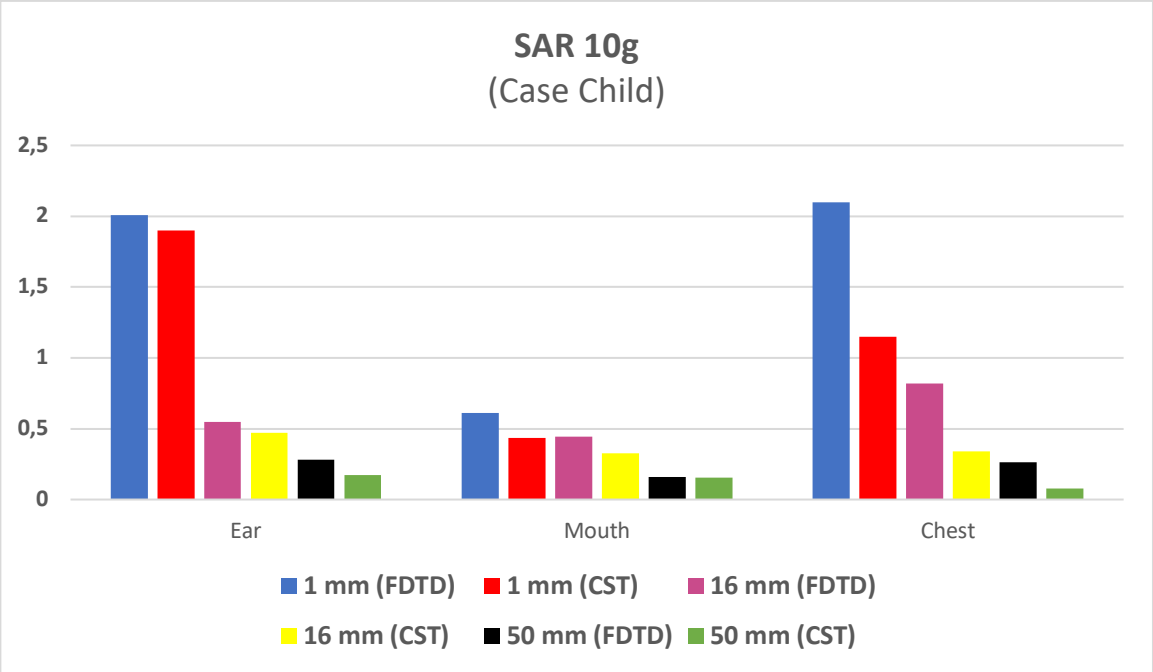

Figure 44: histogram about comparison of the results for the child body model in case of SAR 10 g.

3.2 Women's Cases

The case of woman human models ("Ella" in the FDTD case and "Laura" in the CST Studio case) is analyzed by calculating their SAR averaged over both 1g and 10g of tissue. This is done for scenarios in which the antenna is positioned near the left ear, mouth, and chest, respectively.

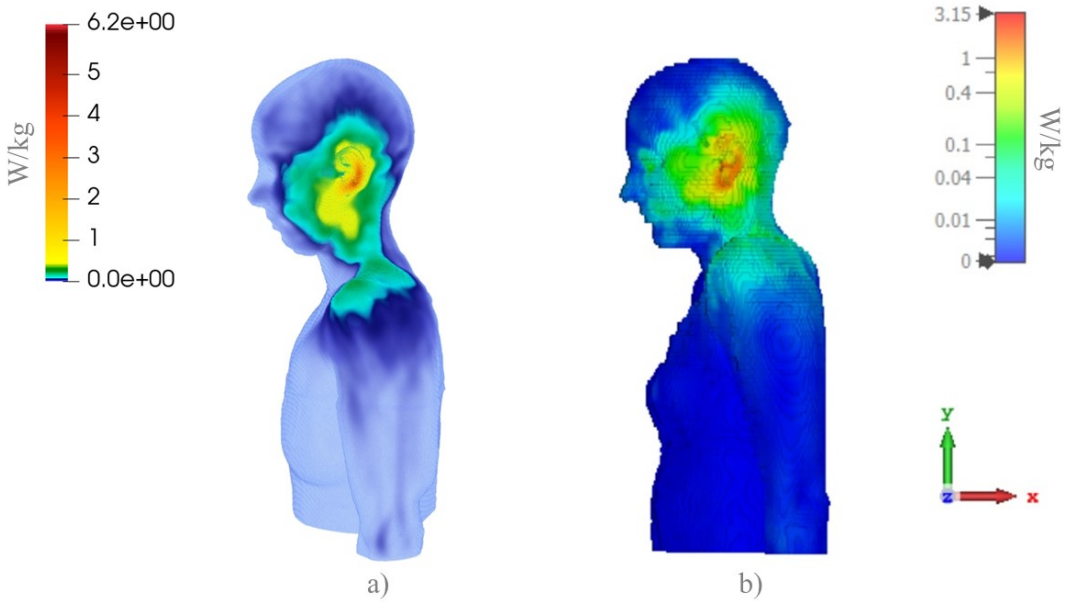

Figure 45: Comparison of 1 g SAR simulation results for antenna position (1 mm) by woman ear in: a) FDTD code, b) CST Studio Suite.

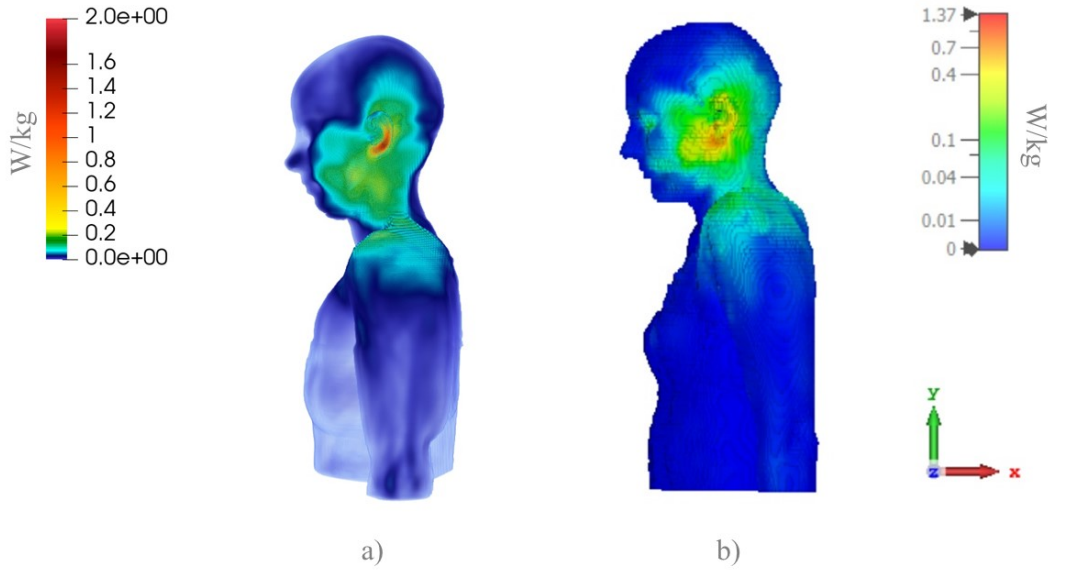

Figure 46: Comparison of 1 g SAR simulation results for antenna position (16 mm) by woman ear in: a) FDTD code, b) CST Studio Suite.

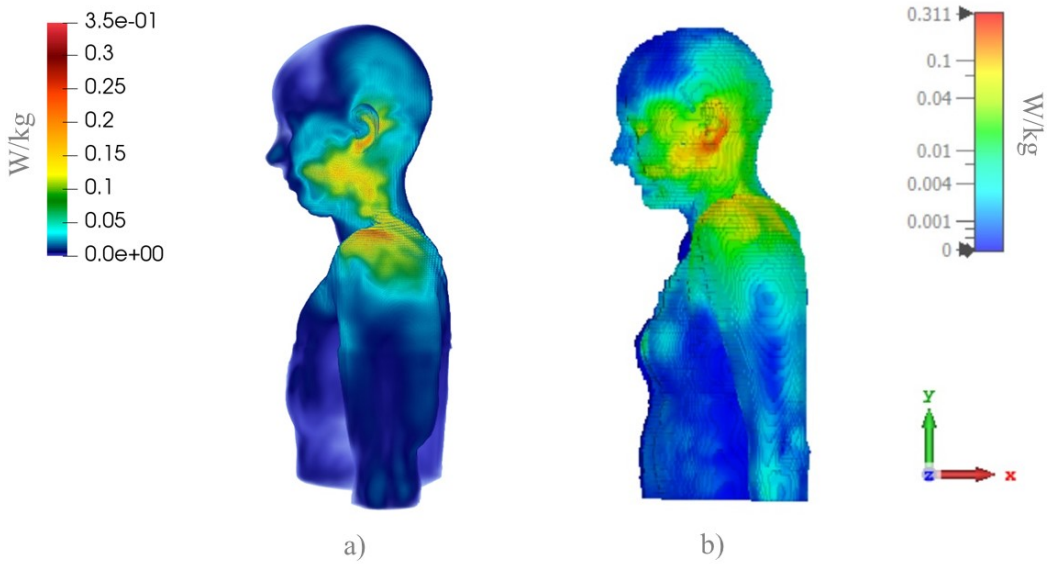

Figure 47: Comparison of 1 g SAR simulation results for antenna position (50 mm) by woman ear in: a) FDTD code, b) CST Studio Suite.

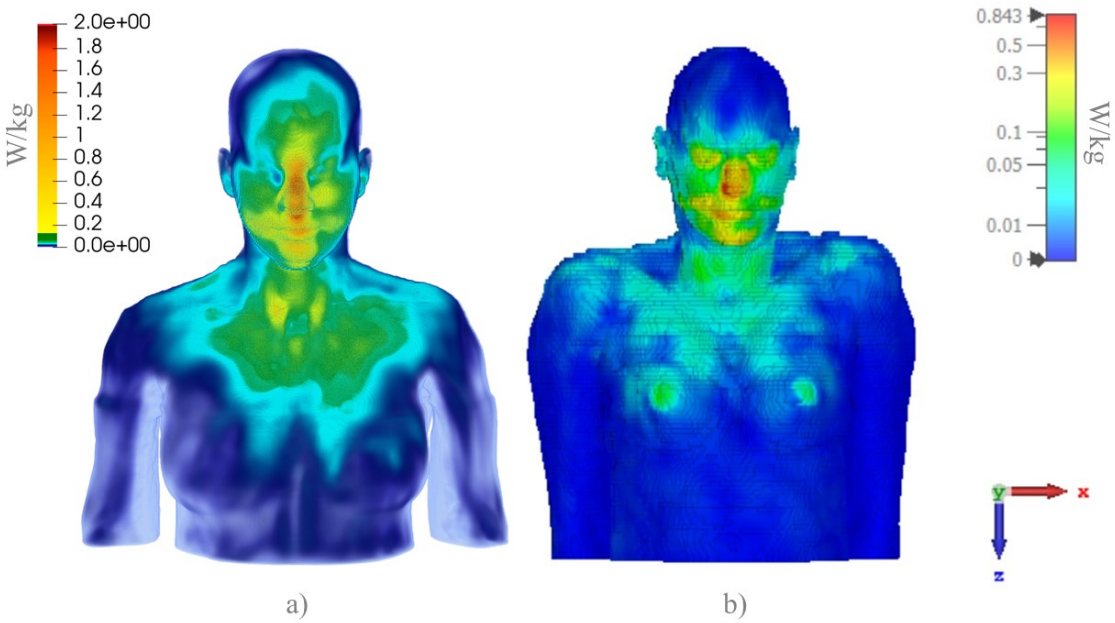

Figure 48: Comparison of 1 g SAR simulation results for antenna position (1 mm) by woman mouth in: a) FDTD code, b) CST Studio Suite.

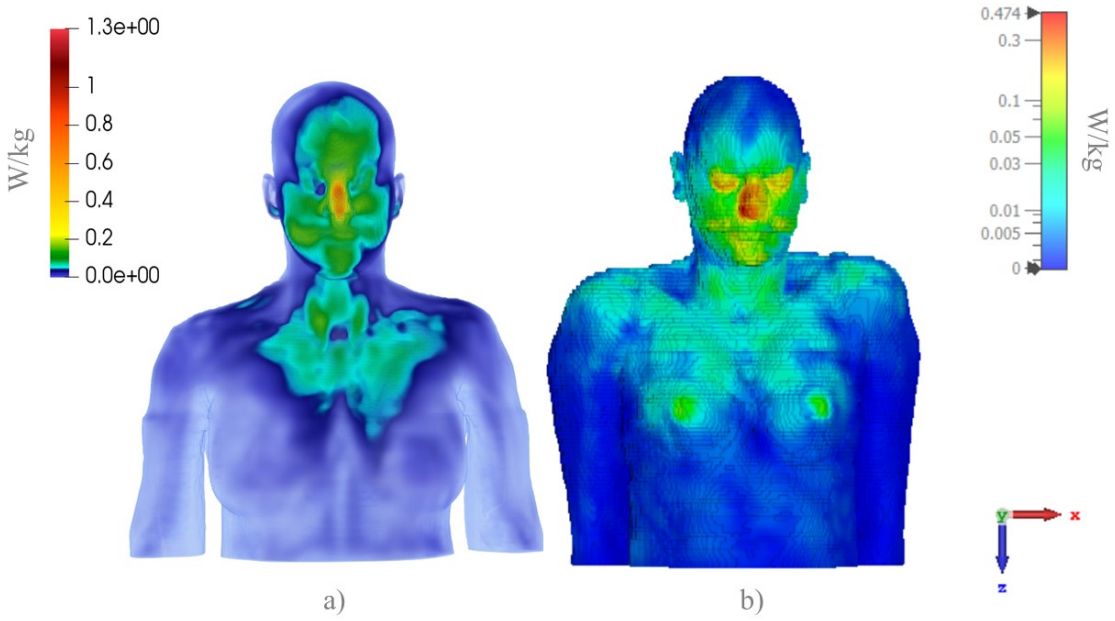

Figure 49: Comparison of 1 g SAR simulation results for antenna position (16 mm) by woman mouth in: a) FDTD code, b) CST Studio Suite.

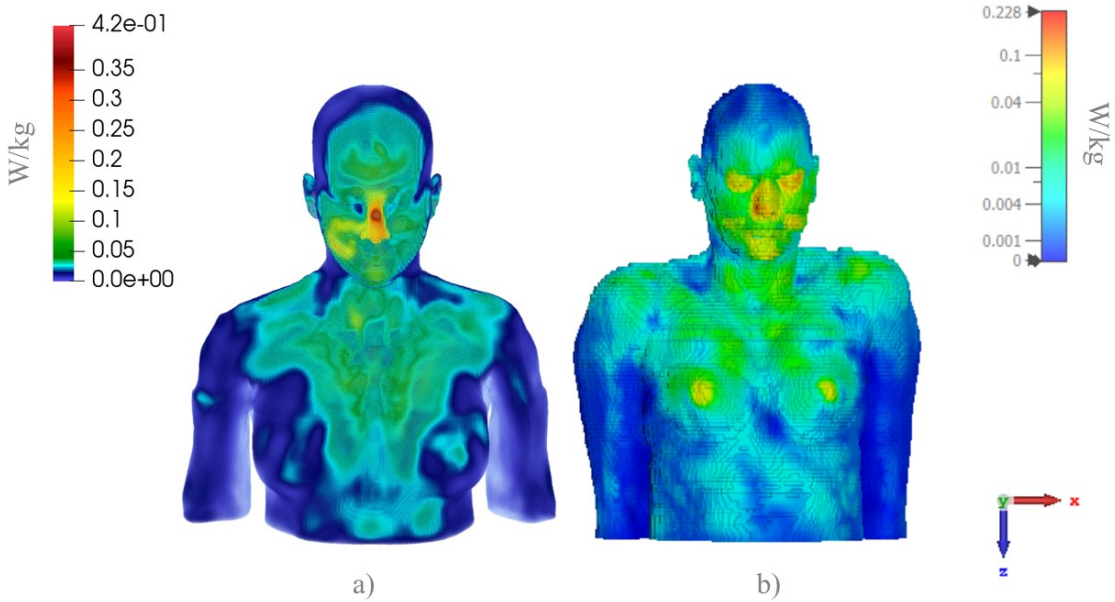

Figure 50: Comparison of 1 g SAR simulation results for antenna position (50 mm) by woman mouth in: a) FDTD code, b) CST Studio Suite.

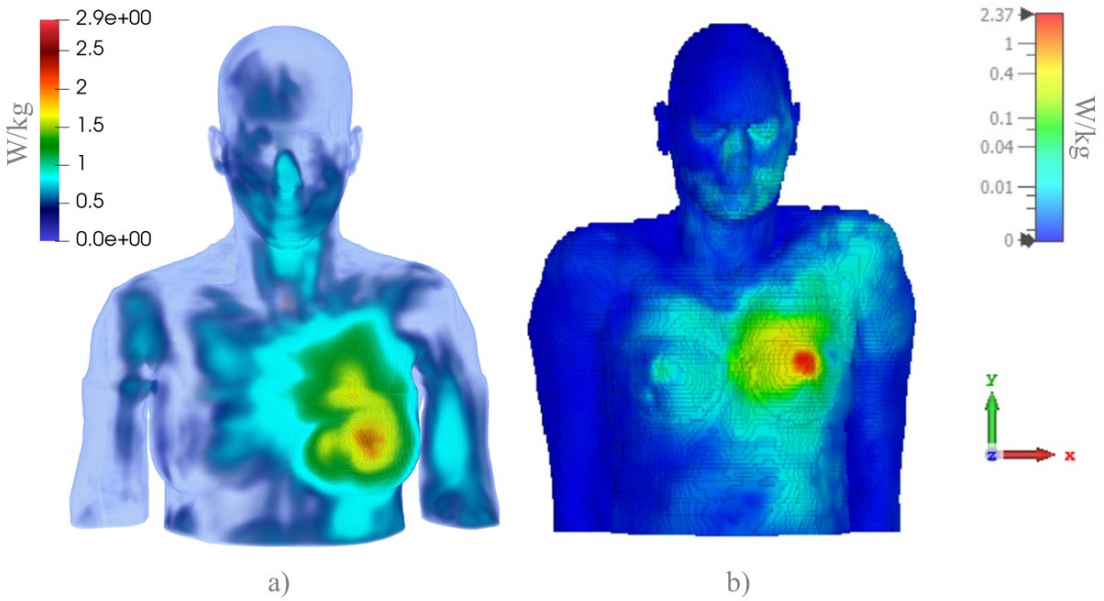

Figure 51: Comparison of 1 g SAR simulation results for antenna position (1 mm) by woman chest in: a) FDTD code, b) CST Studio Suite.

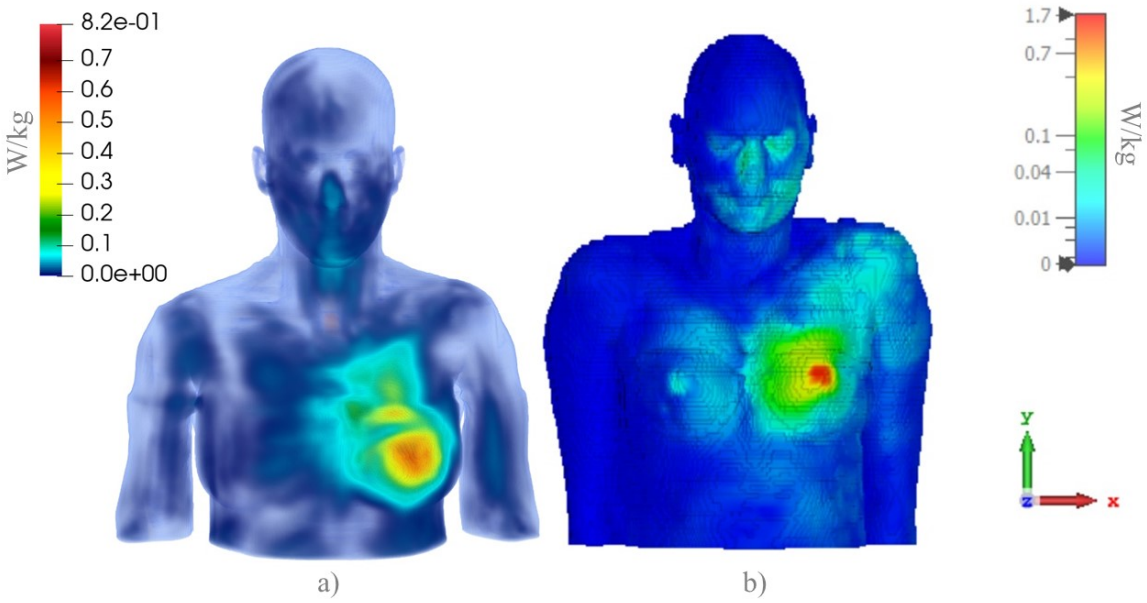

Figure 52: Comparison of 1 g SAR simulation results for antenna position (16 mm) by woman chest in: a) FDTD code, b) CST Studio Suite.

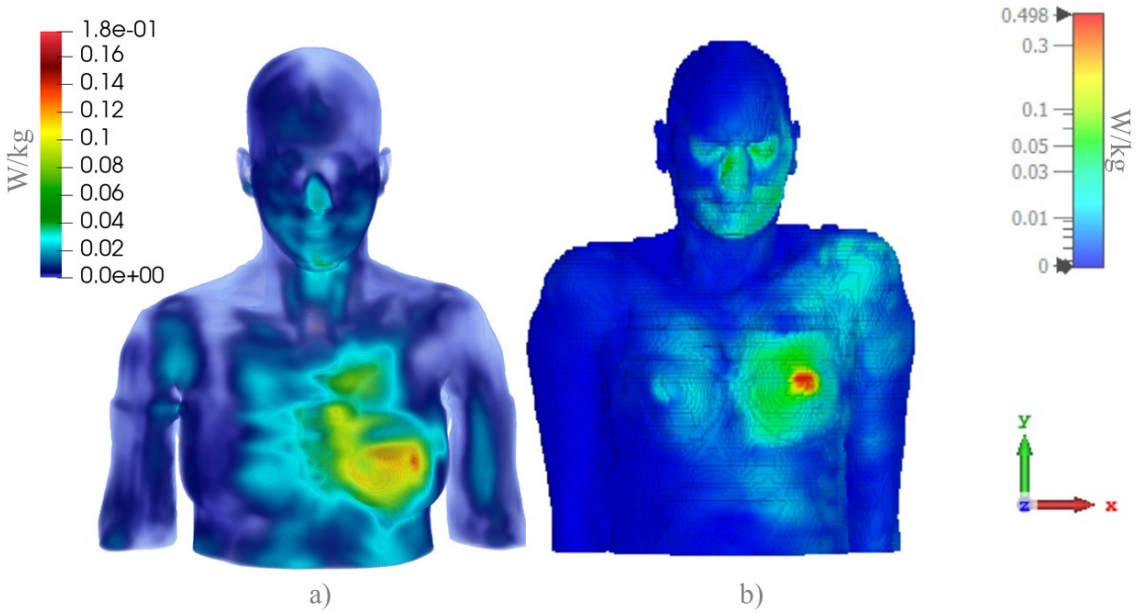

Figure 53: Comparison of 1 g SAR simulation results for antenna position (50 mm) by woman chest in: a) FDTD code, b) CST Studio Suite.

Following a table and a histogram was presented depicting the maximum SAR (1g) values for both the FDTD and CST cases across all the positions and distances considered for "Ella" and "Laura" biological models.

Location of PIFA	***SAR [W\kg]***					
	1 mm		*16 mm*		*50 mm*	
	FDTD	**CST**	**FDTD**	**CST**	**FDTD**	**CST**
Ear	5.216	3.278	1.971	1.431	0.348	0.322
Mouth	2.202	0.833	1.308	0.483	0.423	0.231
Chest	2.998	2.389	0.817	1.716	0.178	0.508

Table 20: Comparison of the results for the woman body model in case of SAR 1 g.

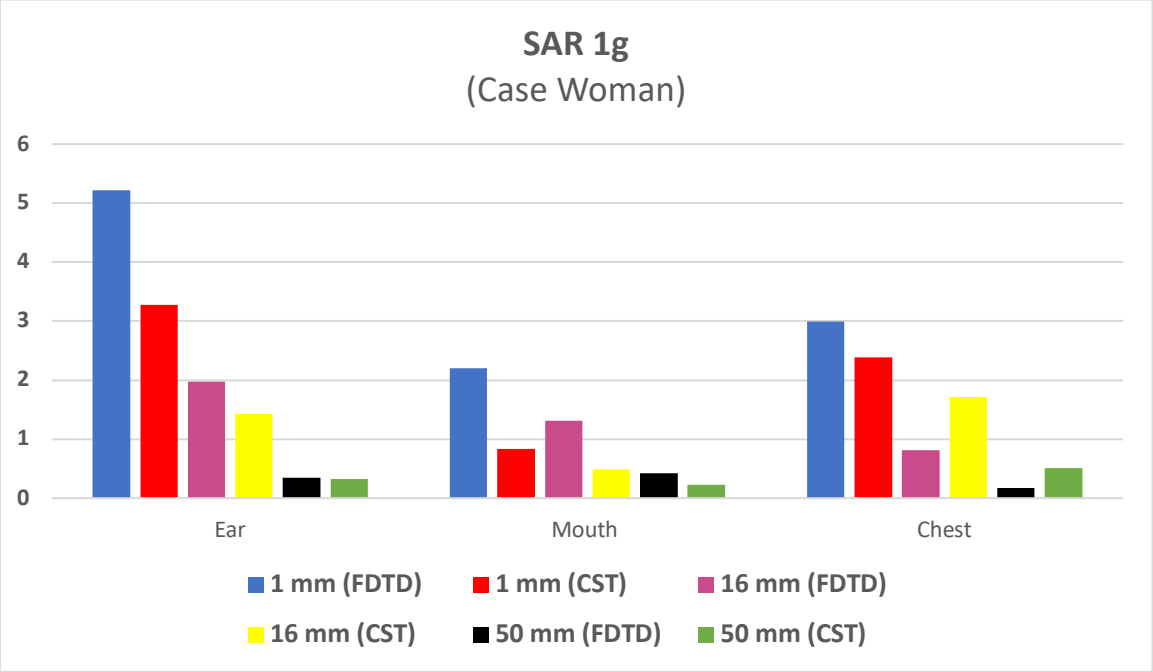

Figure 54: Histogram about comparison of the results for the woman body model in case of SAR 1 g.

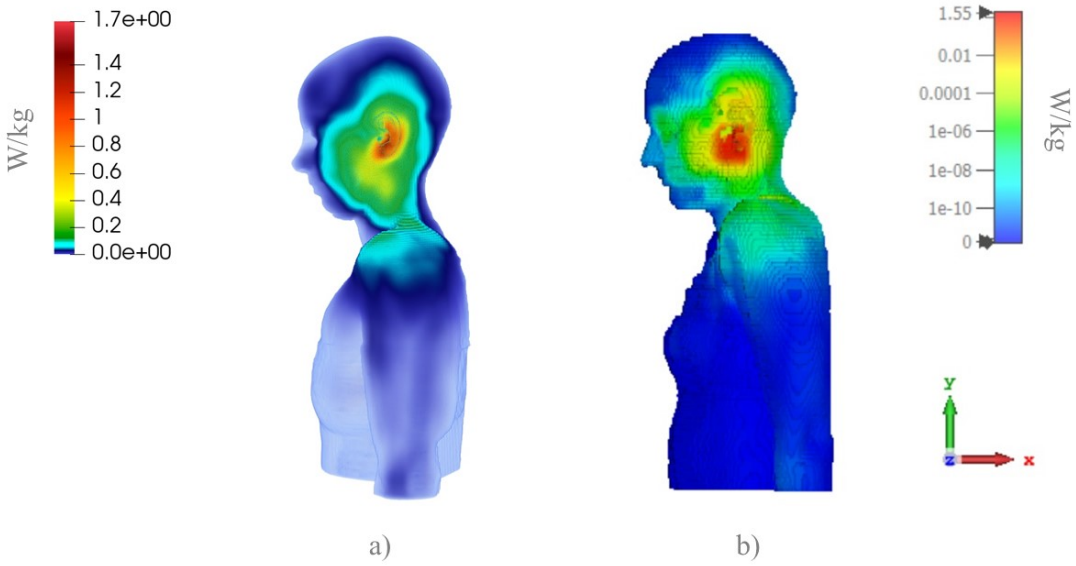

Figure 55: Comparison of 10 g SAR simulation results for antenna position (1 mm) by woman ear in: a) FDTD code, b) CST Studio Suite.

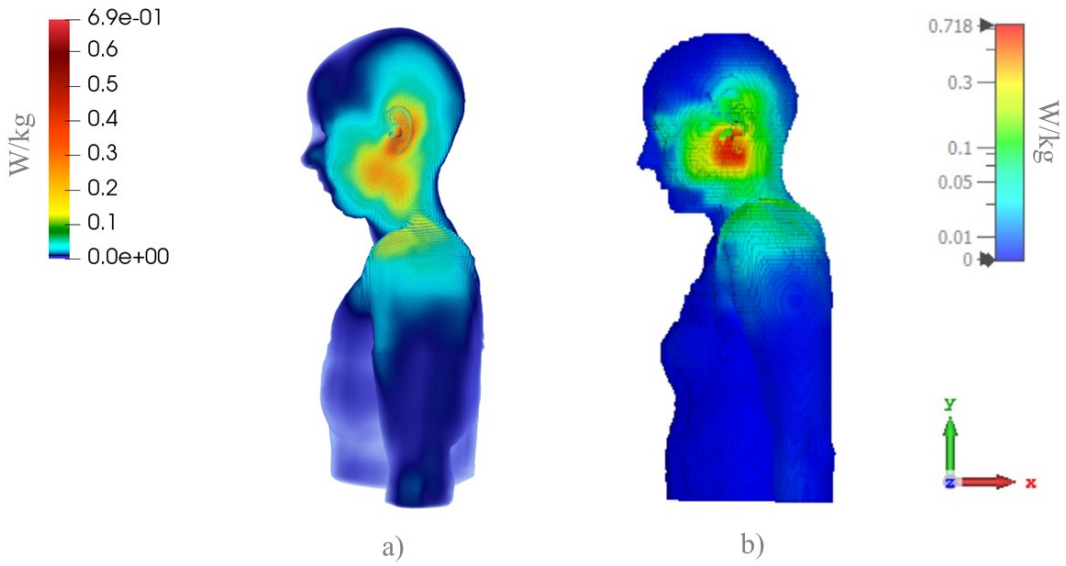

Figure 56: Comparison of 10 g SAR simulation results for antenna position (16 mm) by woman ear in: a) FDTD code, b) CST Studio Suite.

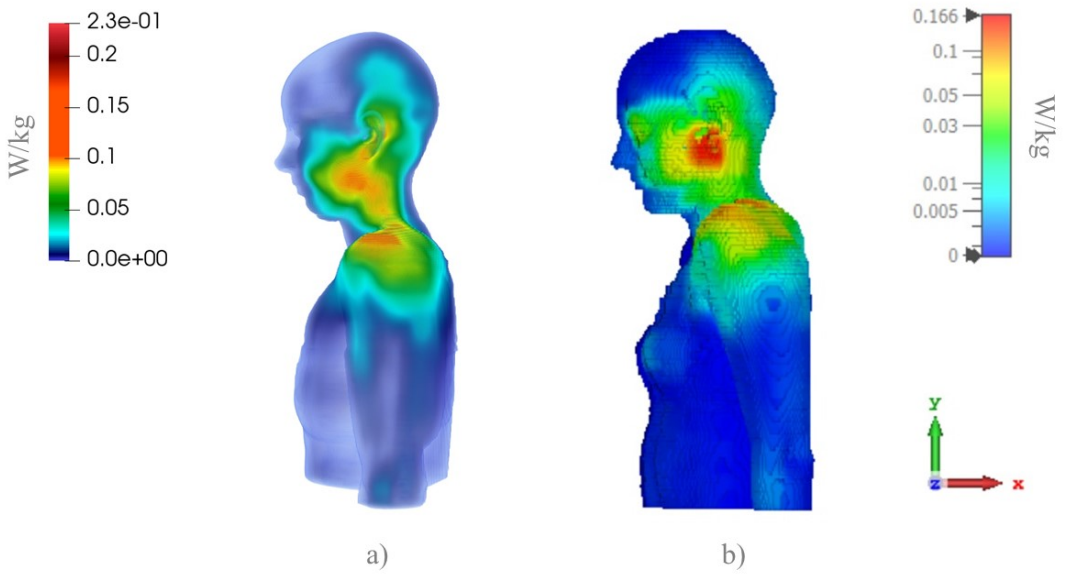

Figure 57: Comparison of 10 g SAR simulation results for antenna position (50 mm) by woman ear in: a) FDTD code, b) CST Studio Suite.

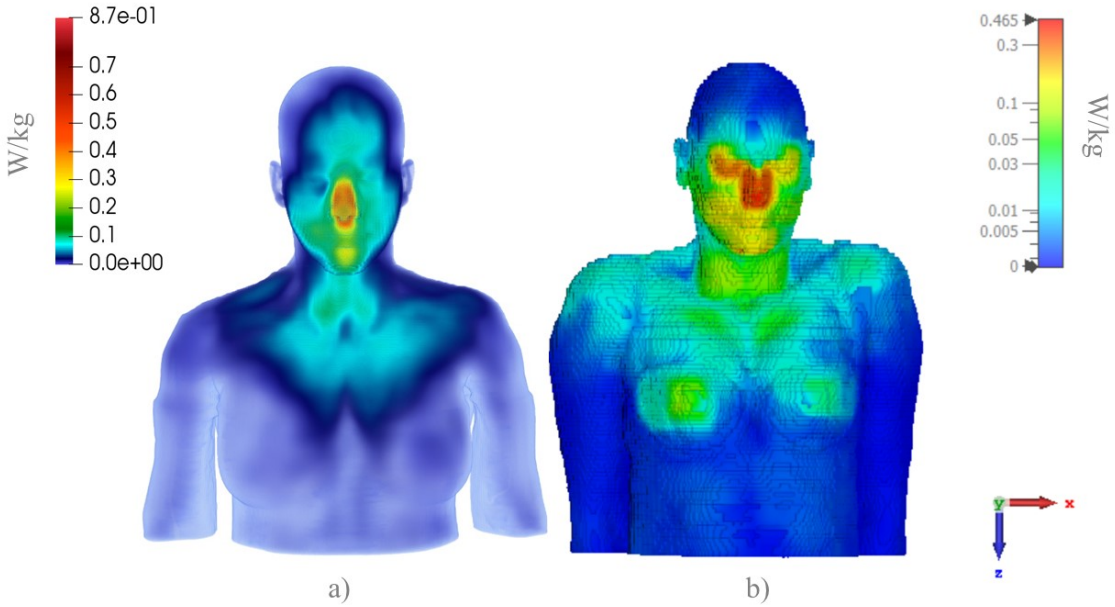

Figure 58: Comparison of 10 g SAR simulation results for antenna position (1 mm) by woman mouth in: a) FDTD code, b) CST Studio Suite.

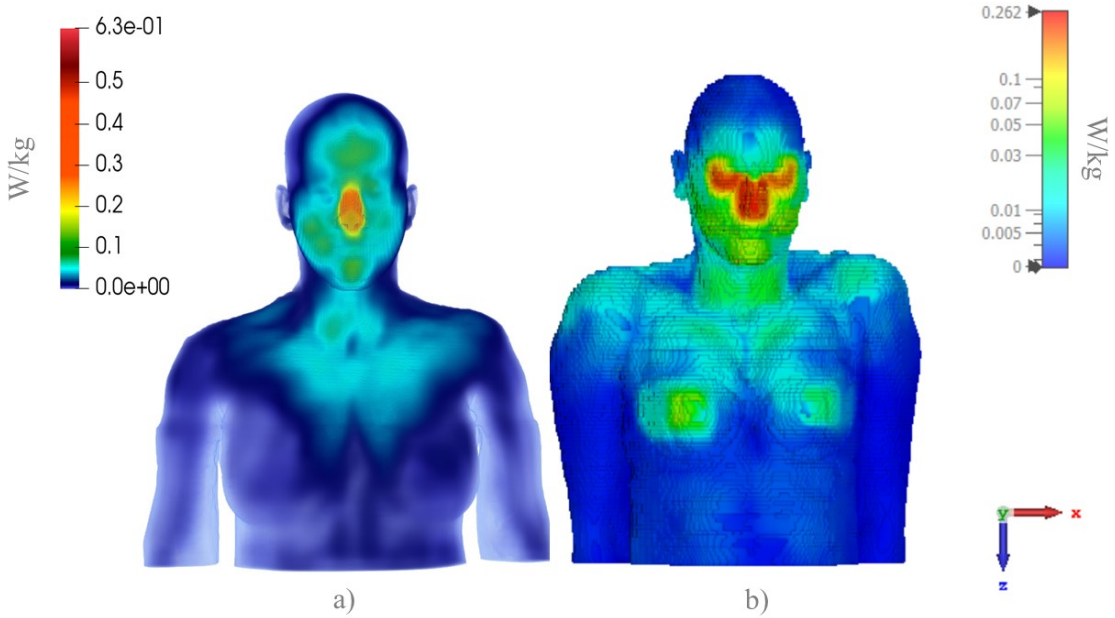

Figure 59: Comparison of 10 g SAR simulation results for antenna position (16 mm) by woman mouth in: a) FDTD code, b) CST Studio Suite.

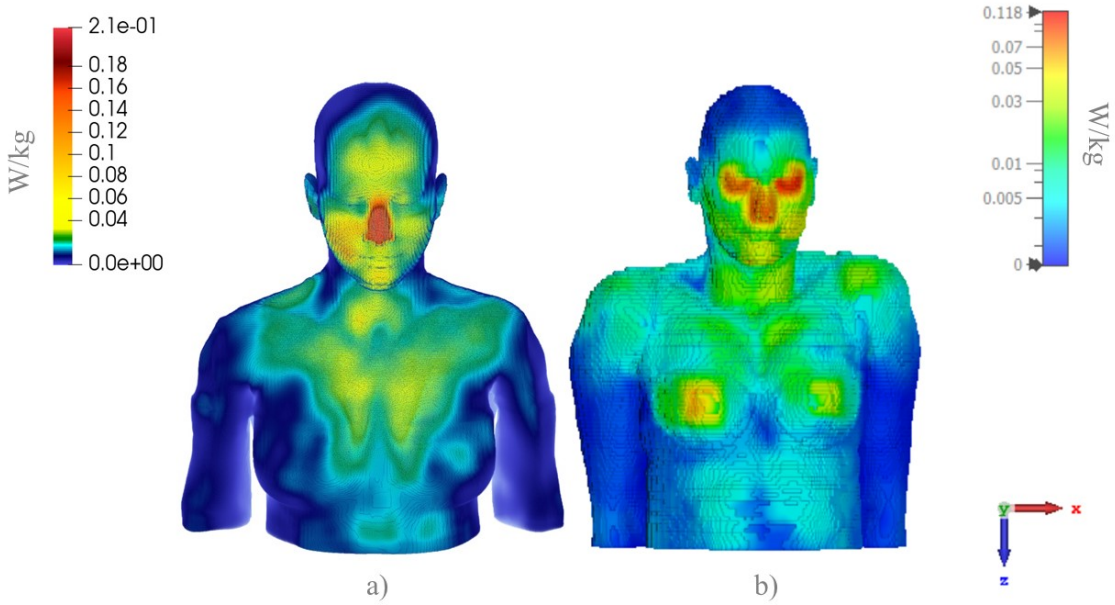

Figure 60: Comparison of 10 g SAR simulation results for antenna position (50 mm) by woman mouth in: a) FDTD code, b) CST Studio Suite.

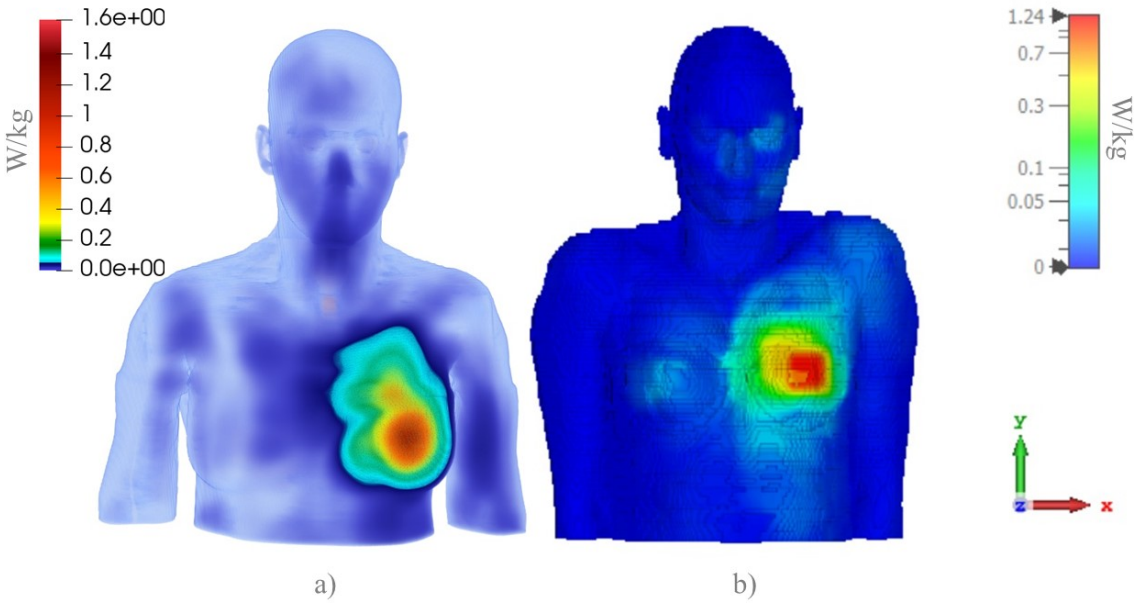

Figure 61: Comparison of 10 g SAR simulation results for antenna position (1 mm) by woman chest in: a) FDTD code, b) CST Studio Suite.

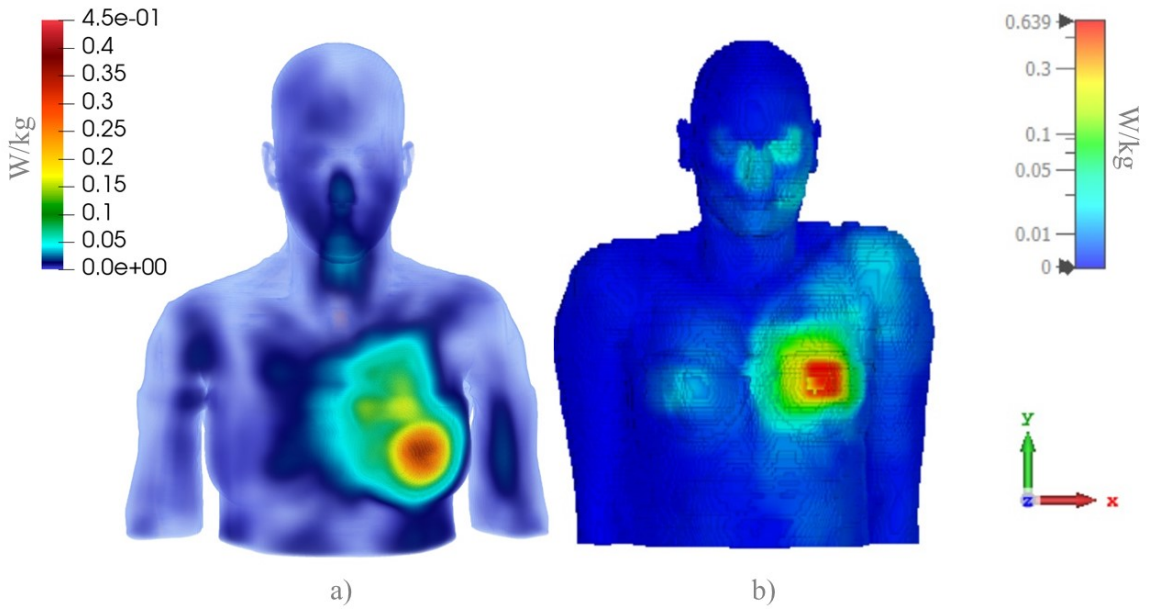

Figure 62: Comparison of 10 g SAR simulation results for antenna position (16 mm) by woman chest in: a) FDTD code, b) CST Studio Suite.

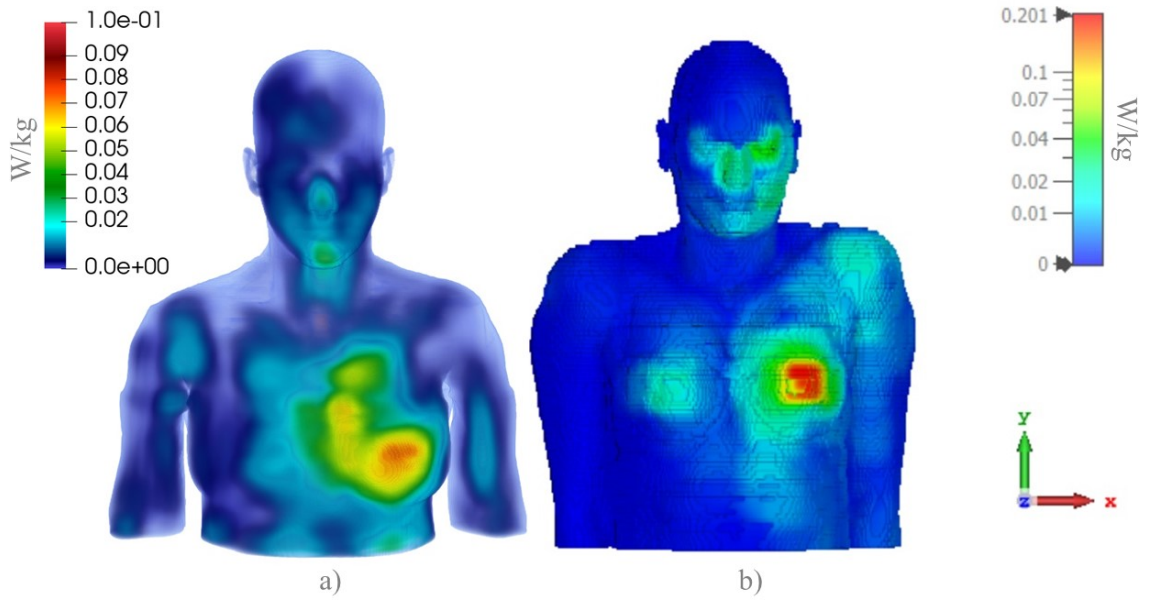

Figure 63: Comparison of 10 g SAR simulation results for antenna position (50 mm) by woman chest in: a) FDTD code, b) CST Studio Suite.

Afterwards Table and histogram of the maximum SAR (10g) values for "Ella" (FDTD) and "Laura" (CST Studio).

Location of PIFA	*SAR [W\kg]*					
	1 mm		*16 mm*		*50 mm*	
	FDTD	**CST**	**FDTD**	**CST**	**FDTD**	**CST**
Ear	1.718	1.545	0.691	0.718	0.232	0.169
Mouth	0.873	0.447	0.632	0.264	0.215	0.119
Chest	1.615	1.238	0.450	0.639	0.104	0.201

Table 21: Comparison of the results for the woman body model in case of SAR 10 g.

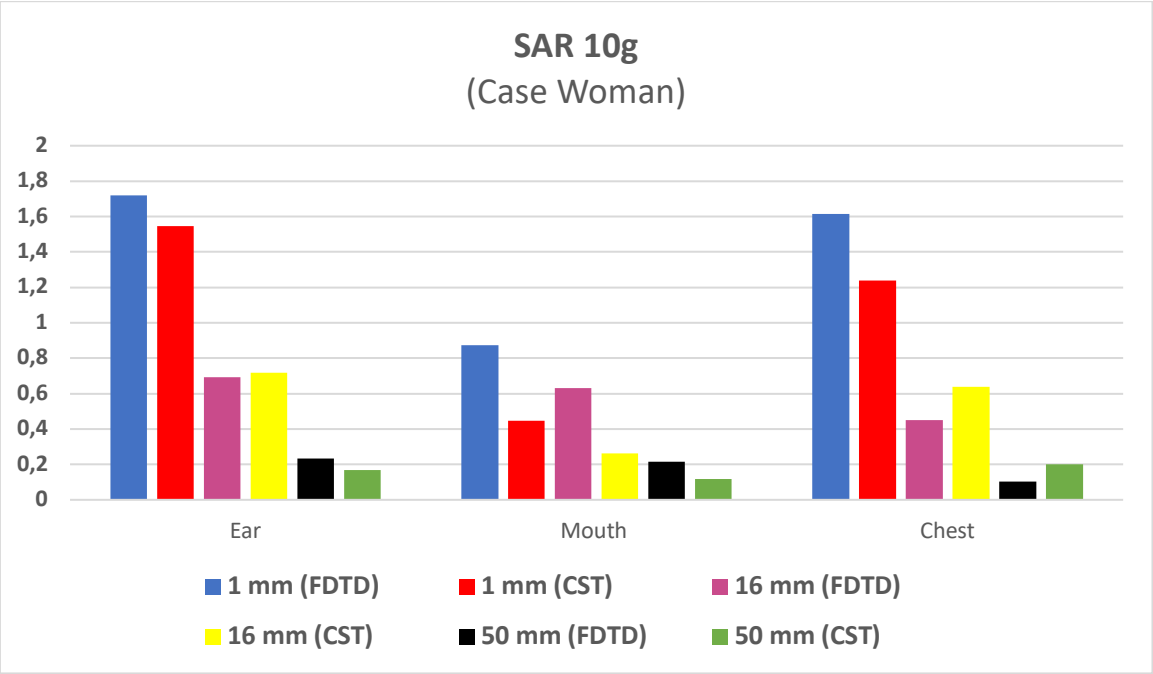

Figure 64: Histogram about comparison of the results for woman body model in case of SAR 10 g.

3.3 Analysis of Absorbed Powers

It is important to remember that it's possible to calculate the power absorbed in the tissues starting from the SAR; therefore, it is necessary to consider the power absorbed by the tissues in the three positions studied.

But this was only possible through the FDTD algorithm by analysing and calculating the field within each cell in the biological model. Starting from the SAR equation (see Eq. 54), it is possible to define the power absorbed in a tissue cell by considering its volume (in this case 1x1x1 mm, respectively 1mm in length, 1mm in width and 1mm in height):

$$Cell_{pot} = \frac{\sigma|E^2|}{2} * V$$

Equation 59

The percentages of power absorbed are analyzed for all tissues considering the power dissipated (in term of average) within the cells given by:

$$Pot_{tot} = \sum_{1}^{n\_cell} \frac{\sigma|E^2|}{2} * grid_{volume}$$

Equation 60

Important to consider that this algorithm analyzes not the actual field values but only the peak or maximum values.

In the following table are present the values of maximum power absorbed in the various analyzed cases.

		Absorption of Electric Field [W]		
		1 mm	*16 mm*	*50 mm*
Ear	***Thelonious***	0.282246	0.198496	0.110455
	Ella	0.307875	0.227049	0.152685
Mouth	***Thelonious***	0.221051	0.190349	0.1271
	Ella	0.233189	0.191957	0.12976
Chest	***Thelonious***	0.271825	0.174733	0.108489
	Ella	0.250772	0.147502	0.090364

Table 22: Values of maximum power absorbed by Thelonious and Ella in different positions and at different distances.

Below are tables and histograms of the tissues that absorbed the most power, which are different in each case due to the positioning of the PIFA antenna and the different biological model considered.

In the first case (ear) for the biological model of "Thelonious" the tissues analyzed are tissues such as muscle, brain (gray matter), connective tissue, skin, cerebellum, cerebrospinal fluid, skull.

Considering the biological model of the woman, on the other hand, the muscles, skin, skull, but also SAT (Subcutaneous Fat), blood and bone were mainly considered.

In the second case (mouth), in the scenarios of both 'Thelonious' and 'Ella', the same tissues were analyzed, including tongue and tooth.

In the last case, i.e., the scenario of PIFA placement near chest, tissues such as heart muscle, lung, thymus were also analyzed, specificity in case of “Ella” was also breast fat.

Thelonious - ear	1 mm	16mm	50mm
Bone	0,29%	0,33%	0,20%
Bone Marrow	0,36%	0,19%	0,08%
Brain (Gray Matter)	4,34%	1,82%	0,77%
Brain (White Matter)	1,17%	0,51%	0,22%
Cartilage	1,43%	0,66%	0,23%
Cerebellum	1,91%	0,91%	0,43%
Cerebrospinal Fluid	1,74%	0,81%	0,35%
Connective Tissue	2,55%	1,54%	0,71%
Fat	0,44%	0,41%	0,20%
Muscle	7,33%	7,49%	4,72%
SAT (Subcutaneous Fat)	0,66%	0,53%	0,31%
Skin	3,55%	2,88%	1,71%
Skull	1,02%	0,49%	0,20%

Table 23: Percentage of absorbed power by selected tissues (case Thelonious ear).

Ella – ear	1 mm	16mm	50mm
Blood	0,32%	0,17%	0,07%
Bone	0,25%	0,31%	0,26%
Brain (Gray Matter)	1,07%	0,71%	0,38%
Brain (White Matter)	0,37%	0,25%	0,14%
Cartilage	1,01%	0,36%	0,10%
Cerebellum	0,60%	0,33%	0,16%
Cerebrospinal Fluid	0,57%	0,39%	0,21%
Connective Tissue	0,95%	0,83%	0,52%
Fat	0,53%	0,51%	0,41%
Muscle	11,83%	9,99%	7,20%
SAT (Subcutaneous Fat)	1,25%	1,09%	0,87%
Skin	2,77%	5,55%	4,03%
Skull	1,06%	0,56%	0,25%

Table 24: Percentage of absorbed power by selected tissues (case Ella ear).

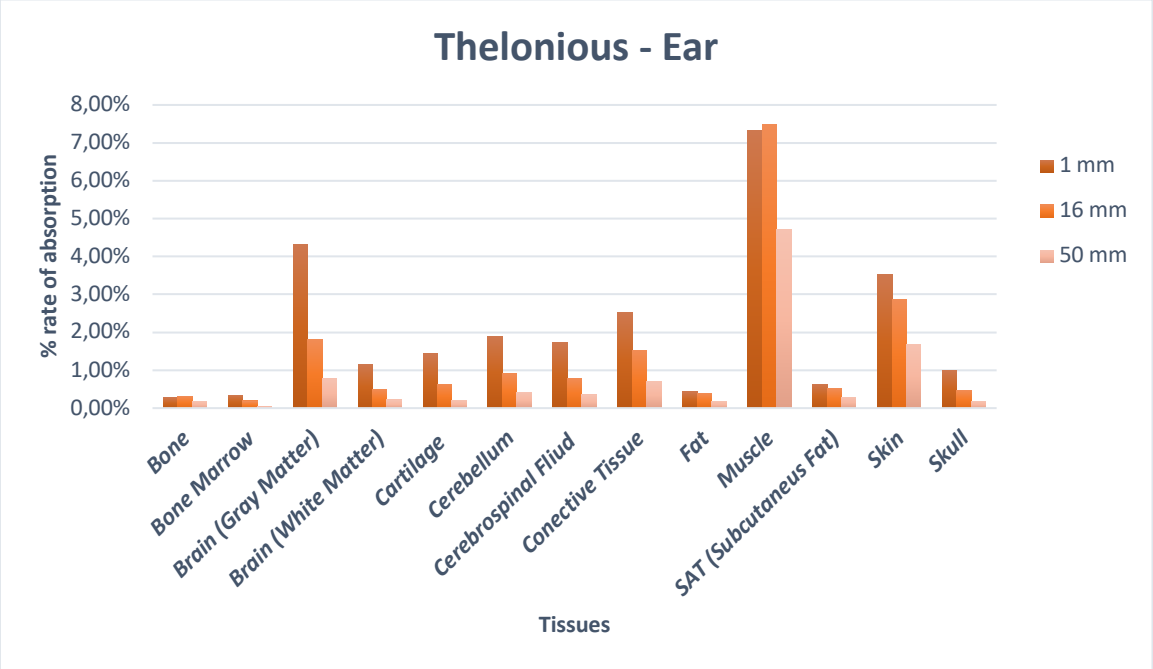

Figure 65: Histogram about Percentage of absorbed power by selected tissues (case Thelonious ear).

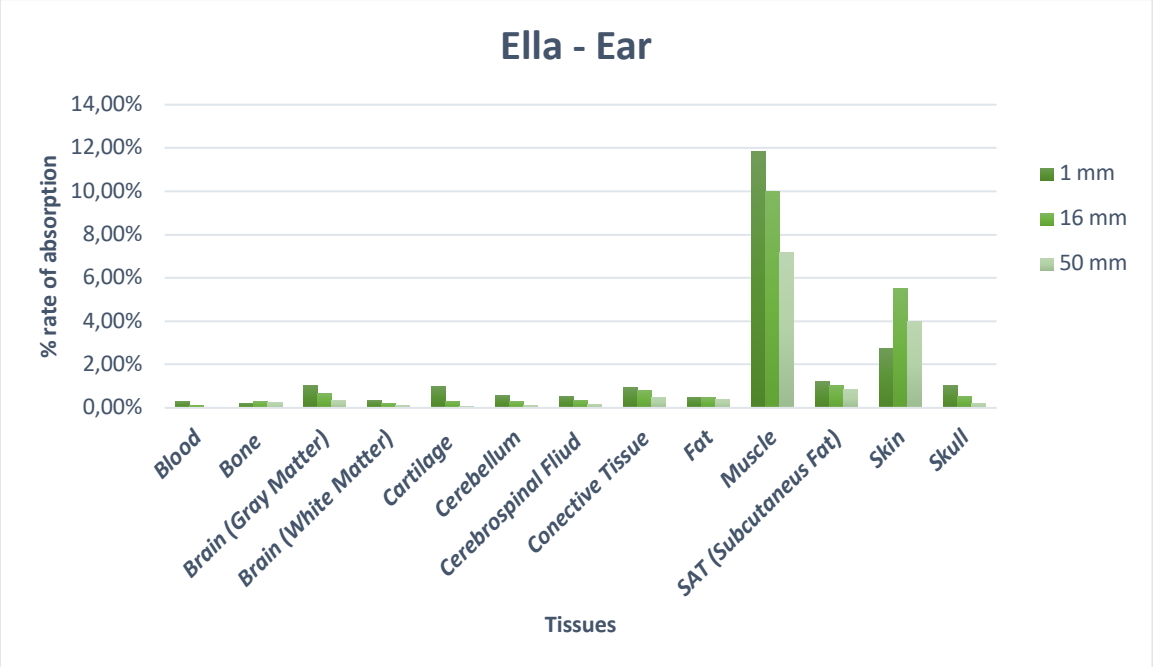

Figure 66: Histogram about Percentage of absorbed power by selected tissues (case Ella ear).

Thelonious - mouth	1 mm	16mm	50mm
Bone Marrow	0,24%	0,18%	0,09%
Brain (Gray Matter)	1,22%	1,44%	1,09%
Brain (White Matter)	0,41%	0,49%	0,37%
Cartilage	1,04%	0,80%	0,36%
Cerebrospinal Fluid	0,68%	0,83%	0,63%
Connective Tissue	1,78%	1,42%	0,76%
Fat	0,63%	0,47%	0,24%
Muscle	6,79%	5,49%	3,86%
SAT (Subcutaneous Fat)	0,66%	0,58%	0,41%
Skin	3,21%	2,76%	1,90%
Skull	0,85%	0,72%	0,35%
Tongue	0,69%	0,42%	0,18%
Tooth	0,08%	0,05%	0,02%

Table 25: Percentage of absorbed power by selected tissues (case Thelonious mouth).

Ella - mouth	1 mm	16mm	50mm
Brain (Gray Matter)	0,57%	0,62%	0,42%
Brain (White Matter)	0,20%	0,22%	0,15%
Cartilage	1,73%	1,28%	0,48%
Cerebrospinal Fluid	0,67%	0,75%	0,47%
Connective Tissue	1,75%	1,32%	0,75%
Fat	0,62%	0,51%	0,36%
Muscle	7,61%	5,87%	4,19%
SAT (Subcutaneous Fat)	1,21%	1,12%	0,91%
Skin	5,25%	4,40%	3,09%
Skull	0,74%	0,70%	0,40%
Tongue	0,37%	0,22%	0,12%
Tooth	0,06%	0,03%	0,02%

Table 26: Percentage of absorbed power by selected tissues (case Ella mouth).

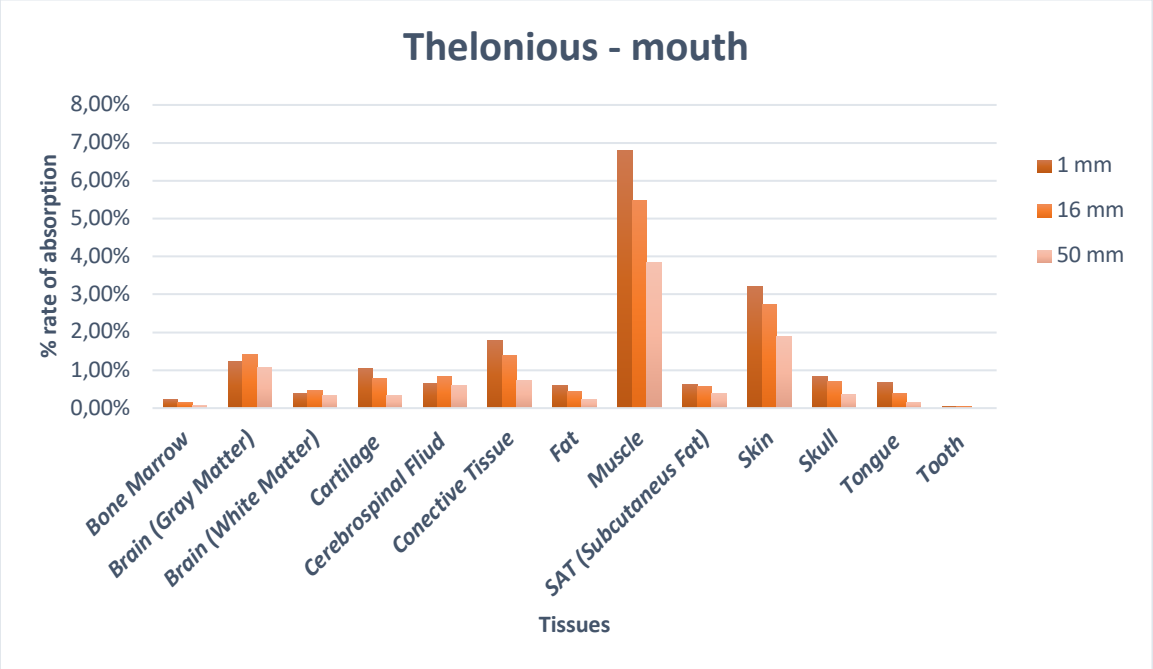

Figure 67: Histogram about Percentage of absorbed power by selected tissues (case Thelonious mouth).

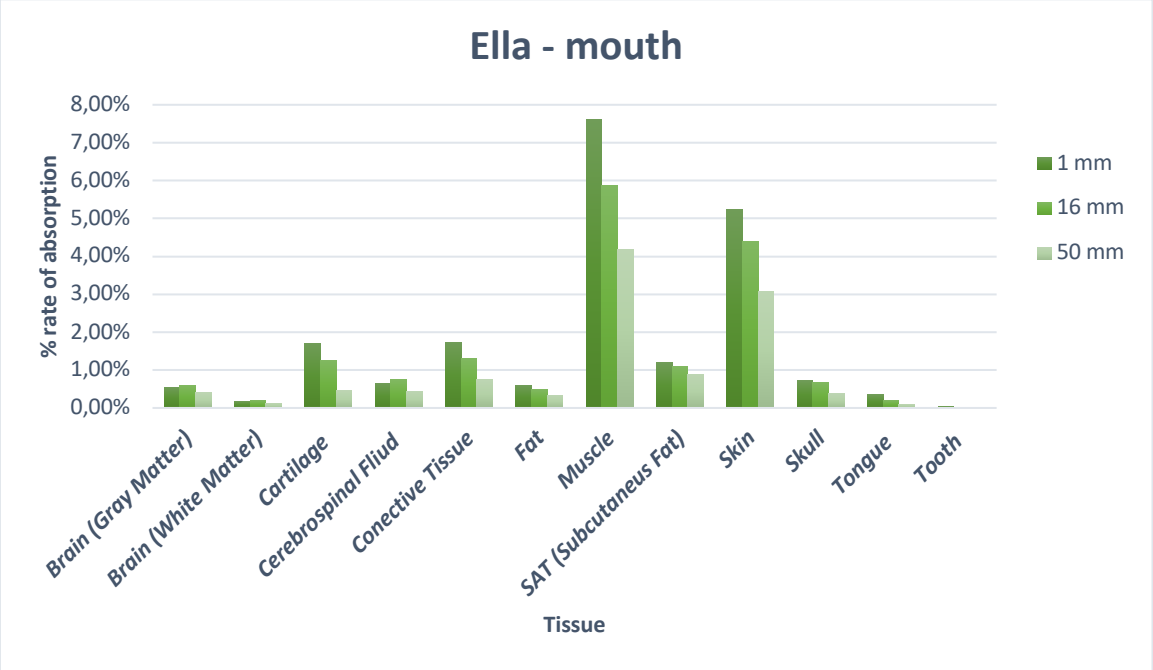

Figure 68: Histogram about Percentage of absorbed power by selected tissues (case Ella mouth).

Thelonious – chest	1 mm	16mm	50mm
Bone	0,30%	0,21%	0,13%
Cartilage	0,83%	0,58%	0,44%
Connective Tissue	0,25%	0,34%	0,37%
Fat	0,23%	0,20%	0,16%
Heart Muscle	5,00%	2,59%	1,05%
Lung	2,49%	1,44%	0,65%
Muscle	9,73%	6,22%	3,68%
SAT (Subcutaneous Fat)	1,14%	0,67%	0,39%
Skin	4,59%	2,86%	1,69%
Thymus	0,58%	0,36%	0,15%

Table 27: Percentage of absorbed power by selected tissues (case Thelonious chest).

Ella – chest	0 mm	16mm	50mm
Bone	0,11%	0,10%	0,07%
Brest Fat	3,81%	1,73%	0,62%
Cartilage	0,16%	0,16%	0,13%
Connective Tissue	0,32%	0,32%	0,20%
Fat	0,42%	0,33%	0,27%
Heart Muscle	0,51%	0,32%	0,17%
Lung	1,46%	0,81%	0,37%
Muscle	4,82%	3,76%	2,83%
SAT (Subcutaneus Fat)	3,58%	1,84%	0,94%
Skin	8,81%	4,37%	2,39%
Thymus	0,03%	0,04%	0,02%

Table 28: Percentage of absorbed power by selected tissues (case Ella mouth).

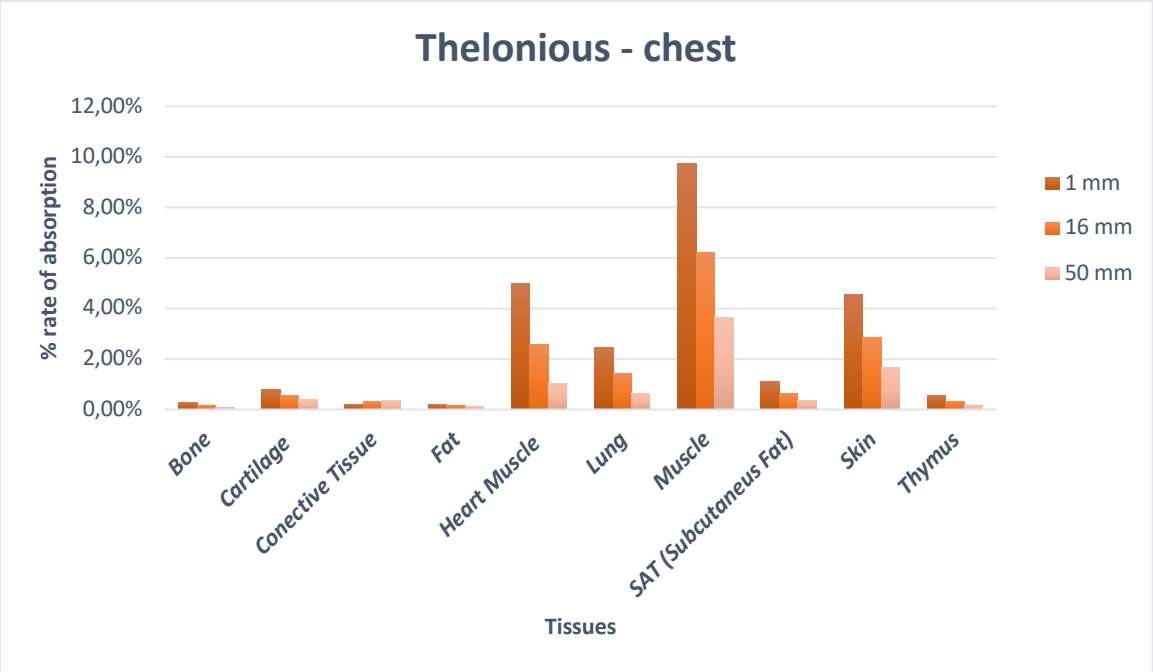

Figure 69: Histogram about Percentage of absorbed power by selected tissues (case Thelonious chest).

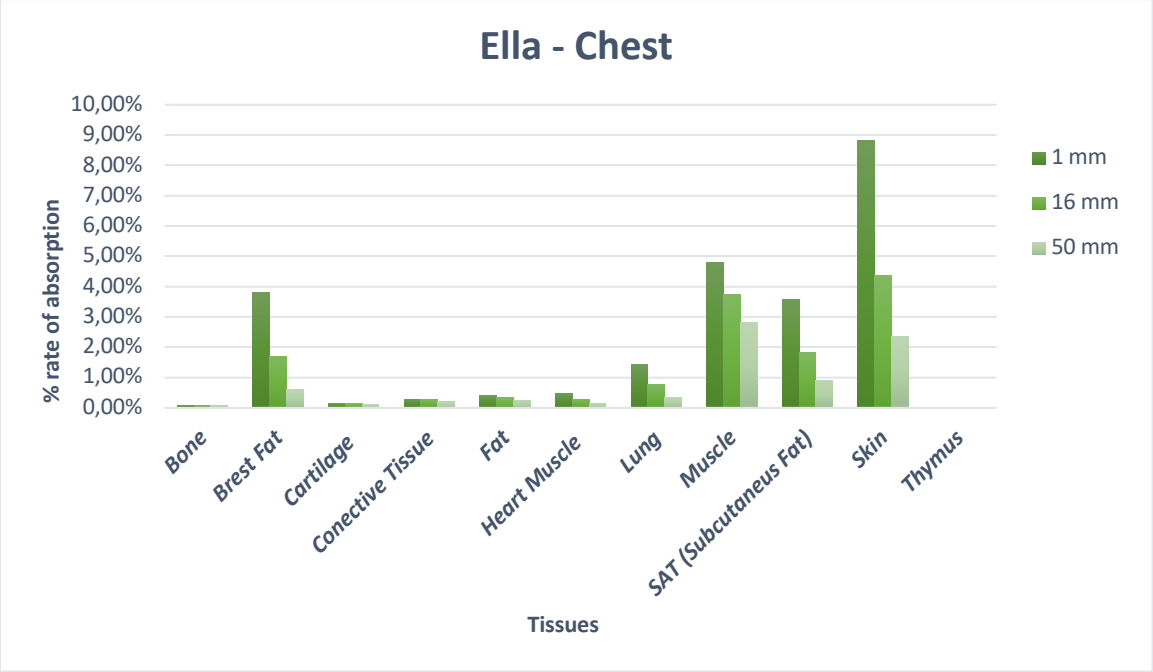

Figure 70: Histogram about Percentage of absorbed power by selected tissues (case Ella chest).

4.Discussion and Conclusion

Previous simulations of the interaction between antenna and biological models were chosen to recreate the three most common positions in which the smartphone is used, i.e. the situation in which the smartphone is close to the left ear, in front of the mouth and on the left side of the chest. We also selected potential distances for each circumstance in which the incident power supply was set to:

1. As close as possible to the skin (1 mm)
2. Medium distance from the skin (16 mm)
3. Long distance from the skin (50 mm)

These positions represent, respectively, the case in which the person usually holds the phone when making a call (left ear), when making phone calls or voice messages via the speaker (mouth case), and, finally, the case in which one uses the smartphone via earphones, for example, and places the phone in a jacket pocket (chest case).

This choice of PIFA antenna was made because an antenna with such characteristics offers versatility and compactness (63), making it typical for smartphones and wireless devices (64) (65) (66). Furthermore, an L-shaped PIFA antenna allows for a compact design, especially for devices with limited space. It can also help to reduce interference by providing isolation between the antenna and other components on the same circuit. Most importantly, this type of antenna is used because it offers performance across various frequency bands, which is essential for devices operating on different communication standards such as GSM (Global System for Mobile Communications), UMTS (Universal Mobile Telecommunications System) and LTE (Long-Term Evolution), practically thease are communication standards corresponding to the second (2G), third (3G), and fourth (4G) generations, respectively.

The choice of frequency was determined to be 1.8 GHz, as this is the operational frequency for GSM (67) (68) , UMTS (69) (70), and certain implementations of LTE networks. (71)

The first communication standard was developed to enable voice and digital data transmission through cellular networks, laying the foundation for mobile communication. UMTS was designed to increase transmission speed compared to its predecessor. Finally, LTE was developed to provide greater speed not only for voice and data transmission but also for video streaming and internet browsing. A notable feature of LTE is that it operates on different frequency bands depending on the country.

As for the biological models, there are those simulating the female body and those simulating the body of a child.

In the first case, two different biological models were chosen based on age while striving to achieve similarity in terms of body proportions between the two female biological models used. Specifically, we selected Ella and Laura respectively for constructing simulations and processing in the FDTD code and CST Studio case. Ella and Laura are biological models simulating the female body but are characterized by two different ages. In this specific instance, Ella represents a 26-year-old woman, whereas Laura simulates a 46-year-old woman. It was not possible to select a biological model closer in age to the one used in the FDTD code due to the limited availability of suitable body databases. Therefore, the choice fell on Laura, who exhibited a BMI and physical characteristics more similar to Ella's, always considering that the water content in biological tissues varies as people age; this constitutes the primary difference between the two human models used.

In the case of biological models simulating child bodies, we chose the biological models "Thelonious" and "child" respectively for FDTD code and CST Studio. In this scenario as well, the main limitation in terms of model databases stems from the CST Studio case, as it provided only a biological model of a 7-year-old girl. This differs in the case of the FDTD code, where we selected a 6-year-old boy. However, in this case, the physiological differences between the two models are extremely minimal.

For all biological models, we chose to analyze only the upper body in order to reduce computational complexity and consequently the duration of the simulations.

Additionally, graphical representations were produced in both environments and for all models, aiming to use a similar color scale to represent them. Specifically, we used the "Rainbow Desaturated" scale for simulations in FDTD and a scale called "Rainbow" for simulations in CST.

Subsequently, tables were generated for each biological model, containing the highest SAR value, both averaged at 1g and 10g, including all positions and respective distances between the antenna and the biological bodies used. This was done to highlight, analyze, and better compare the SAR (1g and 10g) obtained similarly across various models.

One of the aims of this study is to demonstrate the similarity between two investigated methods, namely FDTD and FIT. The FDTD method is implemented using the C programming language, while the FIT method utilizes the CST Studio Suite to calculate the SAR for 1 g and 10 g of tissue. By employing different biological models with slight variations in physical characteristics, substantial differences in SAR results were observed for both the 1 g and 10 g cases. Specifically, in the simulations involving female body types, a comparison was made between Ella and Laura, who exhibited notable differences in age, slight variations in weight, and consequently, differences in BMI calculations. These models were chosen for comparison due to the limited availability of databases on biological models, and their similarity to each other. These differences may have contributed to the divergent SAR results obtained with FDTD and FIT for both the 1 g and 10 g scenarios.

In particular, as summarized in *table 20*, which presents the SAR values for the 1g case, the FDTD method shows significantly higher SAR values compared to CST Studio, especially in the 1 mm case where the PIFA (Planar Inverted F-Antenna) is located in close proximity to the ear. Considering that the SAR limit for 1g of tissue is 1.6 W/kg, it can be observed that our results, particularly for the ear and chest at a 1 mm distance, greatly exceed the limit, with the exception of the mouth case, which exhibits a much lower value compared to the imposed limit. Naturally, it is known that increasing the distance between the subject and the radiation source will reduce the exposure. Therefore, it can be noticed that at distances of 16 mm and 50 mm in all positions (ear, mouth, and chest), the SAR value decreases significantly and falls within the imposed SAR ranges.

Regarding the SAR in 10 g of tissue, as shown in *table 21*, the SAR limits are widely respected, considering that the maximum allowable value is 2 W/kg. The highest SAR value is observed in the ear at 1 mm for both the FDTD and CST Studio methods, with values of 1.718 W/kg and 1.545 W/kg, respectively.

The FDTD method showed higher SAR values, particularly when the PIFA was in close proximity to the ear, while still complying with SAR limits for 10 g of tissue. These findings

highlight the need for careful evaluation and comparison of methods in SAR analysis for different tissue scenarios.

In the case of simulations using child body types, we considered a 7-year-old girl (in CST Studio) and a 6-year-old boy (in FDTD). They share similarities in age and height but differ in weight, and consequently, in BMI. In this case, as shown in *table 18*, which summarizes all the results of FDTD and FIT in the three positions (ear, chest, and mouth) at three different distances for the 1 g tissue case, we observe higher SAR values in CST compared to FDTD for the ear position. However, when the PIFA is located near the chest and mouth, both FIT and FDTD demonstrate SAR values within acceptable ranges for the SAR limits at 1 g, except when the PIFA is situated extremely close to the ear and chest. Regarding the 10 g tissue case, all SAR values are shown to be fully compliant with the SAR limits, even for the ear and chest at 1 mm.

For the 1 g tissue case, CST Studio produces higher SAR values than FDTD for the ear position, but both methods are within acceptable SAR ranges for the chest and mouth positions, except when the PIFA is extremely close to the ear and chest. For the 10 g tissue case, all SAR values comply with the SAR limits, including the ear and chest at 1 mm.

Analyzing the obtained results, we can state that the interaction between the mouth and PIFA, considering all three distances, can be considered the best as it exhibits low SAR values compared to the other cases. On the contrary, the worst case occurs during the simulation of the interaction between the antenna and the ear, especially when they are extremely close. However, it is important to consider that the increase in SAR is influenced by various factors, such as the position of the device or radiation source within the device, the exposure angle, and other individual characteristics of the model.

Furthermore, from the SAR, it is possible to obtain information about the power absorbed by the tissues of the biological models. However, this was only feasible in the case of the FDTD code simulation, as an additional license, currently not available, would have been required with CST Studio to retrieve information in terms of SAR and absorbed power by individual tissues considered during the simulations.

Based on the results presented in *table 23*, in the scenarios where the interaction between the left ear and the biological models is simulated, it has emerged that, for the case of Thelonious, the tissue that absorbed the most power is the muscle tissue, with a value of 7.33% relative to the total electric field it was subjected to. This is closely followed by gray

matter of the brain (4.34%), skin (3.55%), as well as connective tissue (2.55%); these values are obtained when the interaction between the PIFA and the subject is extremely close (1 mm). However, even when the antenna is moved away from the subject, the most affected tissues remain the same, albeit with lower values, naturally. Analyzing the "Ella" model yields a similar situation, where the muscle tissue and skin are predominantly affected.

In the second case of study, both for Thelonious and Ella, the tissues that absorbed the most power are the muscle tissue (6.79% for Thelonious, 7.61% for Ella) and the skin. Specifically, in Ella's case, the connective tissue (1.75%) and cartilage (1.73%) were also affected.

Finally, in the last simulation scenario where the PIFA is positioned on the left side of the chest, it is necessary to highlight tissues such as the heart muscle (5% for the child), and the lung for both biological models. Particularly in the case of Ella, it's important to consider that one of the tissues most affected is Breast Fat (3.81% at 1 mm distance).

In conclusion, our results indicate that the FDTD method shows higher SAR values compared to the FIT method for both 1 g and 10 g of tissue. The results of the return loss simulations done without the biological maps were similar with one another, therefore the discrepancies in SAR between the two approaches could be attributed to their various biological maps, positions and distances of the antenna.

Further studies are necessary to deepen our understanding of the subject. It is important to strive for more similar models, expand the databases of biological models, and conduct a greater number of simulations, including the case of a male subject. By doing so, we can gather more comprehensive and representative data, allowing for more accurate assessments and comparisons between different methods. This will contribute to advancing our knowledge in the field and ensuring the development of safer and more effective approaches in the context of SAR calculations and electromagnetic interactions with biological tissues.

5. Bibliography

1. Balanis, Constantine A. *Antenna Theory, Analysis and Design.* s.l. : John Wiley & Sons, 2nd ed. 1982.

2. M., Firoozy N. & Shirazi. *Planar Inverted-F antenna (PIFA) design dissection for cellular communication application. .*

3. Cheng, David K. *Field and Wave Electromagnetics.* s.l. : Addison-Wesley Publishing Company Inc., Edition 2, 1998. .

4. Balmain, Edward C. Jordan & Keith G. *Electromagnetic Waves and Radiating Systems.* s.l. : Prentice-Hall, 2nd ed. 1968.

5. Gas, Piotr. *Optimization of multi-slot coaxial antennas for microwave thermotherapy based on the S11-parameter analysis.* s.l. : Biocybernetics and Biomedical Engineerin, 2017.

6. Hall, J. R. James and P. S. *Handbook of Microstrip Antennas.* s.l. : Peter Peregrinus, 1989.

7. Pozar, D. M. *Microstrip Antennas.* January 1992. .

8. Deschamps, G. A. *Microstrip Microwave Antennas.* 1953.

9. L., Garcia. *Contribution to the characterization and evaluation of multiple antenna systems for communications .*

10. R., K.Fujimoto and J. *Mobile antenna systems handbook.* s.l. : James Artech House , 1994.

11. Rahmat-Samii, M.A. Jensen and Y. *Performance of antennas for hand-held transceivers using FDTD.* s.l. : IEEE Trans. Antennas Propagatevi, August 1994 .

12. Gyoungdeuk Kim, Sangkil Kim. *Design and Analysis of Dual Polarized Broadband Microstrip Patch Antenna for 5G mmWave Antenna Module on FR4 Substrate .* 2021.

13. Datasheet, ALTERA. *Using Pre-Emphasis and Equalization with Stratix GX.* 2003.

14. Broadband, Kumar G. & Ray K. *Microstrip Antennas.* s.l. : Artech House Inc, 2003.

15. Weiland, T. *A discretization method for the solution of Maxwell's equations for six-component fields: Electronics and Communication.* 1977.

16. Yee, K. S. *Numerical Solution of Initial Boundary Value Problems Involving Maxwell's Equations in Isotropic Media.* s.l. : EEE Trans. Antennas Propag, 1966.

17. Taflove, A. *Application of the Finite-Difference Time-Domain Method to Sinusoidal Steady-State Electromagnetic-Penetration Problems.* s.l. : IEEE Trans. Electromagn. Compat, 1980.

18. Resolutions., International Committee for Weights and Measures (CIPM). *CIPM, 1946: Resolution 2 / Definitions of Electrical Units.* s.l. : International Bureau of Weights and Measures (BIPM), 1946.

19. Dey, S. and R. Miu.ra. *"A locally conformal finite-difference timc-domain algorithm for modeling Ihrcc:-dimc:nsional perfectly conducting objects.* s.l. : IEEE Microwave Guided Wave , 1997.

20. Hall., Shankar. V.. A. H. Mohammadian. and W. F. *A timcHlomain finite lume traaDall f; Maxwell equations.* s.l. : EJrelromagnelics, 1990.

21. Luebbers, K. S. Kunz and R. J. *The Finite Difference Time Domain Method for Electromagnetics.* 2018.

22. tion, International Commissionon Non-Ionizing RadiationProtec-. *Guidelines for Limiting Exposure to Electromagnetic Fields (100 kHz to 300 GHz).* 2020.

23. Hagness, A. Taflove and S. C. *"Computational Electrodynamics: The Finite-Difference Time-Domain Method, Third Edition," .* s.l. : Artech House. , 2005.

24. Vee, K. S. *Antennas and Propagation.* s.l. : IEEE Trans. , 1966.

25. Taflove, A., & Hagness, S. C. *Computational electrodynamics: the finite-difference time-domain method. .* s.l. : Artech House., 2005.

26. Jin, J. *The finite element method in electromagnetics.* s.l. : John Wiley & Sons., 2015.

27. Weiland, T. *Time domain electromagnetic field computation with finite difference methods. International Journal of Numerical Modelling.* 1996.

28. Krietenstein, B., et al. *The Perfect Boundary Approximation technique facing the challenge of high precision field computation: Proc. of the XIX International Linear Accelerator Conference .* 1998.

29. oshanka Ranasinghe, Cilia Swinkels, Arjen Luijendijk, Dano Roelvink, Judith Bosboom, Marcel Stive, DirkJan Walstra. *Morphodynamic upscaling with the MORFAC approach: Dependencies and sensitivities,.* s.l. : Coastal Engineering, 2011.

30. Hagness, A. Taflove and S. C. *The Finite-Difference Time-Domain Method .* Third Edition.2005.

31. A.Z. Elsherbeni, V. Demir. *The Finite-Difference Time-Domain Method for Electromagnetics with Matlab(r) Simulations.* s.l. : SciTech Publishing, Edison, 2015.

32. L. Zhen-Feng, H. Kong-Liang, Y. Bai-Po, Y. Yi-Fan . *A transmitting boundary for transient wave analyses Sci.* 1984.

33. Kelvin A. Carvalho, Fernando H. Silveira. *Evaluation of the lightning performance of grounding electrodes using FDTD-based computational model: Influence of absorbing boundary conditions and representation of the frequency-dependence of soil parameters.*

34. A. Taflove, S.C. *Hagness Computational Electrodynamics: The Finite-Difference Time-Domain Method(Edição: 3).* Boston : Artech House Publishers, 2005.

35. Weiland, M. Clemens and T. *Magnetic field simulation using conformal FIT formulations,.* s.l. : IEEE Transaction Magnetics, 2002.

36. Yee, K. S. *Numerical solution of initial boundary value problems involving Maxwell's equations in isotropic media.* s.l. : IEEE Transaction Antennas and Propagation, 1966.

37. S. M. Rao, G. K. Gothard, and D. R. Wilton. *Application of finite integration technique to electromagnetic scattering by two-dimensional cavity-backed aperture in a ground plane.* s.l. : IEEE Transaction on Antennas and Propagation.

38. K. J. Langberg and R. Marklein. *Inverse scattering with acoustic, electromagnetic, and elastic waves as applied in nanodestructive testing.* Vienna : Wavefield Inversion, Springer, 1999.

39. Rienen, [V. C. Montrescu and U. V. *Simulation of electromagnetic fields in the human body using finite integration technique (FIT),.* s.l. : Biomedizinische Technik/Biomedical Engineering, 2002.

40. 1528-2003), IEEE Std 1528-2013 (Revision of IEEE Std. *IEEE Recommended Practice for Determining the Peak Spatial-Average Specific Absorption Rate (SAR) in the Human Head from Wireless Communications Devices: Measurement Techniques,.*

41. Chou, C. K., et al.,. *Radio frequency electromagnetic exposure: Tutorial review on experimental dosimetry.* s.l. : Bioelectromagnetics, 1996.

42. Balzano, Q., Garay, O., and Steel, F. R. *Energy deposition in simulated human operators of 800 MHz portable transmitters,.* s.l. : IEEE Transactions on Vehicular Technology, June 26, 1978.

43. Kuster, N., and Balzano, Q. *Energy absorption mechanism by biological bodies in the near field of dipole antennas above 300 MHz.* IEEE Transactions on Vehicular Technology : s.n., Feb. 1992.

44. 1528-2003), IEEE Std 1528-2013 (Revision of IEEE Std. *IEEE Recommended Practice for Determining the Peak Spatial-Average Specific Absorption Rate (SAR) in the Human Head from Wireless Communications Devices: Measurement Techniques.*

45. N. Mukherjee, A. Kundu, B. Gupta and M. Mitra. *"Specific Absorption Rate Estimation for a Typical Hibiscus Flower Model as per ICNIRP Electromagnetic Guidelines,.* s.l. : IEEE Calcutta Conference (CALCON), 2020.

46. Gupta, A. Kundu and B. *Comparative SAR Analysis of Some Indian Fruits as per the Revised RF Exposure Guideline.* s.l. : IETE Journal of Research, 2014.

47. A. Kundu, B. Gupta and A. I. Mallick. *Dependence of electromagnetic energy distribution inside a typical multilayer fruit model on direction of arrival and polarization of incident field.* s.l. : IEEE Radio and Antenna Days of the Indian Ocean, 2019.

48. Lin, James C. *RF Health Safety Limits and Recommendations .*

49. Commission, Federal Communication. *Evaluating compliance with FCC specified guidelines for human exposure to radiofrequency radiation,.* 1996.

50. D.Pimienta-DelValleandR.Lagar-Pérez. *Designofadual-bandPIFA for handset devices and it SAR evaluation,.* s.l. : Ingeniería, Investigación y Tecnología, 2016.

51. I.Belyaev, C.Blackman,K.Chamberlin,A.DeSalles,S.Dasdag,C.Fer- nández, L. Hardell, P. Héroux, E. Kelley, K. Kesari, D. Maisch, E. Mallery- Blythe, R. Melnick, A. Miller, J. Moskowitz, W. Sun, I. Yakymenko. *Scientific evidence invalidates health assumptions underlying the FCC and ICNIRP exposure limit determinations for ra- diofrequency radiation: implications for 5G.* 2022.

52. Domingo Pimienta-Del Valle, Raidel Lagar-Pérez. *Design of a Dual-Band PIFA for Handset Devices and it SAR Evaluation.* s.l. : Ingeniería, Investigación y Tecnología , 2016.

53. D.Pimienta-DelValleandR.Lagar-Pérez. *Design of a dual-band PIFA for handset devices and it SAR evaluation.* s.l. : Ingeniería, Investigación y Tecnología, 2016.

54. Caon, M. *Voxel-based computational models of real human anatomy: a review.* s.l. : Radiation and Environmental Biophysics, 2004.

55. M.Nikolovski. *Detailed modeling of the human body in motion to investigate the electromagnetic influence of fields in a realistic environment.* 2017.

56. Ellis, R. E. *Reference man: Anatomical, physiological and metabolic characteristics. report of the task group on reference man ICRP publication 23.* s.l. : Physics Bulletin, feb 1976.

57. C.Warren, L.Pajewski,A.Ventura,andA.Giannopoulos,'. *An evaluation of finite-difference and finite-integration time-domain modelling tools for ground penetrating radar antennas.* 2016.

58. J. Wang, Y.-S. Xia, and W.-Y. Yin. *Study on sar distribution of human body on the vehicle platform using a modified fdtd method.* 2018.

59. M.-C. Gosselin, E. Neufeld, H. Moser, E. Huber, S. Farcito, L. Gerber, M. Jedensjö, I. Hilber, F. D. Gennaro, B. Lloyd, E. Cherubini, D. Szczerba, W. Kainz, and N. Kuster. *Development of a new generation of high- resolution anatomical models for medical device evaluation: the virtual population 3.0.* 2014.

60. Moreland, K. *The ParaView Tutorial.* 2014.

61. al., K. Moreland et. *ParaView Getting Started Guide,.* s.l. : Sandia Natl. Lab., 2015.

62. P1528/D6, IEEE. *IEEE draft recommended practice for determining the peak spatial average specific absorption rate (SAR) in the human head from wireless communications devices: Measurement techniques.* 2013.

63. Andrea D'alessandro, Roberto Caso Marcos R. Pino and Paolo Nepa. *Dual-Band Integrated Antennas for DVB-T Receivers.* 2013.

64. S. i. Kwak, D.-U. Sim, J. H. Kwon, and Y. J. Yoon. *'Design of pifa with metamaterials for body-sar reduction in wearable applications.* s.l. : IEEE Trans. Electromagn. Compat, 2017.

65. K.Rabaani, W.Chelly,M.K.Azizi,R.Collela,and L.Cataranucci. *Planar inverted-f antenna for bluetooth applications.* 2022.

66. D.Bonefacic, B.Rapinac,andJ.Bartolic. *Slotted PIFA for GSM band.* s.l. : Second European Conference on Antennas and Propagation, 2007.

67. Rahnema, Moe. *Overview of the GSM system and protocol architecture.* s.l. : IEEE Communications magazine , 1993.

68. Drane, Christopher, Malcolm Macnaughtan, and Craig Scott. *Positioning GSM telephones.* s.l. : IEEE Communications magazine, 1998.

69. H Kaaranen, A Ahtiainen, L Laitinen, S Naghian. *UMTS networks: architecture, mobility and services .* 2005.

70. BH Walke, P Seidenberg, MP Althoff. *UMTS: the fundamentals .* 2003.

71. S Sesia, I Toufik, M Baker. *LTE-the UMTS long term evolution: from theory to practice.* 2011.

Acknowledgments

A special thank you goes to my supervisor, Franco Moglie, my co-supervisor, Valter Mariani Primiani, and their research team. Their guidance, support, and confidence in me have made the completion of this thesis possible. Their knowledge and commitment have been essential for the success of this research project my personal growth journey.